METEOR-Bericht

Sector collapse kinematics and tsunami implications – SEKT

Cruise No. M154-2

April 29 – Mai 23, 2019

Pointe-à-Pitre (Guadeloupe) – Pointe-à-Pitre (Guadeloupe)

T. Freudenthal, K. Dehning, R. Gatter, C. Hilgenfeldt, L. Hönekopp, M. Hornbach, M. Kühn, J. Kuhlmann, S. Kutterolf, B. Meyer-Schack, K. Pallapies, S.K. Rapp, C. Sievers, S. Watt, and M. Stelzner

K. Huhn

MARUM, Universität Bremen

2019

Table of Contents

1 Cruise Summary

1.1 Summary in English

Deep-seated collapses of volcanic islands have generated the largest volume mass flows worldwide. These mass flows might trigger mega-tsunamis. The way in which these collapse events are emplaced is poorly understood, although this emplacement process determines the scale of associated tsunamis. Key questions such as whether they are emplaced in single or multiple events, how they may incorporate seafloor sediment to increase their volume, and how they are related to volcanic eruption cycles and migration of volcanic centres, still remain to be answered.

This project forms a part of the comprehensive study of large volcanic island landslide deposits and is directly linked to the IODP drilling campaign in the Lesser Antilles (IODP Leg 340). Unfortunately, Leg 340 only recovered material from a single site within the volcanic landslide deposits off Montserrat, and even at this site recovery was not continuous. This single IODP site is insufficient to document lateral variation in landslide character, which is critical for understanding how it was emplaced. The main scientific goals of this project are to determine where the landslides are sourced from; to understand how these landslides are emplaced; and to understand the relationship between landslides, eruption cycles and initiation of new volcanic centres. Based on results of a 3D seismic dataset acquired during Leg 1, ten MeBo cores and 18 gravity cores were drilled during this M154-2 (Leg 2). These data provide a unique dataset of the internal structure, composition and source of material throughout a volcanic island landslide. The results will significantly contribute to understanding the emplacement of volcanic island landslides and they will allow us to assess the associated tsunami risk.

1.2 Zusammenfassung

Hangrutschungen, die bei Flankenkollapsen vulkanischer Ozeaninseln entstehen, zählen zu den größten Rutschungen weltweit und können möglicherweise Mega-Tsunamis auslösen. Da die Dynamik der Kollapsereignisse ein entscheidender Faktor ist, jedoch schwer zu bestimmen, wird die Höhe der Tsunamis kontrovers diskutiert. Hauptfragestellungen sind dabei, ob die initialisierte Unterwasserrutschung in einem einzelnen oder in mehreren Ereignissen stattfindet, inwieweit neben dem initial destabilisierten Material weitere Sedimente mittransportiert werden, und wie sie mit Vulkanausbruchszyklen und der Migration von vulkanischen Zentren zusammenhängen.

M154 baut auf der ersten groß angelegten interdisziplinären Untersuchung der Rutschungsablagerungen von Vulkaninseln und einer IODP-Bohrung bei den Kleinen Antillen (IODP Leg 340). Leider wurde nur ein unvollständiger Kern innerhalb der vulkanischen Hangrutschungen vor Montserrat erbohrt. Informationen über laterale Änderung der Hangrutschung können auf der bisherigen Datenbasis nicht erforscht werden, obwohl diese für das Verständnis des Ablagerungsprozesses von entscheidender Bedeutung sind. Die Kombination von Bohrungen und 3D Seismik hat einen einmaligen Datensatz zur Untersuchung der internen Strukturen, der Zusammensetzung und der Herkunft des Materials der vulkanischen Rutschmassen ergeben. Die Ergebnisse sollen zum Verständnis der Prozesse beitragen, die während vulkanischer Hangrutschungen aktiv sind und so eine Quantifizierung des Tsunamipotentials erlauben. Die wichtigsten wissenschaftlichen Ziele der Ausfahrt sind es, zu bestimmen, woher die Rutschmassen stammen; wie diese abgelagert werden; und den Zusammenhang zwischen Hangrutschungen, Ausbruchszyklen und der Initiierung neuer Vulkanzentren zu verstehen.

2 Participants

2.1 Principal Investigators

Prof. Dr. Katrin Huhn	Chief Scientist	MARUM

2.2 Scientific Party

Name, Academic Title	Discipline	Institution
Bergenthal, Markus	MeBo Team	MARUM
Buelten, Jutta	MeBo Team	MARUM
Dehning, Klaus	Gravity coring	MARUM
Coulibaly, Ousmane	MeBo Team	MARUM
Freudenthal, Tim, Dr.	MeBo Team	MARUM
Gatter, Ricarda	Physical properties	MARUM
Hilgenfeldt, Christian	Gravity coring	MARUM
Hoenekopp, Leonie	Physical properties	MARUM
Hornbach, Matt, Prof. Dr.	Hydroacoustic	SMU Dallas
Klar, Steffen	MeBo Team	MARUM
Kuehn, Michel	Hydroacoustic	GEOMAR
Kuhlmann, Jannis, Dr.	Physical properties	MARUM
Kutterolf, Steffen, Dr.	Core description	GEOMAR
Linowski, Erik	MeBo Team	MARUM
Meyer-Schack, Birgit	Core curation	MARUM
Noorlander, Cornelius	MeBo Team	MARUM
Pallapies, Kilian	Hydroacoustic	MARUM
Rapp, Sophia Kristina	Physical properties	MARUM
Rehage, Ralf	MeBo Team	MARUM
Schmidt, Werner	MeBo Team	MARUM
Sievers, Carina	Core description	GEOMAR
Watt, Sebastian, Dr.	Core description	University of Birmingham
Stelzner, Martin	Meteorology	DWD

2.3 Participating Institutes

MARUM	Zentrum für Marine Umweltwissenschaften, Universität Bremen
GEOMAR	Helmholtz-Zentrum für Ozeanforschung Kiel
University of Birmingham	
SMU Dallas	Southern Methodist University, Dallas
DWD	Deutscher Wetterdienst, Geschäftsstelle Seeschifffahrt

2.4 Crew

Name	**Rank**
Hammacher, Rainer	Kapitän / Master
Soßna, Yves Michael	Chiefmate / Chiefmate
Göbel, Jens	1. Offizier / First Mate
Mock, Benjamin	2. Offizier / 2nd Officer
Neumann, Peter	Ltd. Ingenieur / Chief Engineer
Brandt, Björn	2. Ingenieur / 2nd Engineer
Heitzer, Ralf	2. Ingenieur / 2nd Engineer
Rottkemper, Oliver	SET / Electrical Engineer
Lange, Gerhard	Decksschlosser / Fitter
Kudrass, Klaus	Motorenwärter / Motorman
Eller, Lukas	Motorenwärter / Motorman
Erdmann, Ole	Motorenwärter / Motorman
Willms, Olaf	Ltd. Elektroniker / Chief Electronic
Hebold, Cathi	Elektroniker / Electronic
Seidel, Stefan	Systemmanager / Systemmanager
Zeigert, Michael	Bootsmann / Boatswain
Behlke, Hans	Matrose / Sailor
Bußmann, Piotr	Matrose / Sailor
Drakopoulos, Evgenios	Matrose / Sailor
de Moliner, Ralf	Matrose / Sailor
Pleuler, Merlin Till	Matrose / Sailor
Koch, Stefan	Matrose / Sailor
O'Keefe, Darren	Matrose / Sailor
Staffeldt, Felix	Azubi / Apprentice
Brinckmann, Ferdinand Dr.	Arzt / Doctor
Parlow, Jan	1. Steward / Chief Steward
Zimmermann, Petra	Stewardess / Stewardess
Jürgens, Moni	Stewardess / Stewardess
Zhang, Gou Min	Wäscher / Laundry Master
Wernitz, Peter	Koch /Cook
Kosanke, Patrick	Kochsmaat / 2. Cook

3 Research Program

(K. Huhn)

3.1 Aims of the Cruise

3.1.1 Volcanic Ocean-Island Landslides

The collapse of volcanic islands can generate extremely large landslides. This is why this type of landslide is so dangerous, both due to the initial slide itself and through far field tsunami generation. Volcanic island landslides can have volumes of up to several thousand of cubic kilometres. For instance, the Nuuanu landslide off Oahu (Hawaiian Islands) has a volume of ~5,000 km^3 (Moore et al., 1989), making it the largest volume mass flows yet mapped on our planet. The largest known landslide found on land occurs on Mt Shasta and has a volume of only ~45 km^3 (Crandell, 1989). For comparison, the flank collapse that occurred during the well known 1980 eruption of Mt St Helens had a volume of ~ 3 km^3 (Sousa and Voight, 1995).

Seafloor mapping has shown that major landslide deposits are common around volcanic islands worldwide. The first systematic study was carried out along the Hawaiian Ridge, revealing at least 68 major landslides along a 2,200-km stretch of the ridge (Moore et al., 1989; Moore and Normark, 1994; Moore et al., 1995; McMurtry et al., 2004; Williams et al., 2006). Since then, major debris avalanches have been identified around numerous oceanic island groups including the Marquesas Islands (Wolfe et al., 1994), La Réunion (Labazuy, 1996), the Cape Verde Islands (Masson et al., 2008), the Lesser Antilles (Deplus et al., 2001; Boudon et al., 2007), and the Canary Islands (Watts and Masson, 1995; Urgeles et al., 1999; Krastel et al., 2001; Masson et al., 2002). Giant submarine landslides play an important role during the evolution of volcanic islands, especially during the shield phase of volcanic islands, when high amounts of magmatic activity leads to the quick build-up of potentially unstable volcanic edifices (Moore et al., 1989; Krastel et al., 2001).

3.1.2 Tsunami Generation by Volcanic Island Landslides

There is considerable controversy over the likely magnitudes of tsunamis generated by volcanic island landslides, and hence the hazard they may pose. We need to better understand how submarine landslides are emplaced because it is this emplacement process that determines the tsunami magnitude. In particular, we need to understand (1) where the material in the landslide originates from, and (2) whether the landslide was emplaced in one or multiple stages.

Origin of material in the landslide: The original source of material within the landslide has a strong control on the scale of tsunami produced by a landslide (Watt et al., 2012a). The volume is one of the most critical parameters for tsunami generation. For the same unit volume, however, a landslide originating on the submerged flanks of the volcano, and especially from the seafloor, will produce a smaller tsunami than a landslide comprising only the subaerial volcanic edifice. As noted by Watt et al. (2012a), a landslide offshore Montserrat would have produced significantly smaller tsunamis if much of the material was seafloor sediment rather than parts of the volcanic edifice (Watt et al., 2012a). In addition, tsunami magnitude is also critically dependent on whether failure occurs in one stage or in many separate stages. Failure in a series of stages separated by a few tens of seconds or minutes can substantially reduce the resulting tsunami magnitude (Løvholt et al., 2005, 2010). Landslide deposits can be relatively complex, and it is often the turbidity current that runs out beyond the landslide that provides the clearest record of emplacement

dynamics. For instance, Hunt et al. (2011) showed how the turbidite associated with the Icod volcanic landslide in the Canary Islands comprises a series of compositionally distinct subunits, which record multistage collapse. The presence of turbidite mud intervals within these subunits, which would take a considerable period of time to settle, suggests considerable delays between each stage of the collapse.

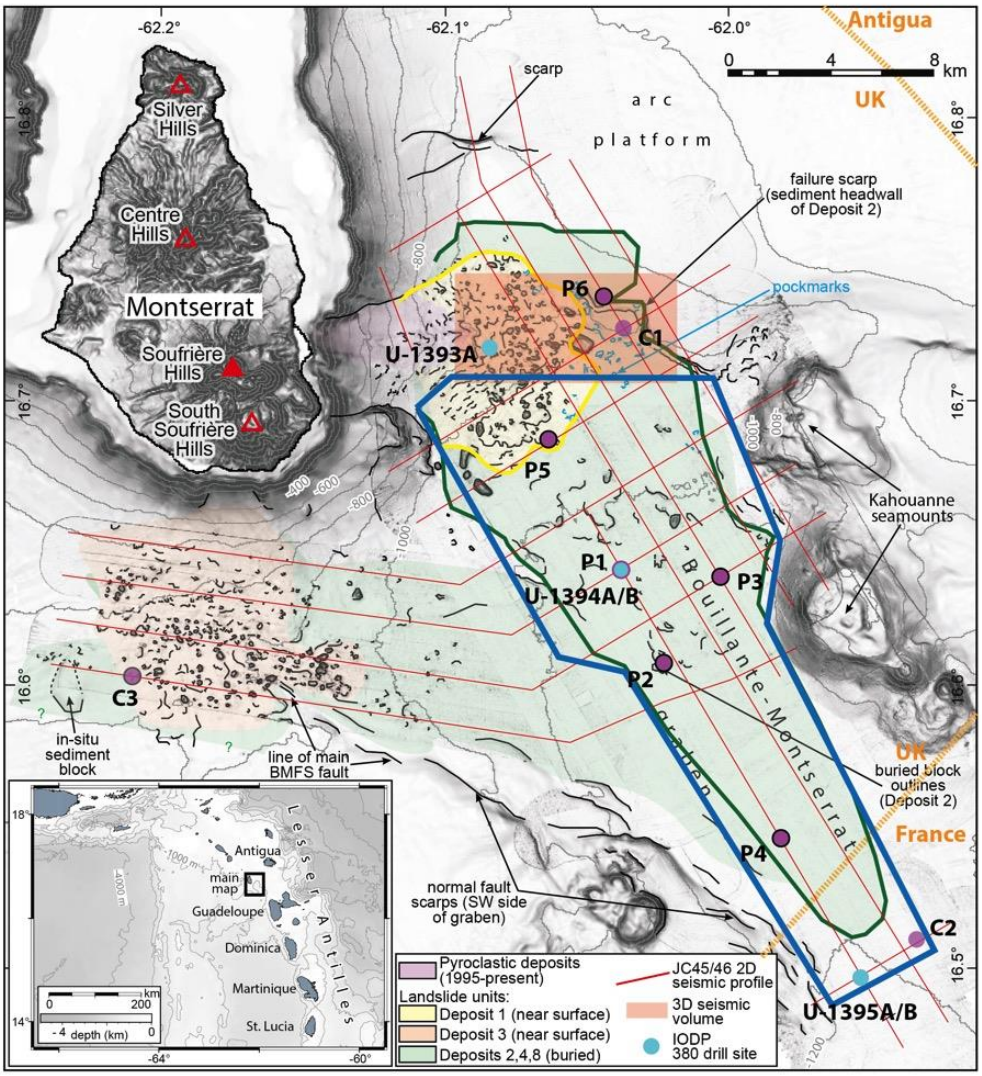

Fig. 3.1: Working area of R/V METEOR cruise M154-2 (modified after Watt et al., 2015).

IODP site U1395 offshore Montserrat recovered already slid masses and turbidite deposits associated with volcanic landslide Deposit 2 (Fig. 3.1). At a distance of 25 km from the island, the shallow section still comprises a series of massive fining-up sand intervals forming a spectacular 7 m thick deposit. Hence, landslide and mass flow deposits offshore from the volcanic island can be extremely large, and may pose a significant hazard, both from the slid event itself, and from resulting tsunamis. However, the emplacement dynamics of the Deposit 2 and its relationship to volcanic eruption cycles or magmatic evolution are still poorly understood, due to a lack of detailed studies of landslide deposits mainly because core recovery during IODP drilling was less than 15%.

3.2 Objectives

A central objective of the M154-2 cruise is a detailed analysis of landslide deposits off Montserrat by MeBo70 drilling in order to investigate the composition, origin, and deformation degree of slid material in different parts of the Deposit 2 southeast of the island (Fig. 3.1). Sedimentological and geotechnical analysis of these materials provide a hint to the source region of the slid masses, the kinematics of the slid event as well as the timing, e.g. to ensure that this was a single stage event. In addition, undisturbed slope sections were drilled in order to gain a deeper insight into the stratigraphy and the volcanic history respectively of this region. Therefore, major aims of this project are (1) to determine where the landslides are sourced from - the volcanic edifice or the sedimentary slope around ocean islands? (2) to understand how they are emplaced, and (3) to understand the relationship between landslides and eruption cycles.

(1) What type of material are the landslides made of, and where did that material originate from? How much seafloor sediment was incorporated into the landslides, and by what processes? What are the implications for tsunami generation?

The combination of MeBo70 cores, and 3D seismic data will document the spatial variability and overall character of the shallow most Deposit 2. The IODP site (U1394) that penetrated Deposit 2 shows that it is overlain by a very heterogeneous mass flow deposit that contains a range of volcanic and bioclastic material. However, it leaves two possible hypotheses for the origin of flat lying interbedded sand and mud intervals that form the lower part of Deposit 2, which are separated by homogenised sediments resembling debris flow matrix. The first hypothesis is that the packages of flat lying sediment are blocks of sediment incorporated into the landslide. The second hypothesis is that the flat lying sediment and debritic intervals are undeformed and in-situ and record a very prolonged multistage collapse of the volcano. This project aims to test the validity of these contrasting hypotheses.

MeBo core sites will aim to determine the runout deposits from both Deposits 1 and 2, and provide a full and unique record of ash fall and turbidites to the east of the volcano (since this is an area where the seafloor sediment has not failed). This is important for correlation with the distal IODP site U1396, and will provide a more comprehensive record of the volcanism at Montserrat over the past few 100 kyr. If time permits, another MeBo site will sample the mega-block of sediment that was incorporated into Deposit 2 to determine whether it is bedded seafloor sediment, the nature of its basal detachment surface, and whether any stratigraphic package is missing from this sequence, which may have formed Deposit 2b.

The origin and composition of Deposit 1 is still contentious, as this more recent and blockier avalanche deposit was not sampled successfully by IODP drilling. MeBo70 sampling will help establish the origin of these slid masses. Therefore, a MeBo core site is located just outside the slid deposits at the undisturbed margin where potential glide planes are easier to recover. A package of strong reflectors separate Deposit 1 and 2 at this location, and this core also aims to determine their composition and significance. It has been proposed that they represent submarine pyroclastic flow deposits that record a major period of volcanism.

(2) Have the landslides been emplaced in one event, or multiple widely separated events?

Understanding whether volcanic island landslides are emplaced in a single short-lived episode, or in multiple stages, is crucially important for predicting the magnitude of resulting tsunamis. Emplacement in multiple stages (even a few minutes apart) can greatly reduce initial tsunami

magnitude (e.g. by >50 %; Løvholt et al., 2005). The MeBo cores in combination with 3D seismic data will determine the significance of internal reflectors within Deposit 2 (Fig. 3.2), and whether these reflectors record emplacement in one or multiple stages.

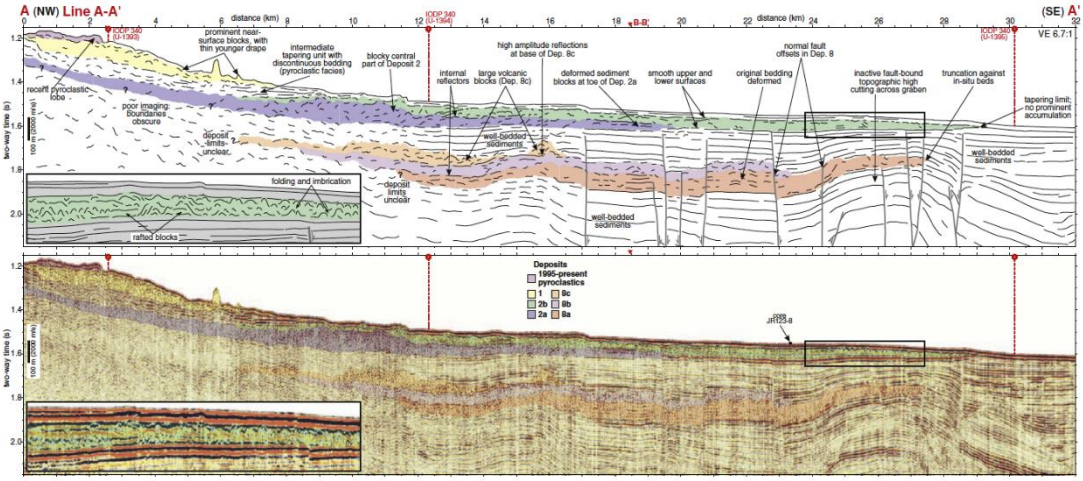

Fig. 3.2: High-resolution 2D seismic data showing the structure of the landslide Deposits 1, 2a, and 2b. Obtaining 3D seismic coverage is crucial to determine the amount of compression and to put the age constraints resulting from IODP Sites U1394 and 1395 into context (from Watt et al., 2012b; see Fig. 3.1 for location).

The deposits of longer runout turbidity currents can also be used to determine whether the associated landslide was emplaced in one or multiple stages (Wynn and Masson, 2003; Hunt et al., 2011). Turbidites that comprise multiple fining up sequences of sand capped by mud indicate emplacement in multiple widely spaced stages, as mud settles and consolidates slowly. At IODP site U1395, the spectacular 7 m thick turbidite associated with Deposit 2 comprise a series of stacked graded sand units without intervening mud (Fig. 3.2). This suggests that Deposit 2 was emplaced in a series of closely spaced pulses. However, an alternative explanation is that the mud drapes were removed by later stages of the flow. Coring a distal MeBo site located further up the basin margin aims to recover the distal part of the runout deposit from Deposit 2. The aim of this site is to determine whether the turbidite subunits are separated by mud intervals that record significant time gaps between the emplacement of the subunits. The finer grained sediments in this area will be easier to drill.

(3) What is the timing of major landslides relative to volcanic eruption cycles, initiation of new volcanic centres, or sea level change?

It is important to understand the timing of major landslide events relative to eruption cycles for hazard predictions. An exciting initial observation from IODP Leg 340 is that Deposit 2 is immediately overlain by a basaltic fallout deposit, suggesting it may be associated with a major change in magma composition, and initiation of the basaltic South Soufriere Hills centre on Montserrat. IODP core U1396 provides an excellent record of over 140 fallout layers during the last 4.5 Ma. During some periods, however, the direction of the wind would not be towards this site, and the fallout from eruptions would be elsewhere. Analysis of fallout deposits within the widely spaced MeBo and gravity cores will help to provide a more complete record of major volcanic eruptions on Montserrat. This core data will also help to determine precisely the emplacement age of Deposits 1 and 2. MeBo cores and gravity cores taken form (i) undisturbed slope section just north of the headwalls of Deposit 2 gain a deeper insight into the eruption and

deposition history and in this segment of the island, and (ii) from south of Montserrat will help to establish the age of debris avalanche Deposit 3, and its relation to eruption cycles.

3.3 Agenda of the Cruise

After labs and coring tools were set up and MeBo70 equipping was successful completed with the harbour basin test, we left the Port of Pointe-à-Pitre (Guadeloupe) shortly after lunchtime on the 29th April 2019. After a short transit of 7 h, we arrived in our research area offshore Montserrat and immediately continued with the hydro-acoustic mapping with the multibeam echosounder to extend the existing bathymetric map of the target area. For calibration, a Sound Velocity Profile (GeoB23702-2) was recorded. Together with EM122, PARASOUND data were recorded throughout the entire cruise.

As major aim of M154-2 was to sample slid masses and undisturbed slope segments off Montserrat, the majority of the working time was used for gravity coring and MeBo70 drilling. In total, MeBo70 was 20 days in operation at 6 locations to collect sediment samples (Fig. 3.3). In addition, in-situ Cone Penetration Test (CPT) measurements as well as borehole logging data were collected at five sites. Therefore, a Spectrum Gamma Instrument (SGR), a magnetic susceptibility (MagSus) and Acoustic probe (AcousP) were successfully utilized. In addition, a gravity corer was deployed 26 times, a box corer eight times, and a grab sampler three times. Furthermore, a heat flow probe was successfully tested and deployed attached to the gravity corer at six sites. This resulted on very short notice from a collaboration with the SMU Dallas.

3.4 Description of the Work Area

The island of Montserrat in the Lesser Antilles is an ideal natural laboratory to study volcanic island landslide processes (Fig. 3.1). Previous seismic data document the location of more than ten large landslide deposits around the island (Le Friant et al., 2004, 2012; Lebas et al., 2011; Watt et al., 2012a; Crutchley et al., 2013; Karstens et al., 2013). In several locations of Montserrat, blocky flank collapse deposits and more extensive, smoother deposits occur together (Watt et al., 2012b). With high-resolution geophysical data, authors were able to show that this emplacement relationship involves events dominated by seafloor sediment failure. The volume of the landslide deposits cannot be explained by the failure of volcanic material alone. Additionally, internal structures show that deposit emplacement may occur in multiple stages. Although of greater volume, the sediment failure component of these landslides produces small tsunamis in comparison to the volcanic component, which presents a more significant local hazard. This would suggest that some of the claims concerning tsunami height that were made for other volcanic islands (e.g. Canary Islands) were grossly exaggerated.

Several mass wasting deposits off Montserrat with contrasting characteristics (Deposits 1, 2, and 3) will be the focus of this project (Fig. 3.2). These landslides are relatively small, and we were therefore able to map them completely during M154-2. Deposit 1 (1.7 km^3), which is the most recent event, has a blocky character, and is draped by only ~1-2 m of sediment. Deposit 2 is much more extensive, with a smoother surface, and appears to contain a significant component of incorporated seafloor sediment. The buried Deposit 2 is overlain by 5 m to 10 m of drape. Deposit 2 is up to 90 m thick, and comprises two parts (the shallow Deposits 2a and the upper Deposit 2b; Fig. 3.2.2) separated by laterally extensive seismic reflectors. Emplacement of Deposit 2 appears to have triggered large-scale failure of seafloor sediment, as documented by a major head scarp

along the northeastern limit of the deposit (Fig. 3.1). Deposit 3 south of Montserrat seems to be the youngest event. It has a mean thickness of 30 m and extends approx. 10 km south. In addition, detailed investigation of the background stratigraphy in the vicinity of these landslides will enable a deeper insight into the eruption history and volcanic activity of the Montserrat volcanic cones.

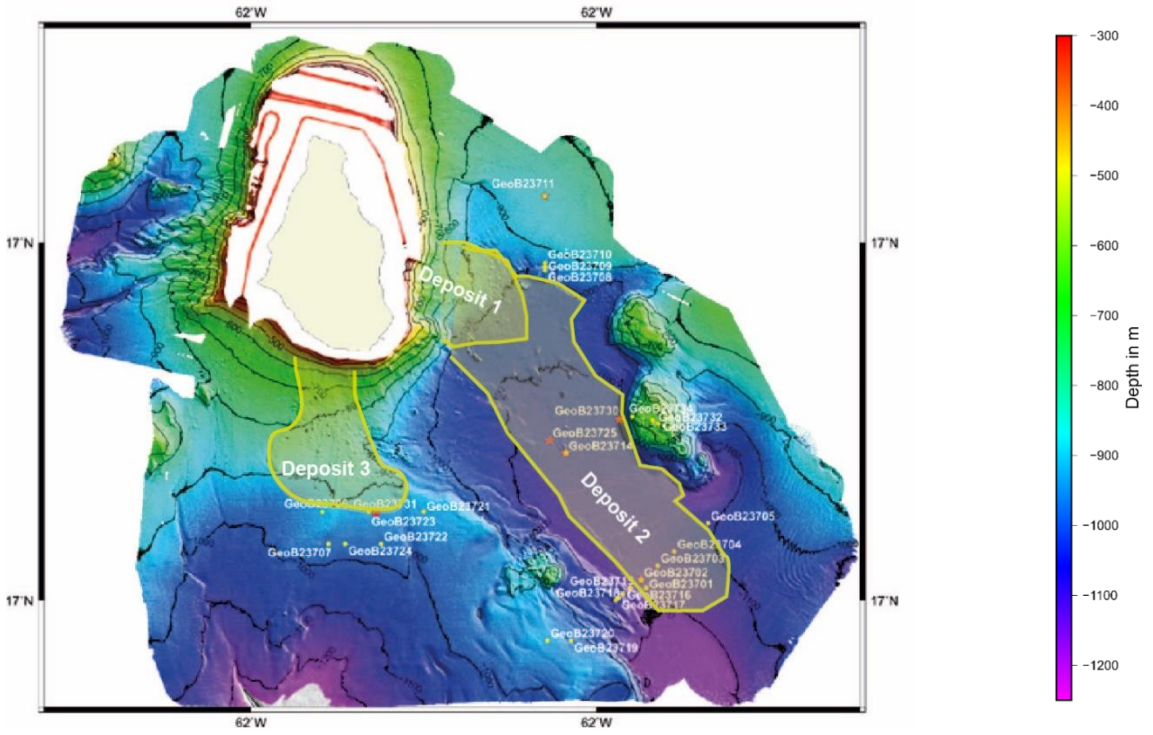

Fig. 3.3: Working area of M154-2 offshore Montserrat. Bathymetry data were collected during both legs M154-1 and M154-2. Gravity core are marked by yellow circles and MeBo sites by red stars.

4 Narrative of the Cruise

(K. Huhn)

Monday, 29 April 2019: After all labs were set up and the MeBo70 equipping was successful completed with the harbour basin test, we left after lunchtime the Port of Pointe-à-Pitre (Guadeloupe). After a short transit of 7 h, we arrived in our research area offshore Montserrat and immediately continued with the hydro-acoustic mapping of the target area, SE of the island.

Tuesday, 30 April 2019: In the course of the morning, we collected five gravity cores in a transect across the distal part of the largest near-surface landslide deposit offshore Montserrat Deposit 2 (GeoB23701-GeoB23705). Core penetration depth was between 0.73 mbsf (GeoB23701) and 2.98 mbsf at the site also selected for the first MeBo drilling (GeoB23702). Afterwards a Sound Velocity Profile (GeoB23702-2) was recorded at this site and MeBo70 was launched into water in the afternoon for its first operation (GeoB23702-3). During this first deployment, a newly developed CPT (cone penetration test) probe was successful utilized to a depth of 12.6 mbsf, where the CPT hit a very stiff, sandy layer; and measurements were stopped.

Wednesday, 1 May 2019: Following the CPT measurements, the flush tool was used to drill to the final borehole depth of 28.65 mbsf without coring. An Acoustic probe was successfully deployed in the borehole to measure a continuous v_p velocities profile from 27.7 mbsf to the seafloor while

the drill string was dismantled. MeBo was back on deck at 8:00 p.m. The following night was used to continue hydro-acoustic mapping.

Thursday, 2 May 2019: In the morning, we continued our gravity coring program along the distal part of the Deposit 3 south of the island (GeoB23706-GeoB23707). During the last deployment GeoB23707, the gravity corer was bent and could penetrate only to a depth of 0.47 mbsf. After another gravity coring at site GeoB23702, MeBo was deployed a second time at this site at 2 pm (GeoB23702-5). Aim was to core the slid masses of Deposit 2 down to the potential glide plane and to recover undisturbed sediment sections underneath. Based on the sediment-physical data collected during first deployment, MeBo drilling parameters were adjusted.

Friday, 3 May 2019: Drilling of GeoB23702-5 was continued until Friday afternoon to a final depth of 30.3 mbsf. After drilling, the magnetic susceptibility probe was lowered in the borehole and mapped in situ while the drill string was dismantled. MeBo70 was back on deck at 9 pm. Core recovery was 56.87%. All cores were first scanned with the MSCL before whole rounds were taken and all cores were split and processed: (a) photos were taken using the smart CIS 1600 Scnanner. (b) A first visual core description revealed that Deposit 2 is overlain moderately bioturbated hemipelagic muds interbedded with normally-graded silts and sands, with cm to dm thicknesses, deposited by mass flows and density. Parts of the MeBo core recovered mixed hemipelagic and volcanic lithologies, above the coarse gravel, while lower stratigraphy included volcanic beds with pumice clasts. Similar sediments could be observed in all cores recovered during M154-2 (see below). (C) Sediment physical properties were measured (chapter 5.3.5). During the entire cruise, all cores (MeBo and gravity) were processed following this procedure. The following night was used to continue hydro-acoustic mapping.

Saturday, 4 May 2019: The day was organized by the same pattern. After hydro-acoustic mapping until 8 am, the morning and early afternoon were used for gravity coring (GeoB23708-GeoB23711). Cores were taken along a NS-trending profile along the northern headwall of Deposit 2 crossing a prominent canyon structure Here, gravity corer could not penetrate into the sediment. In contrast, just north of the canyon in the area of undisturbed, not destabilized slope sediments, material could be collected from the upper 1 m of the sediment bed. At 3 pm, MeBo was deployed at site GeoB23711 in the undisturbed slope area to utilize the CPT probe during a first operation (GeoB23711-2). CPT measurements were collected until a depth of 11.65 mbsf where again a layer of very stiff and solid sediments were reached. MeBo operation was stopped and the drill tool was back on deck at 12 pm. We continued with hydro-acoustic mapping.

Sunday, 5 May 2019: After hydro-acoustic mapping until 2 pm, MeBo was deployed again at site GeoB23711 with the major aims to drill (a) material from the undisturbed slope to gain a deeper insight into background stratigraphy of the area, (b) the basal failure plane of Deposit 2 and a spill-off of Deposit 1 as well as (c) the undelaying strata. This will enable to shed light on the age and timing of the different collapses and slid events.

Tuesday, 7 May 2019: MeBo was back on deck at lunchtime after drilling GeoB23711-3 down to the target depth of 65.3 mbsf. Core recovery was 41 % and we could recover material from all lithological sequences. Afterwards the borehole was logged over it’s entire length with the Acoustic probe. During the second half of the day, the box corer (GeoB23712-1, 2) and the grab sampler (GeoB23713-1) were used to sample the seafloor near the MeBo site. In addition, these

deployments served primarily to test the newly installed camera system what worked after initial difficulties. The b/w image of the camera enable at least the visualization of coarse structures of the seabed. The rest of the day was used for further hydro-acoustic mapping.

Wednesday, 8 May 2019: Directly after lunch, MeBo was deployed again at site GeoB23711-4 for 60 h until 10th May midnight. Major aim of this leg was (i) to utilize the CPT probe, which was successful until a depth of 23.7 msbf. Further penetration was impossible because of increasing sediment strength and stiffness. (ii) to drill to the target depth of 70.30 mbsf. Alternating the special flush tool and the drill tool were utilized and in total 26.6 m sediment cores could be recovered. Sediments are very well-stratified with frequently embedded volcanic ashes and coarse grained volcanic sandy materials. (iii) Finally the magnetic susceptibility probe was lowered in the bore string. Unfortunately, it got stuck in the drill string due to sediment penetrating from below and did not measure. The rest of the night was used to continue the hydro-acoustic mapping.

Saturday, 11 May 2019: In total 10 gravity cores were collected during this day (GeoB23714-1 – GeoB23720-1) along a profile perpendicular the southwestern flank of the Bouillante-Montserrat graben (Fig. 3.1; Fig. 3.3). Attached to the gravity corer, a heat flow probe was lowered into the shallow sediment section. Heat flow measurements were successful and a significant heat flow peak of 260 mW/m² was measured at site GeoB23715-1. These values indicate active fault zones at this outer rim of the graben. Early in the evening, MeBo was deployed again at the central part of the slid masses (GeoB23714-2). Shortly after the start of drilling, the drilling had to be stopped in a depth of 5.30 mbsf as MeBo sank in strongly and tilted slightly. We have therefore decided to briefly lift MeBo a few meters into the water column, move it a few meters and start flushing down (GeoB23714-3); as the aim was not to drill rather to collect in situ measurements with the Acoustic and magnetic susceptibility probes.

Sunday, 12. May 2019: Early in the afternoon at 4 pm, MeBo had to be recovered after reaching a depth of 20.3 mbsf because of a broken flush tool. This could be repaired very quickly and already after five hours MeBo was deployed again at this site (GeoB23714-4). It flushed down to a depth of 12.7 mbsf and started drilling with the aim to recover core material from the boundary layer at the base of Deposit 2b.

Monday, 13. May 2019: After 2.6 m drilling, the drill string has gotten stuck and we had to finish this site. MeBo was back on deck at 1 pm. However, core recovery for the drilled sections was 87%. The material exhibit a very high stiffness, which is why, for example, sediments could not be removed from the core catcher. The samples could only be obtained by cutting the core catcher. In addition, very coarse volcanic material stuck at the base of this section what clearly explains the difficulties during drilling. At 3:30 pm, gravity coring was continued at five locations (GeoB23721-1 – GeoB23724-1) along an east-west trending profile cutting the southern edge of Deposit 3 south off Montserrat. The same evening after less than 10 hours of maintenance, MeBo was deployed at site GeoB23725-1 slightly north-west of site GeoB23714. The aim was again to sample the slid masses from Deposit 2 at specific depth levels both above and below the potential interface between Deposit 2a and 2b. Comparison of the sediment in both sections should enable to shed light on the timing between both slid events.

Wednesday, 15. May 2019: After drilling down to 41 mbsf, MeBo was back on deck at 6:30 pm. With the aim to sample specific depth sections, it was first flushed down to 25.3 mbsf and one core

section was drilled from 25.3 mbsf. Then we washed down again and cored again from 40.3 mbsf. Core recovery in total was 48 %. While the drill string was dismantled, the borehole was logged with the Acoustic probe. The rest of the night was used to test the camera system attached to the box corer and to collect volcanic samples at the seafloor (GeoB23726-1 – GeoB23729-1). Finally, we continues with hydro-acoustic mapping.

Thursday, 16. May 2019: Still with the aim to sample Deposit 2 and additionally to test the hypotheses that this mass wasting event might overspill the volcanic cones, GeoB23730 was selected right at the foot of the volcanic cone. MeBo was deployed at site GeoB23730-1 at 2 pm. Target depth was reached at 25.3 mbsf and the borehole was logged with the Acoustic probe.

Friday, 17. May 2019: MeBo was recovered at 2 am. Afterwards, volcanic samples should be collected with the grab sampler and the box corer north of the volcanic cones along the north-western flank of the Bouillante-Montserrat graben (GeoB23726, GeoB23727). The material turned out to be very difficult to sample because of the high sand content. Penetration depth was very poor. After a short transit to the area of Deposit 3 south off Montserrat, MeBo was deployed at site GeoB23731-1 at 3:30 pm. This site was selected to sample an area south of Montserrat to gain a deeper insight into the stratigraphy at different sections of the volcano.

Saturday, 18. May 2019: MeBo was recovered at 2 pm after drilling down to 25.3 mbsf and a successful logging of the borehole from 22.7 mbsf up to the seafloor with the Acoustic probe. The next few hours were used to collect sample the inner parts of the volcanic cones which border the Bouillante-Montserrat graben (GeoB23732 – GeoB23734). Still less is known about the age of these volcanoes. In addition, sediment samples should enable to test the hypotheses regarding the exhumation of these cones above the sea-level. Penetration into the sediments were impossible. There is no evidence of sedimentation in the cones from gravity coring. At 8:30 pm, MeBo was already maintained again and ready for the second deployment at site GeoB23731. Aim of the operation was to utilize the CPT probe in depth levels between 4.4 – 7.1 mbsf, 7.2 – 7.6 mbsf, and from 9.2 mbsf down to the target depth of 29.2 mbsf beneath the potential glide plane of Deposit 3. In addition, further geophysical data were collected insitu in the borehole. The Spectrum Gamma Instrument has been used successfully whereas the magnetic susceptibility measurements failed.

Sunday, 19. May 2019: MeBo operation at site GeoB23731 was finished at 2 pm. Based on the very good results of the borehole measurements, we decided to log again GeoB23711 at the undisturbed slope section north of Deposit 2 with the Spectrum Gamma Instrument and the magnetic susceptibility probes. MeBo was therefore deployed again at GeoB23711 at this site at 8 pm. It was flushed down to 55.3 mbsf and both probes logged successful the borehole of the entire depth.

Monday, 20. May 2019: Site GeoB23711-5 was finished at 2 pm. Since we had also decided for the next deployment against sediment sampling and for insitu measurement, the short transit to the site GeoB23725 was sufficient for maintenance of the MeBo. MeBo could be deployed already 4 hours and started flushing down to the target depth of 55.3 mbsf.

Wednesday, 22. May 2019: After the flushing down, the Spectrum Gamma Instrument has been used successfully and the magnetic susceptibility probe was lowered in the borehole and mapped insitu while the drill string was dismantled. The recovery of MeBo was more difficult as in any other location during this expedition. With the target of 55.3 mbsf, the entire shallow part of

Deposit 2 was penetrated as well as the upper portion of Deposit 2b. As already observed during the first deployment at this site (GeoB23725-1), the sediments of Deposit 2 seems to be very stiff exhibiting a very high cohesion and shear strength. The drill string seemed to be almost cemented in the sediment. After passing the boundary between Deposit 2a and 2b recovery relieved again recovery velocity increased. MeBo was back on deck after a final successful deployment at 4 am.

Thursday, 22. May 2019: After a short transit we reached the Port of Pointe-à-Pitre (Guadeloupe) at 8 am and started immediately with demobilisation of our equipment.

5 Applied Methods and Preliminary Results

5.1 Hydroacoustics

(M. Kühn, M. Hornbach, K. Pallapies)

5.1.1 Bathymetry

Bathymetrical mapping is a method used to create a map of the seafloor topography. It works by sending acoustic waves into the water column and receive the reflections from the seafloor. Depending on the water depth, it is a fast method to get an overview about seafloor surface structures in the working area. These maps can be used for further cruise planning, for example to decide where to acquire new Parasound profiles or to calculate seafloor slope angles to exclude positions with high slopes as MeBo drilling locations.

5.1.1.1 System Setup and Method

RV METEOR is equipped with two Kongsberg Maritime multibeam echosounder (MBES; Fig. 5.1). The EM122 system operates at 12 kHz and covers water depths from 20 m below the transducers up to full ocean depth; while the EM710 system offers a frequency range from 40 - 100 kHz of signals for water depths ranging from 3 m below transducers to roughly 1000 m. Two different transmit pulses can be selected: a CW (Continuous Wave) or FM (Frequency Modulated) chirp. The sounding mode can be either equidistant or equiangular or mixed, depending on operation preferences and requirements. Both systems can be operated in single-ping or dual-ping mode, where one beam is slightly tilted forward and the second ping slightly tilted towards the aft of the vessel. The whole beam can also be inclined towards the front of the back and the pitch of the vessel can be compensated dynamically. The EM122 system produces 432 beams covering a swath angle of up to 150° while the EM710 system produces 432 beams for a maximum swath angle of 140°. Both systems offer a high-density beam-processing mode with up to 800 soundings per swath. The swath angle, however, can be reduced if required.

The transducers of both multibeam echosounder systems of RV METEOR are mounted in a so-called Mills cross array, where the transmit array is mounted along the length of the ship and the receive array is mounted across the ship. The system on RV METEOR is of a 1° x 2° design. The EM712 system installed on RV METEOR is of a 1° x 1° design, but transducers are much smaller.

The echo signals detected from the seafloor go through a transceiver unit (Kongsberg Seapath) into the data acquisition computer or operator station. In turn, the software that handles the whole data acquisition procedure is called Seafloor Information System (SIS). In order to determine the point on the seafloor, where the acoustic echo is coming from, information about the ship's

position, movement and heading, as well as the sound velocity profile in the water column are required. Positioning is implemented on board RV METEOR with conventional GPS/GLONASS plus differential GPS (DGPS) by using either DGPS satellites or DGPS land stations resulting in quasi-permanent DGPS positioning of the vessel. These signals also go through the transceiver unit (Seapath) to the operator station. Ship's motion and heading are compensated within the Seapath and SIS. Beamforming also requires sound speed data at the transducer head, which is available sound velocity probe. This signal goes directly into the SIS operator station. Finally, a sound velocity profile for the entire water column can be obtained either from a sound velocity probe or from a CTD (conductivity, temperature and density) probe. The temperature (T), salinity (S) and pressure (p) data acquired by any CTD (conventional or mounted on the AUV) can be converted into sound speed by using a sound speed function C(S,T,p). During cruise M154-2, we used direct sound velocity measurements with a special profiler probe (GeoB23702-1).

In addition to bathymetric information, both the EM122 and the EM712 system register the amplitude of each beam reflection as well as a sidescan signal for each beam. During cruise M154-2 the following settings of the Kongsberg EM122 system were used. The pulse was FM, ping mode was set to HD-equidistant, dual ping mode was set to fixed, and depth mode was set to automatic. The beam angle was reduced to 120° during most of the survey, except for survey lines close to the volcanic island and during transit, where maximum coverage was desired. Survey speed varied between 5 knots and 8 knots. Acquisition parameters for the EM710 system were the same as those for the EM122, except for the beam angle, which was reduced to 100° during most surveys. Unfortunately, the quality of the data acquired with the EM710 was insufficient. Therefore, we decided to switch the system off, except for a few profiles in shallow waters (<900 m).

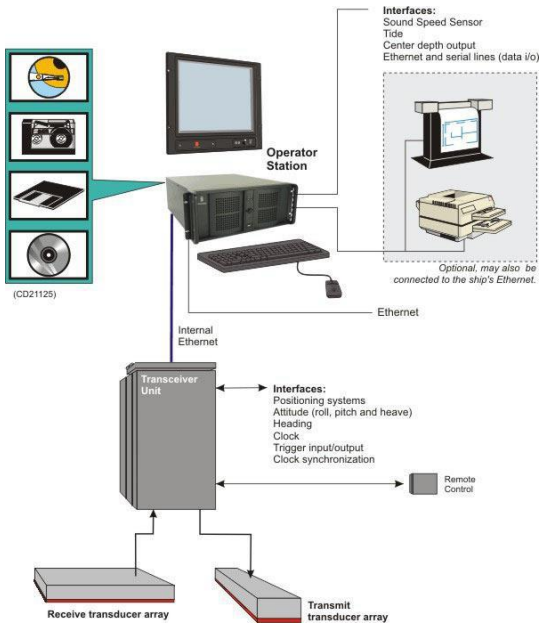

Fig. 5.1: Sketch of the MBES system aboard RV Meteor.

During transit, EM122 data were collected despite higher ship's speed of up to 13 knots. Water column data were recorded at dedicated surveys. One sound velocity probe (SVP) cast was used for a water sound velocity profile, measured at the first MeBo drilling site. Data processing has been carried out on board using the software package MB Systems. Within MB Systems the processing and gridding of EM122 data took place. The soundings were preprocessed from

Kongsberg all-format to an internal MB Systems format (format: 59). The pings were cleaned using mbclean. First, we flagged all soundings with a deviation of 2 % from the local (N=10 pings) median. Second, we applied a swath-filter, which zaps bad rails (30 m) for each swath. Residual bad soundings or spikes were cleaned with the manual 3D ping tool (mbeditviz). The data were subsequently gridded with MB-Systems using a Gaußian weighted mean with a cell size of 10 – 25 m, depending on the coverage and water depth. All data were interpolated for a maximum of five cell sizes to achieve good coverage for the high-resolution grid.

Backscatter and water column data have not been processed on board, but where stored for post-cruise processing.

5.1.1.2 Preliminary Results

The bathymetry off Montserrat (Fig. 5.2) is diverse, and exhibits evidence for active tectonics, frequent, large mass transport events, and volcanism. Below, we briefly note a few initial observations, provide preliminary characterization and interpretation, and suggest potential paths for future research.

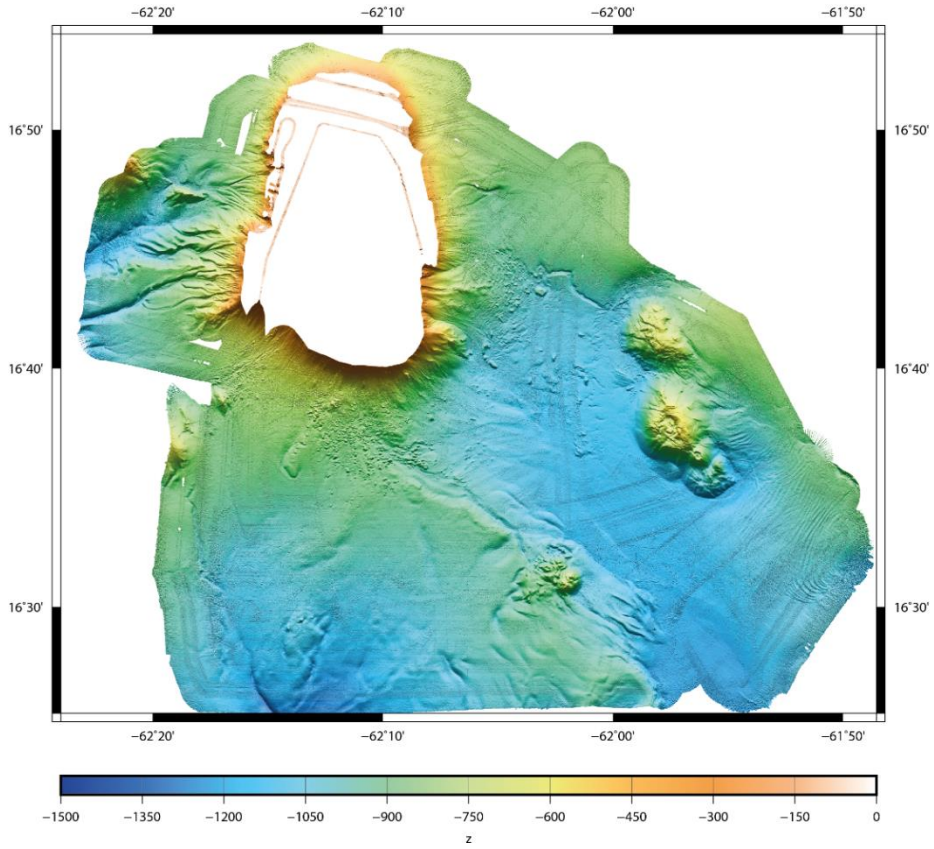

Fig. 5.2: Bathymetric map with data collected on M154-1 and M154-2. Data was gridded with a binsize of 10 m and interpolated with maximum of five cells.

5.1.1.2.1 Bathymetry East of Montserrat

The most significant bathymetric feature east of Montserrat is a NW-SE trending Bouillante-Montserrat overlain by slide debris. The graben is bounded on the north by a slide headwall associated with slide Deposit 2. Analysis of seismic and Parasound data suggests that this headwall may also be associated with a deeper-seated normal fault. The graben is bound to the east by a

series of NW-SE trending volcanic seamounts that extend parallel to the graben and are well imaged in multibeam data. The western edge of the graben terminates with a complex network of en échelon normal faults also striking generally NW-SE, parallel to the graben. These faults appear primarily as folds on the seafloor, however, regional Parasound data confirms progressive deformation and offset with depth, consistent with growth faulting and active extension on the western edge of the graben. There is also evidence for possible submarine volcanism, perhaps associated with intrusion along these faults.

5.1.1.2.2 Bathymetry South of Montserrat

South of Montserrat at depths <1000 mbsl, cobbles and blocks associated with slide Deposit 3 are ubiquitous. Several of these blocks seem to have diameters exceeding 200 m. Further south, at seafloor depths >1000 m, the bathymetry is generally nondescript, with only a few subtle channel systems extending approximately north-south, and a gently dipping seafloor to the south. At the greatest water depths (>1200 mbsf), we observe a series of canyons converging towards the south. To the southeast of Montserrat, we observe a NW-SE trending ridge bounded to the east by normal faults that define the western edge of the graben. We also observe possible submarine volcanic features on the extreme eastern edge of this ridge, as noted previously when describing bathymetry bounding the margin east of Montserrat.

5.1.1.2.3 Bathymetry West of Montserrat

Erosive channels crosscut by active fault systems characterize the bathymetry west of Montserrat. In water depths >1000 m, the dominant bathymetric features are two prominent, subparallel deep-cutting channels trend WSW-ENE. The trend of these channels is approximately conjugate with normal faults mapped east of Montserrat. Closer to Montserrat, in water depths shallower than approximately 800 mbsl, we observe smaller, more sinuous feeder channels that trend generally east-west. In the northwest, however, several feeder channels are crosscut or offset by linear WSW-ENE linear features that we interpret as faults, including a prominent, 1.5 km long fault at 750 – 650 m water depth against which several channels terminate. The strike of this fault is similar to the trend of the two deep canyons, further south. We observe similar discontinuous lineations down slope of this fault, with several cutting through a bathymetric high. The orientation of the fault is consistent with regional strike-slip focal mechanisms. The fault also exists in a seismically active area between Montserrat and Redonda.

5.1.1.2.4 Bathymetry Northeast of Montserrat

Only limited bathymetric data were collected north and northeast of Montserrat, and what little data exist are relatively non-descript. We observe minor lineations running WSW-ENE in shallow water extending from the carbonate shelf. East of northern Montserrat, we also observe several lineations that appear to converge into the slide headwall associated with Deposit 2.

5.1.2 Parasound

5.1.2.1 System Setup and Method

The hull-mounted parametric sub-bottom profiler PARASOUND P70 (Atlas Hydrographic) was operated on a 24-hour schedule for flare imaging and to provide high-resolution (less than

15 cm for sediment layers) information on the uppermost 50 – 100 m of sediment. The system has a depth range of 10 m to >11,000 m (full ocean depth) and a maximum penetration of 200 m. This high sediment penetration is acquired through the high pulse transmission power of 70 kW.

The PARASOUND P70 is a narrow beam sediment echo sounder, providing primary frequencies of 18 kHz (PHF) and adjustable 18.5 – 28 kHz, thus generating parametric secondary frequencies in the range of 0.5 – 6 kHz (SLF) and 36.5 – 48 kHz (SHF), respectively. The secondary frequencies are obtained through nonlinear acoustic interaction of the primary waves at high signal amplitudes. This interaction occurs in the emission cone of the high-frequency primary signals, which is limited to a beam width of 4.5° x 4.5° for the PARASOUND P70. The system consists of four identical transducer modules, each about 0.3 m x 1.0 m. The P70 version includes 384 acoustic elements combined to form 128 stave channels. The resulting footprint size is approximately 4 % of water depth, and vertical and lateral resolution is significantly improved compared to conventional 3.5 kHz echo sounder systems. The system provides features like recording of the 18 kHz primary signal and both secondary frequencies, continuous recording of the whole water column, beam steering, different types of source signals (continuous wave, chirp, barker coded) and signal shaping. Digitization takes place at 98 kHz to provide sufficient sampling rate for the high secondary frequency. A down-mixing algorithm in the frequency domain is used to reduce the amount of data and allow data distribution over Ethernet.

For the standard operation, a parametric frequency of 4 kHz (SLF) and a sinusoidal source wavelet of three periods were chosen to provide a good balance between signal penetration and vertical resolution. The 18 kHz signal was also recorded permanently. Within the survey area the system was mainly used for analysis of sedimentary processes, such as the identification of mass transport deposits, background sedimentation, coring locations for MeBo and tectonic surface deformation. Due to low water depth (>1500 m) within the survey area and a rugged morphology of the seafloor close to Montserrat the system was operated in a single pulse mode.

All raw data was stored in the ASD data format (Atlas Hydrographic), which contains the data of the full water column of each ping, as well as the full set of system parameters. Additionally, a 200 m-long reception window centred on the seafloor was recorded in the SEG-Y and compressed PS3 data format after resampling the signal back at 12.1 kHz. This format is in wide usage in the community and the limited reception window provides a detailed view of sub-bottom structures.

All data was converted to SEG-Y format during the cruise using the software package ps32sgy (Hanno Keil, Uni Bremen). The software allows the generation of one SEG-Y file for longer time periods, frequency filtering (low cut 2 kHz, high cut 6 kHz, 2 iterations), subtraction of mean. If seismic data were collected simultaneously, one SEG-Y file was created for the length of a planned profile. All data was loaded to the seismic interpretation software IHS Kingdom. We used IHS Kingdom to convert the subsequent SEG-Y files from amplitude to envelope data and applied an automatic gain control (AGC) with a filter window of 0.01 s to achieve higher visibility of deeper sedimentary layers. While the AGC filtered data provides good insight on the penetration depth, the envelope data enables a better understanding of the subsurface with high- and low-reflective layers. In addition, the data was converted from time to depth domain with an average velocity of 1500 m/s to select locations for sediment coring and to get sediment thickness information. This approach allowed to obtain a first impression of seafloor morphology, sediment coverage, sedimentation patterns, tectonic deformation and imaging of mass transport deposits.

5.1.2.2 Preliminary Results

In total, more than 1160 km (725 nm) of PARASOUND profiles were acquired (Fig. 5.3). These profiles were mainly used to pin down locations for gravity cores, grab samples and MeBo locations (see chapter 5.4.1). Nevertheless, some of the profiles also revealed geological features that have not been described within the survey area before and are a potential subject of further post-cruise interpretations.

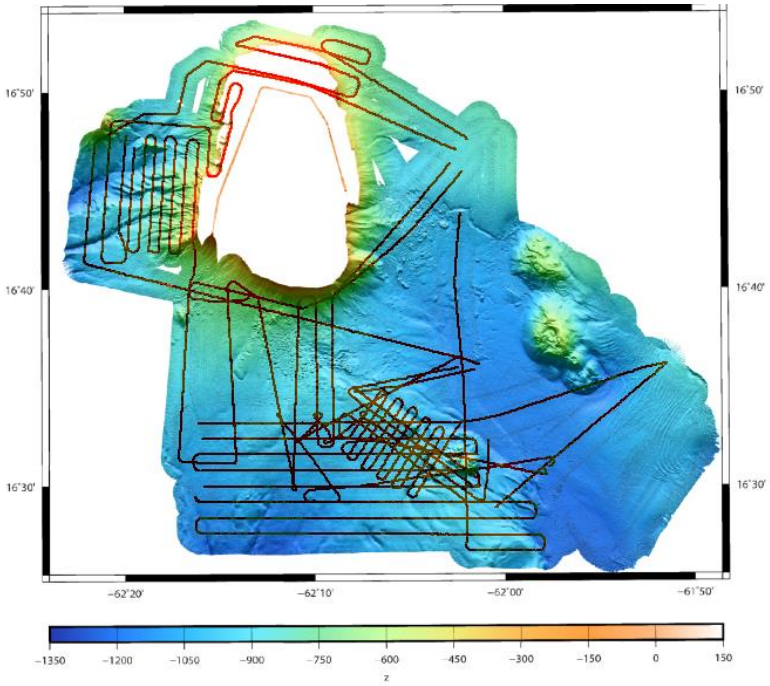

Fig. 5.3: Overview of the acquired PARASOUND profiles during M154-2.

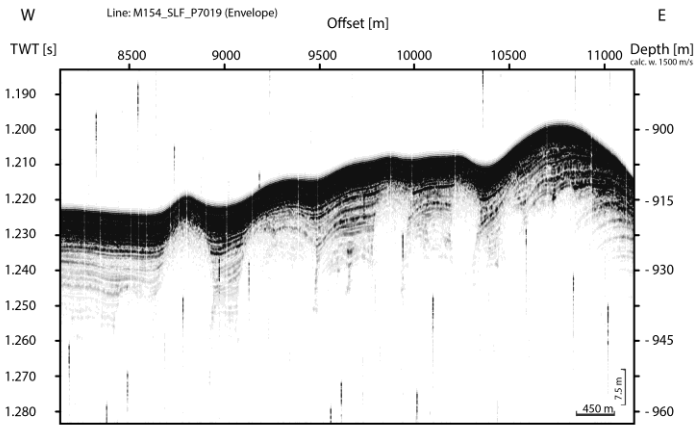

Fig. 5.4: PARASOUND profile south of Montserrat. Several acoustically blanked structures are visible, partly bending the overlying stratigraphy.

The structures shown in Fig. 5.5 are characterized by acoustic blanking, extending from the maximum penetration depth of about 30 mbsf to a relatively shallow depth of about 7 mbsf. Inside these blanked zones no stratigraphy observable, in contrast to well-stratified surroundings.

5.2 In-situ Borehole Measurements

(T. Freudenthal)

5.2.1 Geophysical Borehole Logging

5.2.1.1 System Setup and Method

The borehole logging tools that are used with the MARUM-MeBo70 drilling system are autonomous slim hole tools. They are equipped with a memory logger containing batteries and data logger for measuring the physical formation properties in the borehole in an autonomous mode. When the maximum coring depth is reached, the inner core barrel is replaced with one of the borehole logging tools. During this expedition, we used an Acoustic probe, a Magnetic Susceptibility Instrument and a Spectrum Gamma Instrument (SGR). The Spectrum Gamma Instrument was hooked up inside of the drill string using a wire. The Acoustic Instrument, as well as the Magnetic Susceptibility Instrument are located below the drill bit and are hooked up the borehole together with the drill pipe during recovery of the drill string (logging while tripping). Tripping speed was about 0.6 m to 1 m per minute. The depth of the drill bit and of the wire latching device are recorded by the control system of the MeBo. The GeoBase software package is used to combine the depth information with the sensor readings.

The Acoustic probe is used for measuring p-wave velocity in the formation. The probe is equipped with a transmitter and two receivers located 90 cm and 100 cm below the transmitter. An acoustic pulse was omitted every two seconds. The waveform is recorded by the receivers and afterwards analysed for runtime of the p-wave refracted at the borehole wall. The GeoBase software package calculated the p-wave velocities from the runtime difference at the two receivers. The Acoustic probe also is equipped with a temperature sensor measuring the temperature of the borehole fluid. The Antares 1188 Memory Magnetic Susceptibility Instrument uses three coils for measuring the magnetic susceptibility within the formation. The spacing between the upper transmitter coil and the lower receiver coil is 20 cm. A small compensation coil is located below the transmitter coil. The transmitter transmits an alternating magnetic field tuned to resonate at 1 kHz. The compensation coil is used to compensate for near-instrument effects e.g. induced by well bore fluids. The compensation coil signal is subtracted from the receiver signal. The resulting signal is analysed for the quadrature part that is proportional to the magnetic susceptibility of the surrounding formation. The measurements are corrected for temperature influences on the instrument. The Antares 1460 Spectrum Gamma Instrument contains a 250 mm-long caesium iodide crystal, 38 mm in diameter, connected to a photo-multiplier. Light impulses that are generated by gamma ray collisions with the scintillation crystal are counted and analysed concerning the energy spectrum. The three naturally occurring gamma ray emitters – potassium (K), uranium (U) and thorium (Th) – generate different energy spectra. A GeoBase software package calculates the best fit for the spectra. By combining the results of the Spectrum fit with the gamma ray counts the concentrations of K, U, and Th are calculated.

5.2.1.2 Preliminary Results

An overview of the deployment of the borehole logging tools during the cruise M154-2 can be found in chapter 5.3.1.2. Strong variability in the geophysical properties of the formation was observed in the data of all three probes (Fig. 5.5). The susceptibility and natural gamma ray intensities will help to distinguish between biogenic/siliciclastic material and material of volcanic

origin, while p-wave velocity variations may indicate changes in grain size, mineralogy and consolidation of the sediments.

5.2.2 Cone Penetration Testing

(J. Kuhlmann)

A new MeBo (Freudenthal and Wefer, 2007) in-situ apparatus for static cone penetration testing (CPT) was used during the cruise, after its first deployment during cruise M149 in a mud volcano proved successful. Its main goal is to conduct CPT testing using the MeBo drill rig to provide in-situ data about sediment strength and pore water pressure.

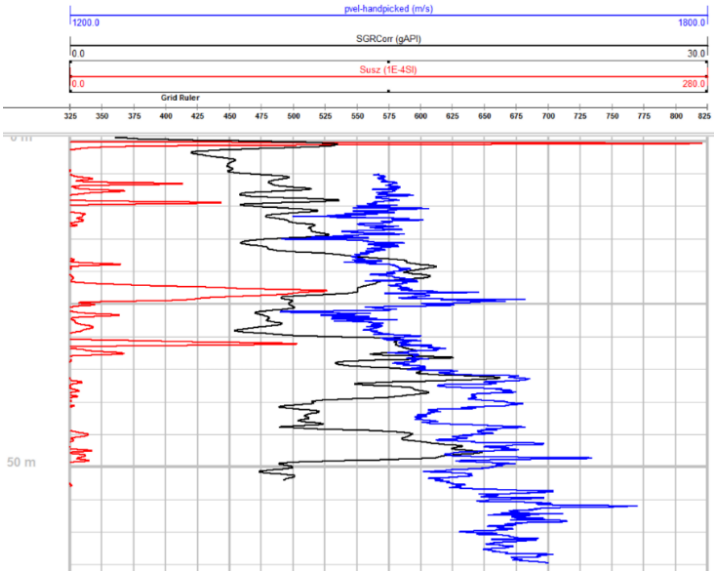

Fig. 5.5: Borehole logging data acquired at site GeoB23711. Shown are the p-wave velocity (blue), the natural gamma ray intensity corrected for attenuation effects by the drill string (black) and the magnetic susceptibility (red) versus drilling depth.

5.2.2.1 System Setup and Method

The main part of the CPT probe is a commercial tip from “Geomil Equipment B.V”, which is able to measure tip resistance and sleeve friction (Figs. 5.6 - 5.8). An additional u2 port is connected to an external Keller 200 [bar] absolute pressure sensor. Data can be continuously logged at a rate of 100 Hz for more than 30 hours at a maximum water depth of 2000 m.

The entire probe consists of five basic components (Fig. 5.7). The MeBo linkage (Component 1) serves as a coupling for the MeBo elevator, which during normal drilling operations is used to recover the inner core tubes. The rear housing (Component 2) is a closed pressure housing containing the electronics (data logger) and the battery packs. The docking shoulder (Component 3) reduces the outer diameter from 70 mm to 59.5 mm so that the CPT probe can attach to the neck of the front drill string. The front housing (Component 4) serves as an extension in order to achieve a greater distance between drill bit and measuring tip and holds place for the pressure sensor. The Geomil tip connecter (Component 5) reduces the outside diameter further from 59.5 to 44 mm, which corresponds to the extent of the Geomil tip.

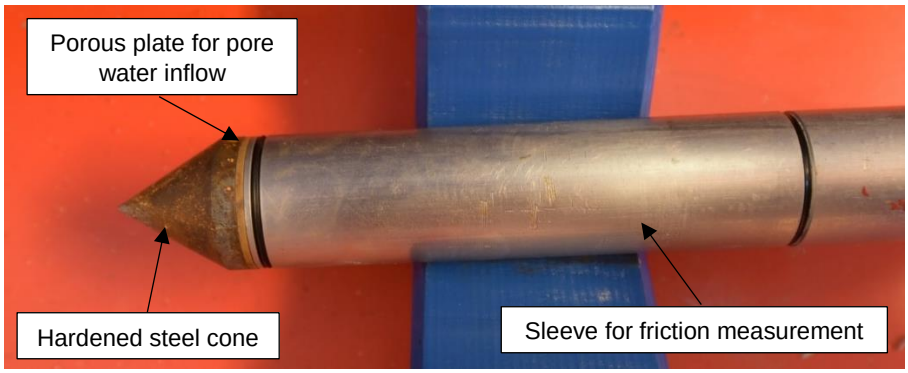

Fig. 5.6: Close-up of the Geomil tip with hardened steel cone and porous plate for passage of pore water.

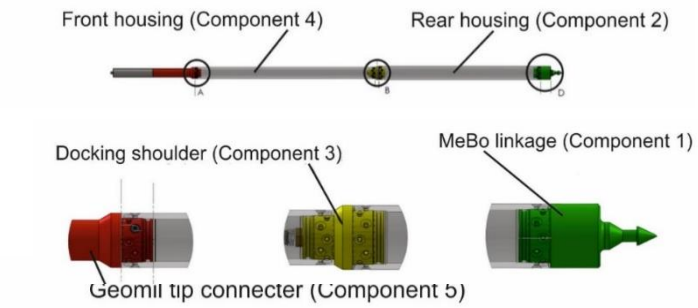

Fig. 5.7: Schematic representation of all basic components of the MeBo CPT.

During operation, the cone tip protrudes 1.4 m from the end of the drill barrel, hence allowing for the measurement of cone and sleeve resistance as well as pore water pressure in an environment not disturbed by the drilling process (Fig. 5.6). Once the probe is deployed, CPT testing is initiated by pushing with a target velocity of 1.5 – 2 cm/s, while the length of a drilling rod (i.e. 2.5 m) limits the maximum pushing distance of each test. Accordingly, further testing for continuous downhole measurements require previous attachment of a new drilling rod.

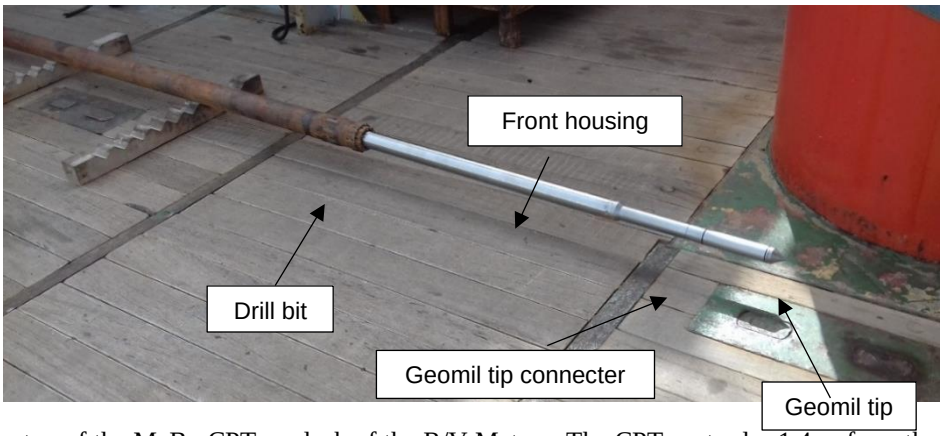

Fig. 5.8: Test setup of the MeBo CPT on deck of the R/V Meteor. The CPT protrudes 1.4 m from the drill barrel, as it will do during operation.

5.2.2.2 Preliminary Results

The CPT probe was deployed during four MeBo stations over the course of the cruise. In general, it was aimed for a semi-continuous downhole pushing to a predefined target depth. Standard procedure included a feed of 35 % and a flushing of 35 – 50 % in order to achieve pushing

speeds of 1.5 – 2 cm/s. Given the sedimentological environment in the study area (presence of several coarse volcanoclastic layers) and the inability to rotate the drill bit during CPT pushing, pushing had to be aborted at several instances due to stagnating advance of the borehole bottom depth. Rotating-while-pushing was tested during the deployment at site GeoB23711-2 to avoid this problem and facilitate pushing, but led to undesired friction at the MeBo linkage of the CPT probe and potential rotation of the probe itself. Instead, whenever push advance ceased, the CPT probe was recovered and re-deployed after flushing the borehole to a desired depth level – usually either the previous position of the Geomil tip or down to the full length of the drilling rod. Pushing was then newly initiated.

After deployment, data processing involves the picking of beginning and ending for each push as well as the conversion of measured data to cone resistance q_c [kN], pressure u2 [bar] and sleeve friction f_s [kN]. An exemplary result of a full MeBo CPT deployment at site GeoB23702-5 is depicted in Fig. 5.9, which shows a general increase of cone resistance and sleeve friction with depth, along with a pronounced anomaly at depth indicating a stronger sedimentary layer at this horizon.

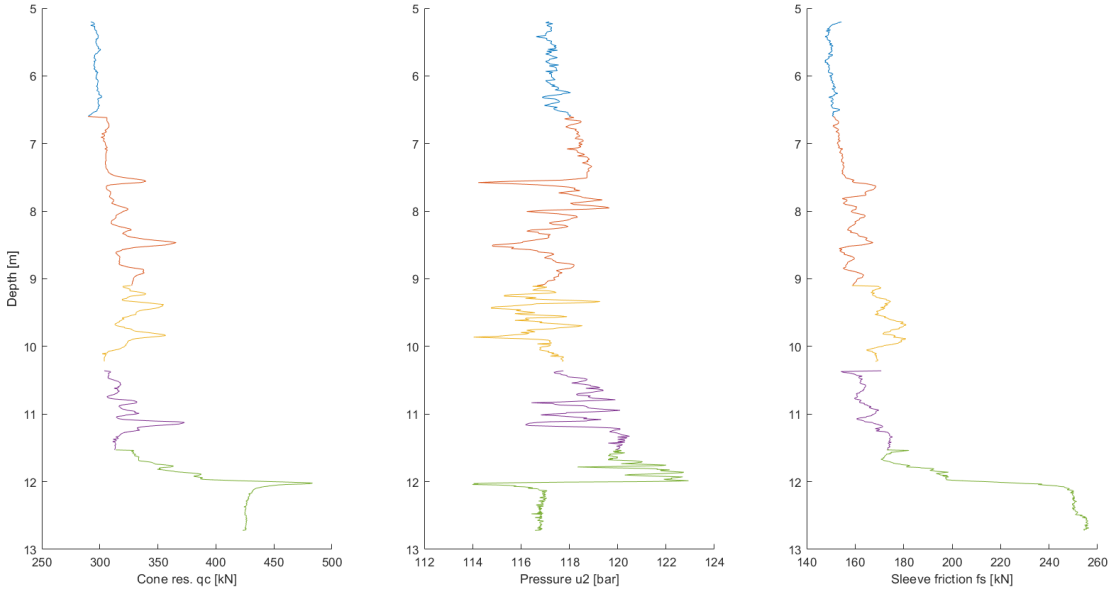

Fig. 5.9: Processed data of the MeBo CPT deployment at station GeoB23702-3 showing a total of five push tests in a depth window of 5.2 m to 12.7 m.

5.3 Sediment Recovery Techniques

5.3.1 Coring Technique

5.3.1.1 Gravity Cores

(K. Dehning, C. Hilgenfeldt)

In order to recover sediment cores from the shallower subsurface, a gravity corer with tube lengths of 1.5 m to 3 m and a weight of approximately 1.6 tons was used (Fig. 5.10). The gravity corer was deployed with the cradle on the starboard side of the vessel which was deployed and recovered using a hydraulic arm that has a maximum carrying capacity of 10 tons. The gravity corer was lowered with an average velocity of 1 m/s until 100 m above seafloor and then with 1.5 m/s until contact. At every station the gravity corer was deployed together with Posidonia navigation placed 100 m above the tool. The gravity corer was equipped with a rigid PVC-liner,

which is used for retaining permanent cores for sediment description, and geochemical and geotechnical analyses. A plastic inner tube was inserted inside the gravity core which is marked lengthwise with a straight line, the so-called Bleil-line, in order to retain the orientation of the core for subsequent analyses. Once on board, the sediment core was cut into 100 cm sections, closed with caps on both ends and labelled according to a standard scheme (see chapter 5.3.2).

A total of 18 gravity cores were recovered during the cruise M154-2. Gravity core deployments are summarized in the station list and shown in Figure 5.11.

Fig. 5.10: Gravity core is lowered into the water.

5.3.1.2 MeBo70 Drill Rig

(T. Freudenthal)

During RV METEOR cruise M154-2, the seafloor drill rig MARUM-MeBo70 (Freudenthal and Wefer, 2009) was used for getting long sediment cores. This device is a robotic drill that is deployed on the seabed and remotely controlled from the vessel. The complete MeBo70-system, including drill, winch, launch and recovery system, control unit, as well as workshop and spare drill tools is shipped within six 20’ containers. A steel armoured umbilical with a diameter of 32 mm is used to lower the 10-tons heavy device to the seabed where four legs are being armed out in order to increase the stability of the rig. Copper wires and fibre optic cables within the umbilical are used for energy supply from the vessel and for communication between the MeBo70 and the control unit on the deck of the vessel. The maximum deployment depth in the current configuration is 2000 m.

The mast with the feeding system forms the central part of the drill rig. The drill head provides the required torque and rotary speed for rock drilling and is mounted on a guide carriage that moves up and down the mast with a maximum push force of 4 tons. A water pump provides seawater for flushing the drill string for cooling of the drill bit and for removing the drill cuttings.

Core barrels and rods are stored on two magazines on the drill rig. We used wire-line core barrels (HQ) and with 55 mm (push coring) and 63 mm (rotary drilling) core diameter. The stroke length was 2.5 m. With complete loading of the magazines a maximum drilling and coring length of more than 70 m can be reached. A tool for flushing down the drill tool can be used instead of

the core barrels. Next to the core barrels borehole logging tools and probe for cone penetration tests can be deployed with MeBo70. Station time can reach more than 24 hrs per deployment.

The MeBo was deployed 14 times at six stations to conduct core drilling (Fig. 5.11), cone penetration tests (CPT) and borehole logging. In some cases, the drill string was flushed to the target depth either using a push core barrel or using a special flush tool ("Vollbohreinheit". VBE). In total, the MeBo was deployed for 353 hrs. 477 m were drilled. 161 m were cored in total with an average recovery rate of 35 %. Cone penetration tests were conducted at four deployments (see chapter 5.2.2). Borehole logging was conducted at 10 of the 14 MeBo70 deployments. Detailed information on deployment of MeBo, recovery of sediments and borehole logging tool deployments are summarized in the station list.

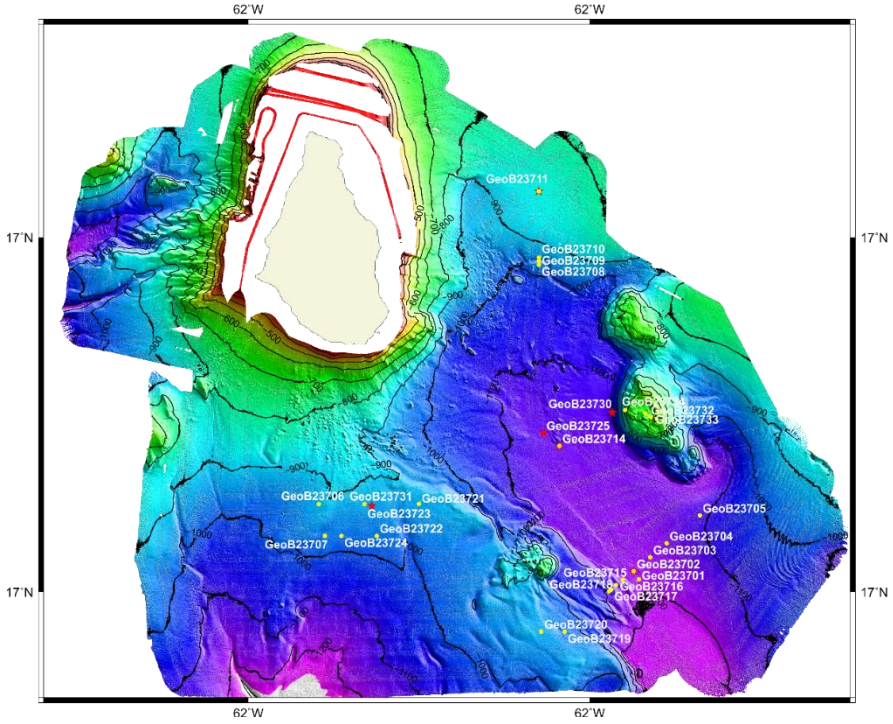

Fig. 5.11: Gravity core (yellow circles) and MeBo (red stars) stations where cores were recovered

5.3.1.3 Box coring

(K. Huhn)

A giant box corer was used to sample surface sediments. The box corer had a diameter of 50 x 50 cm and a height of 55 cm. It was deployed at five stations, one or multiple times (see Station list 7.2). In addition to sediment sampling, a camera system was attached to the box corer in order to obtain seafloor images (Fig. 5.12). These images should enable to identify volcanic rock samples at the surface. After recovery, surface fotos were taken and the entire sediment package was washed to search for potential volcanic rock samples. All black samples identified from

camera fotos turned out to be old coral pieces. In non of the samples, volcanic rock materials could be found.

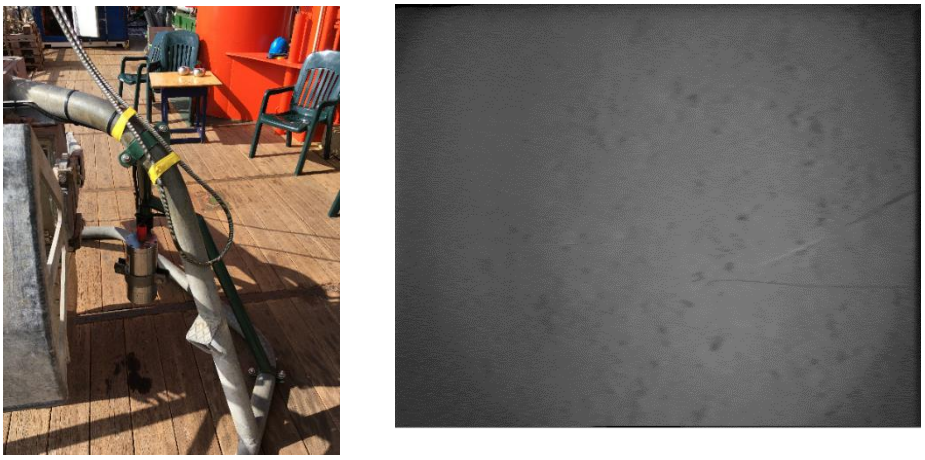

Fig. 5.12: Shows the modified box grab and a first image approx. 7m above ground from the central area of a volcanic cone.

5.3.1.4 Grab sampler

(K. Huhn)

For samples of surface sediments in a volcanic environment, a Van-Veen-type grab sampler was deployed at three locationssee (Station list 7.2). Major aim was to collect volcanic material samples or subsequent age dating, and to and to accomplish box core locations. In all samples, typical sandy surface sediments were collected. No volcanic materials were sampled during these deployments

5.4 Core Curation and Labelling

(B. Meyer-Schack, L. Hönekopp, R. Gatter)

During the cruise M154-2, two types of cores were collected: (1) gravity cores and (2) MeBo cores. For gravity cores, 1.5 m to 6 m long barrels with a liner diameter of 12 cm were utilized. The MeBo cores were drilled with the MeBo70 rig, which can recover up to 70 m-long cores via a push or rotary system, with liner diameters of 5.6 cm and 6.4 cm, respectively.

Once retrieved, the gravity cores were cut on deck into 100 cm long sections. The bottom of each section was sealed with a cap and labelled with the corresponding section number. Each section was closed with caps, taped (black tape for bottom, yellow tape for the top) and labelled (Fig 5.13A). The sections were labelled on both sides, one as archive half and one as working half, and the top and bottom depth were noted on each end of each section (Fig. 5.13B). The core catchers were stored separately in labelled plastic bags.

In contrast to gravity cores, the MeBo70 rig recovers between 1 and 28 core segments, each 250 cm long (i.e. a maximum of 70 m core recovery in total). These core segments were labelled on deck with clips corresponding to their segment number (1 to 28 equalling top to bottom). The core catcher of each segment got a clip with the same number. The sediment in the core catcher was pushed into a short pre-cut liner, and capped, taped and labelled according to Fig 5.13C. While one team prepared the core catcher, the liner team took care of the retrieved core segments. A cap

was taped to the bottom of the liner and labelled with “bottom”. The empty part of the liner was cut were the sediment began and a cap was attached with yellow tape. The liner was labelled with “top”. The segments were cut into subsections and labelled (Fig 5.13C).

After all the liners were labelled, they were cut into two halves along the so-called Blei-line which separates the working and archive halves using a fixed bladed rid and a cheese wire. For storage, each half was wrapped in plastic foil and inserted in a labelled D-Tube.

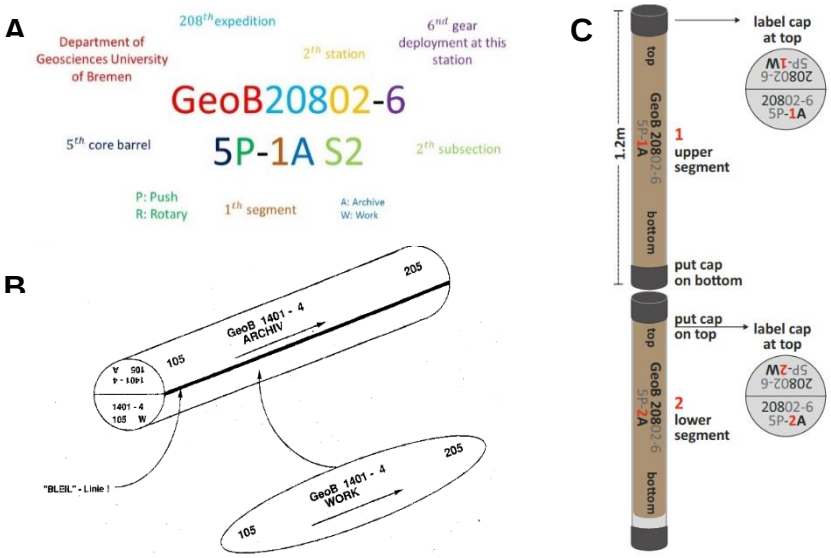

Fig. 5.13: **(A)** Label description. Labelling of gravity cores **(B)** and MeBo cores **(C)**.

5.4.1 smart CIS1600 Line Scanner

(B. Meyer-Schack)

5.4.1.1 System Setup and Theory

During cruise M154-2 all retrieved gravity and MeBo cores were scanned with the Camera Image Scanner smartCIS right after core splitting. The line scanner uses the software smartSCAN and can operate at three different resolutions: 1000 dpi. 500 dpi and 250 dpi. For the cores obtained during the cruise M154-2, a standard resolution of 500 dpi was adapted and a 75 mm lens for core diameters between 30 mm and 200 mm were used.

Different camera settings were used for gravity and MeBo cores as they have different diameters of 56 mm and 120 mm. respectively. The camera settings are listed in Table 5.1.

Tab. 5.1: Camera settings for gravity and MeBo cores.

Settings	Gravity Core	MeBo Core
Diameter	120 mm	56 mm
Distance between core and camera	288 mm	252 mm
Aperture	f = 5.6	f = 4.8
Camera settings	Fine Tune: +20 % Gain: R: 182, G: 163, B: 222	Fine Tune: +30 % Gain: R: 197, G: 176, B: 240

5.4.2 Core Description and Smear Slide Petrography

(S. Watt, S. Kutterolf, C. Sievers)

5.4.2.1 Theoretical Background

This chapter outlines procedures used to document the composition, texture, and sedimentary structures of the sediments recovered during MeBo and gravity core deployments. The procedures include visual core description, smear slide analysis, and digital colour imaging (see chapter 5.3.3). The objectives of this process are twofold: (1) to provide an overview of the sedimentary units encountered within the respective study sites; and (2) to synthesize these observations and assign general sediment lithofacies.

Core sections from the archive halves were used for sedimentological and petrographic observation, after MSCL. Following imaging, the archive-half sections of the sediment cores were macroscopically described, defining lithostratigraphic units by visual inspection and smear slide analysis. Visual inspection of sediments yielded information particularly concerning lithologic variation, colour, sedimentary structures, and drilling disturbance, whereas smear slide analyses were used to identify sedimentary constituents including volcaniclastics, bioclasts and minerals. Mineralogical information gleaned from these slides provides additional support for lithofacies assignments and offered indicative estimates of the lithological composition.

5.4.2.1.1 Core Descriptions and Lithological Logs

Core descriptions are documented on hand-drawn paper graphic logs and subsequently digitalized for a preliminary stratigraphic overview. Native files are included in the data delivery for this voyage report. Files are organised according to study sites and coring methods.

Gravity cores are always contiguous sections (1 m max.) with no core breaks (but not including the core catcher samples), and depth references in the core descriptions are made from the top of the complete core. For MeBo cores, each drill section is logged separately (i.e. 1P. 2P. and 3P etc.) giving both, a) zero at the top of each section (left axis) and b) depths already recalculated to the contiguous hole depth in cmbsf (below seafloor) using the drilling tables provided by the MeBo team where the starting point of each drilled core is provided in cmbsf (continuous depth range of the layers given in the section description). In the case of incomplete core recoveries (normally 2.5 meter per core) the sediments are moved to the top of each core and potential gaps in sediment recovery accumulate at the base of each core, following the IODP procedure. Core catcher sections are included within the logged sequence.

On board core descriptions should be considered as a provisional summary and are not intended to include bed-by-bed graphical depiction. Units of similar character are typically classified collectively, and where appropriate, a text narrative summarizes notable features.

5.4.2.1.2 Lithologic Classification Schemes

Lithologic names for granular sediments are assigned using the scheme illustrated below, which combines aspects of the classification systems used during IODP. Pelagic/hemipelagic, bioclastic and volcaniclastic sediments were the principal materials recovered during M154-2. Basic lithologic groups were modified from the scheme of Mazullo and Graham (1988). If the sediment contained <50 % biogenic debris, then it was classified as either siliciclastic (implied terrigenous)

or volcanoclastic. Sediment with >50 % biogenic debris was classified as hemipelagic, if it had a clay matrix, but a common lithology encountered was a clay-poor biogenic silt or sand, which was classified as bioclastic.

All sediment samples were classified based on texture (Fig. 5.14; see also Shepard. 1954). Components present in amounts of 25 % – 50 % are primary modifiers (e.g. biocalcareous silty clay and tuffaceous silty clay), whereas components of 5 % – 25 % are secondary modifiers (e.g. clayey silt with glauconite). Most of the sediment/sedimentary rock categories shown in Fig. 5.14 contain >50 % particles of <63 µm size (silt and clay). When referring generally to fine-grained sediment or sedimentary rock collectively, the term "mud" (or mudstone) is applied. The term "sand" refers to materials with ≥50 % sand-size particles. All grain size designations followed the conventional Wentworth (1922) scheme as depicted by Folk (1980). Maximum grain size was described based on the terms in the Wentworth grain size classification.

Colour was determined qualitatively for core intervals using Munsell Colour Charts (Munsell Colour Company. Inc., 2000). Visual inspections of the archive-half sections were used to identify compositional and textural elements of the sediment, including rock fragments, sedimentary structures, and diagenetic features such as colour mottling. Sediment and sedimentary rock in this volcanogenic sediment environment were also classified using an approach that integrated the nature of volcanic particles. Where there are ≥25 % volcaniclasts, but <25 % pyroclasts, the sediment was designated as volcaniclastic sand. Where the clast composition is 25 % – 75 % pyroclasts, the sediment/sedimentary rock was classified as tuffaceous sand. However, if the clast composition is ≥75 % pyroclasts, it was classified using the volcanological terms ash (<2 mm) and lapilli (2 – 64 mm) (modified after Fisher and Schmincke, 1984).

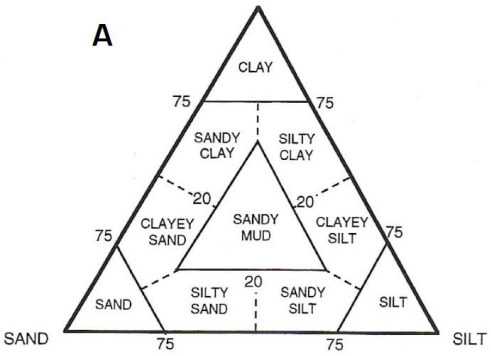

Fig. 5.14: Classification schemes for terrigenous clastic sediments (after Mazzulo and Graham, 1988).

5.4.2.1.3 Functionality of the Graphic Logs

The graphic log presents a lithological column, texture, colour (Munsell notation), lithofacies, presence of any fossils or structures (shown as symbols), information regarding tephra, position of smear slides, notes, and comments. Where core lithologies are highly variable and vertically condensed, most of the narrative is shared between the notes and comments columns, and as such some complex logs will require careful reading. The digitalized sections provide a condensed overview of the lithologies and summarize similar grain sizes into their principal names or an umbrella term (e.g. mud; see Fig. 5.15).

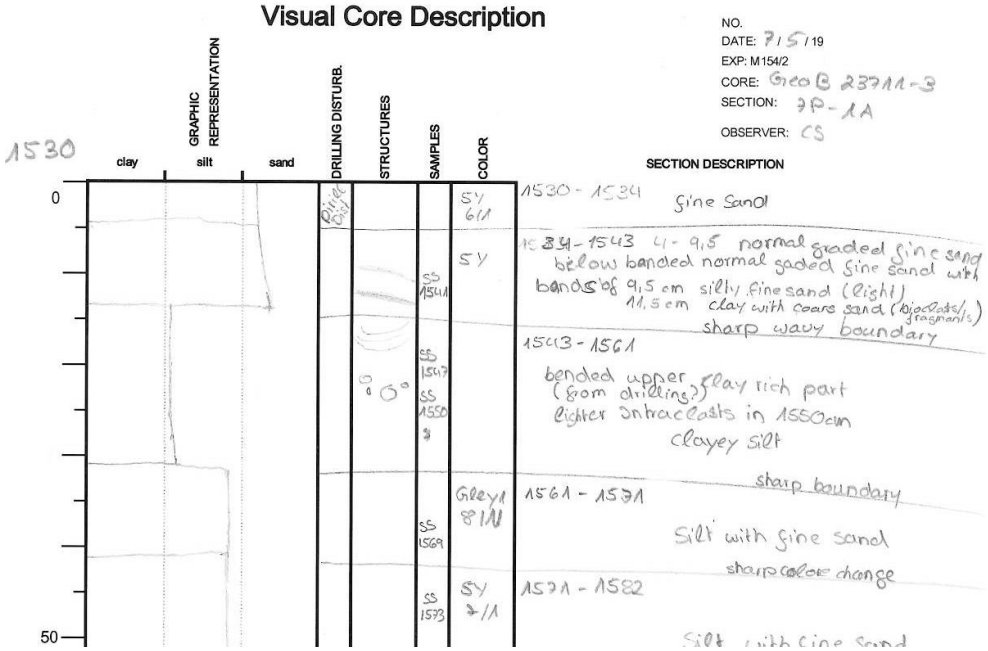

Fig. 5.15: Exemplary graphic log – MeBo core section GeoB23711-3 7P-1A

5.4.2.1.4 Smear Slides

Smear slides provide additional on board and archive information of core mineralogy, texture and composition. Samples are collected to provide representative characterization of the sediments, confirmation of material, or where significant changes in the sediment properties are apparent, including colour, hardness, grain size, bedding, fossils, minerals, deformation, and biological material. These changes also help in the assignment and refinement of sediment lithofacies. A small sample of sediment is scraped using a toothpick in a horizontal fashion perpendicular of the core axis, and dispersed with water on a glass slide, heated and subsequently covered with a resin (Meltmount Thermoplastic Liquid Mounting Media, RI 1.539) and a cover slide. The label applied to each smear slide refers to the depth down-core from where the sample is collected. Terminology used to describe the smear slides is qualitative, with approximations of relative abundance.

5.4.2.2 Preliminary Results

Gravity cores were successfully collected from 17 sites during cruise M154-2 (sites 1 to 6, 10, 11, 15 to 19, 21 to 24), and a separate graphic log has been constructed for each core. In addition, MeBo drilling was undertaken at six separate sites. Some of these sites were drilled by MeBo multiple times, but the aim of some of these deployments was to collect downhole data or to recover core samples only from specific horizons, and the amount of core retrieved on each MeBo deployment is thus variable (for example, even on deployments used for logging. a single core was generally recovered from the top of the stratigraphy). As a result, core samples were recovered multiple times from sites 11 (11-2 to 11-4), 14 (14-2 and 14-4) and 31 (31-1 and 31-2). Graphic logs were constructed for all cores recovered, and are provided alongside a summary of all core recovery details in Appendix A and B (see also station lists). A small number of MeBo core sections (either core catcher samples, particularly from site 2 – 5, or core subsections from other sites) have been left intact as whole-round samples, for later geotechnical analyses, and are thus not currently included in the core descriptions.

Observations made on the visual core descriptions have been summarized into a small number of sedimentary lithofacies, used to construct schematic summary logs. These are based principally on particle size, grading and sorting (particularly mud content), and on the predominance of volcanic or biogenic clasts. The lithofacies thus defined are indicated in Fig. 5.16.

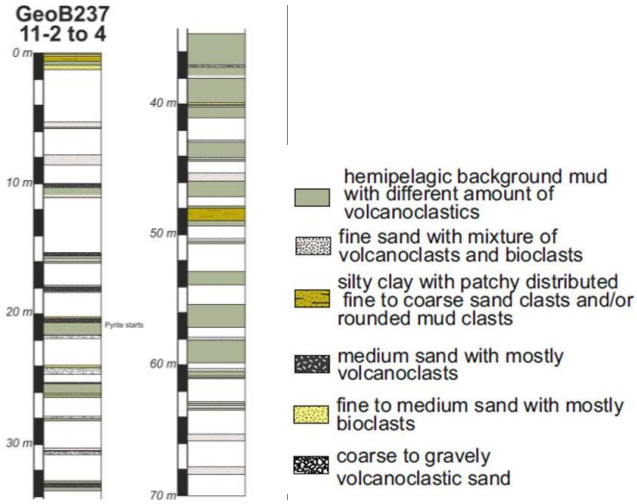

Fig. 5.16: Example digitalized schematic summary log for MeBo core site 11 (drill holes 2 to 4, composite log). The white gaps indicate sections where no material was recovered.

5.4.2.2.1 Overview of Lithofacies

The sediments sampled throughout the area predominantly comprise mud-rich facies (often with a high silt, both volcanic and biogenic clasts, or biogenic sand component) interbedded with better-sorted sands, interpreted in most cases as turbidites. In some cases these sandy intervals show multiple units defined by normally-graded beds or generally sharp colour changes, indicative of variable proportions of volcanic and biogenic clasts. These units with multiple, stacked beds, without intervening hemipelagic sediment, are mapped collectively as a sandy turbidite. Hemipelagic clays show distinct and consistent colour changes across core sites, but have been grouped in the summary logs as a single facies representing background sedimentation.

Bioclastic or mixed volcaniclastic-bioclastic facies are common, and easily distinguished from volcaniclastic sands, which have a mid- to dark-grey colour and a low (<5 %) bioclast content. Throughout the study region, turbidite sands range from coarse- to fine-grained sand deposits, and are generally of decimetre scale. This observation of a seafloor sedimentary sequence dominated by turbidite sands, interbedded with hemipelagic clay, is consistent with previous results from extensive shallow vibrocore and gravity core (<5 m depth) surveys throughout the area (e.g. Trofimovs et al., 2008, 2013; Cassidy et al., 2012, 2013), as well as samples recovered at IODP drilling sites U1395 and U1396 (Le Friant et al., 2015). It is notable that these turbidite sands are predominantly of a bioclastic or mixed volcanicastic-bioclastic composition, rather than volcaniclastic composition, suggesting that prevailing mass-transport processes in the region mobilise seafloor or shelf materials, and may not be directly related to volcanic eruptions or volcanic mass-wasting (i.e. flank collapse) events.

Coarser units are much less frequent, but in a small number of cores coarse volcaniclastic sands to volcaniclastic gravels were encountered. representative of higher-energy transport processes, and generally containing mixed volcanic lithologies.

Tuffaceous deposits (e.g. volcanic ash beds) are less frequent than volcaniclastic turbidite sands, and generally thin (cm-scale or less), sometimes dispersed or patchy, and very fine-grained. A small number of coarser pumice and crystal-rich deposits were identified in some MeBo cores, likely representing fall deposits from relatively large explosive eruptions.

5.4.2.2.2 Shallow Stratigraphy – Gravity Coring

Transects of gravity cores were collected to provide representative samples of the background stratigraphy across the S of the Bouillante-Montserrat graben (sites 1 to 5), up the western margin of the graben (sites 15 to 19), on the platform S of Montserrat (sites 6 and 21 to 24), and on the platform E of Montserrat (sites 10 to 11). Sites 2 and 11 were also the locations of MeBo cores. All these gravity cores successfully retrieved material, with penetration beneath seafloor ranging from about 0.5 m to 3 m. A small number of additional sites failed to retrieve material, particularly within the Bouillante-Montserrat graben close to Montserrat (where it is likely that the thick sandy turbidite from the 1995-2013 eruption could not be penetrated; cf. Trofimovs et al., 2013).

The transect at the S end of the Bouillante-Montserrat graben recovered hemipelagic clays interbedded with fine to medium sandy turbidites, the majority of which were bioclastic or mixed volcaniclastic-bioclastic compositions. Volcaniclastic turbidites sampled near the seafloor are likely to correspond to the 1995-recent eruption and the 1.5 – 2.5 ka andesitic turbidite identified by Trofimovs et al. (2013). Initial visual correlations could be made between cores based on the colour, thickness and broad components of units, but detailed correlations require further analysis (Fig. 5.17). A similar stratigraphy was encountered on the W side of the graben, but penetration here appears to have reached stratigraphically older units, likely due to a reduced sedimentation rate. Similar lithologies were encountered with bioclastic or mixed units more frequent than volcaniclastic units. A consistent stratigraphy was found between cores, although turbidite sands did not always extend across the full sample set. Correlation could also be made, based on visual hemipelagite characteristics and sandy beds, with cores sampled on the platform south of Montserrat. However, penetration in this area was poor (approximately 50 cm for all cores, except at site 6), suggesting a hard or coarse unit is present at this depth.

Several samples were taken from all gravity cores for smear slide analyses. Volcaniclastic sands are relatively pure (i.e. bioclast contents <5 %). and comprise crystal fragments (predominantly plagioclase, with abundant greenish brown and occasionally red hornblende, ortho- and clinopyroxene, with variable proportions of opaques) and volcanic lithics (subangular to subrounded generally microcrystalline dense to vesicular clasts).

Bioclastic sands are rich in foraminifera and, in some cases, in carbonate lithic fragments, with a variety of additional components including sponge spicules, coral fragments, unidentified shell fragments and echinoid fragments, and nannofossils. These sands generally have a minor proportion of volcanic crystal fragments (with plagioclase the most abundant, more seldom pyroxene and hornblende dominated), which in some cases forms a more significant component, defining the mixed volcaniclastic-bioclastic turbidites (on the macroscopic scale, these have a pale grey to greenish colour, contrasting with the paler yellow bioclastic sands, and the mid to dark grey volcaniclastic sands). Intervening clays are rarely pure, but generally silty, with coarser clasts dominated by bioclastic material (dominated by foraminifera. with a variety of other planktonic fragments, c.f. radiolarian and diatoms, but also fragments of benthic species like sponges, corals

and echinoderms), and variable proportions of volcanic detrital crystal fragments (plagioclast, hornblende, pyroxene and opaques) – again consistent with the dominant mineral assemblage forming recent andesites on Montserrat (e.g. Harford et al., 2002).

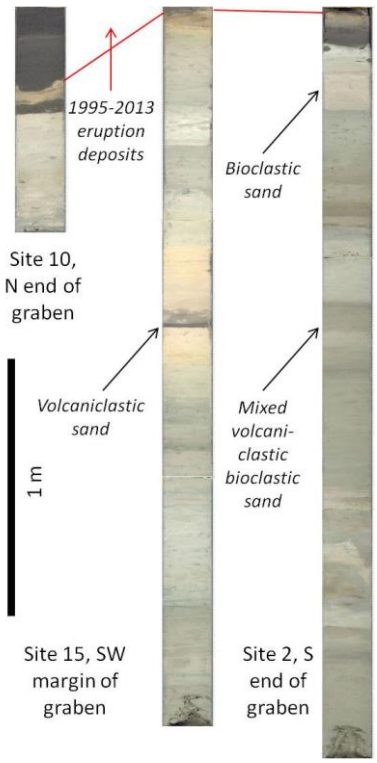

Fig. 5.17: Example scans of gravity cores from across the study area, highlighting unit correlations for the 1995 – 2013 eruption deposits, and the different sand lithologies encountered (interbedded with hemipelagic sediment).

5.4.2.2.3 MeBo Cores

MeBo core samples were retrieved at sites 2, 11, 24, 25, 30 and 31. The first five sites all targeted stratigraphy directly including the Deposit 2 horizon (the main mass-movement target of this research), while site 31 targeted adjacent stratigraphy to the south of Montserrat, providing broader stratigraphic context and also intersecting a separate landslide deposit. Deposit 3, of poorly constrained age (Le Friant et al., 2004; Cassidy et al., 2012).

Recovery of material varied significantly between sites, due to drilling strategies adopted to reach the horizons of interest and overcome challenges in coring lithologies associated with the mass movement deposits.

At site 2, cores were recovered from 0 – 30 m. Lithologies similar to those recovered in gravity cores from the same site were encountered throughout the sequence (interbedded sands, comprising both volcaniclastic and bioclastic material, with hemipelagic clay), with the most prominent interval being a coarse volcaniclastic sand. Other volcaniclastic horizons, including pumiceous deposits, were also encountered (Fig. 5.21).

At site 11, three holes were drilled, with the best recovery during 11-3, and some additional material, aiming to fill gaps in the stratigraphy, during 11-4. This site lay to the north of the graben, intersecting the equivalent horizon to Deposit 2. Overall lithologies were again comparable to

previous sites, but the cores recovered material from greater depths, reaching over 60 m. Bioclastic sands are common throughout the sequence, with several volcaniclastic deposits also occurring, in some cases reaching coarse sand to gravel grade. Initial visual inspection and smear slide analysis suggest bed correlations between sites 2 and 11.

Sites 24, 25 and 30 aimed to sample cores from the central part of Deposit 2, and represented the most challenging drilling conditions. As a consequence, several intervals were washed down, in order to reach target horizons related to the internal structure of Deposit 2 (Watt et al., 2012b). The most successful recovery was from site 24, where both volcaniclastic gravels and finer-grained sands were recovered. These sites also gave good recovery of the youngest stratigraphy, particularly the 1995 – 2013 eruption deposits.

Site 31 aimed to drill through parallel-bedded stratigraphy south of Montserrat, intersecting the Deposit 3 horizon, clearly visible in Parasound profiles at approximately 10 m below the seafloor. Core recovery was relatively low, but retrieved material from most sections. Coarse volcaniclastic sands to gravel were encountered at multiple levels, and more frequently than in any other core site. Material from the Deposit 3 horizon was successfully recovered, in addition to several other units, suggesting a number of volcaniclastic mass-flow deposits are present in the stratigraphy of this area.

Smear slide analyses of hemipelagic and sandy intervals from the MeBo cores indicate very similar lithologies to those analysed from gravity cores. There are variations between some bioclastic sands, in both the nature of the bioclasts and the proportion of carbonate lithics, suggesting some variability in the source regions of these events. The volcaniclastic components appear to be more consistent through time, with similar mineral assemblages, consistent with andesitic volcanism. The MeBo cores penetrate a number of fine-grained ash-rich horizons (i.e. containing glass shards), which were not sampled in the gravity cores, as well as pumiceous horizons, and the range of volcaniclastic deposits is thus greater than evident in the shallowest stratigraphy. This observation is consistent with the lithologies described in IODP 340 drill cores

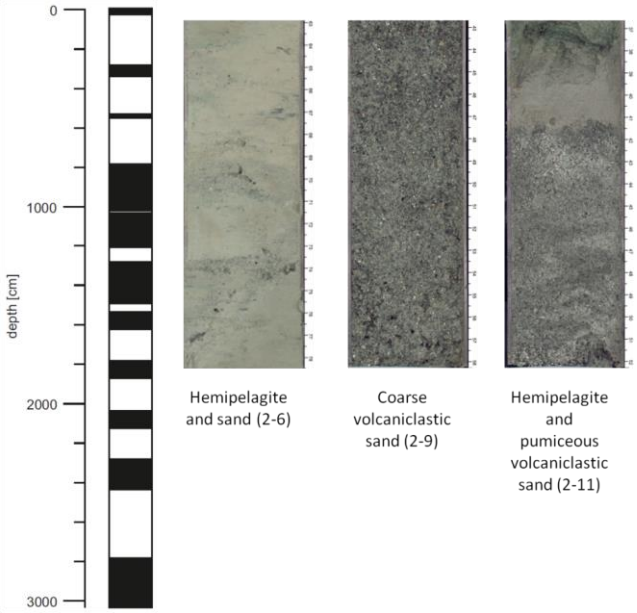

Fig. 5.18: Example lithologies recovered from MeBo coring at site 2. Recovery for the full hole is shown on the left (indicated by black intervals), with examples of lithologies from different parts of the stratigraphy.

(site U1395; Le Friant et al., 2015), and mineral assemblages and coarse grain size of several of the deposit suggests that they are likely derived from eruptions of the Soufriere Hills volcano.

Coarser volcaniclastic deposits were examined visually, rather than by smear slide analyses, and these are consistent in being dominated by dark andesitic lithic clasts, but also containing a wide variety of other volcanic clast types, including pumiceous and altered material. Such mixtures would be expected in sector-collapse related deposits, and are thus consistent with being directly derived from the emplacement of Deposit 2. Combining the visual core description and study of recovered lithologies with Parasound and seismic reflection data, material from the Deposit 2 interval was successfully recovered at MeBo sites 2, 11 (-3 and -4) and 25.

5.4.3 Physical Properties

(J. Kuhlmann, R. Gatter, L. Hönekopp, S. K. Rapp, C. Hilgenfeldt)

Physical properties of marine sediments are reliable quantitative indicators of composition, formation and environmental conditions of sediment deposits. They may serve as proxies for processes such as post-depositional consolidation and early diagenesis. In addition, these parameters may help in core-to-core and core-acoustic, as well as hole-to-hole correlations.

During cruise M154-2, shipboard measurements on sediment physical properties included high-resolution Multi-Sensor Core Logger (MSCL) measurements on the cores before (and after) splitting, as well as fall cone and vane shear tests (for undrained shear strength), and Moisture and Density (MAD) measurements on the working halves of the recovered cores. MSCL measurements were carried out at a resolution of 1 cm. Fall cone tests were taken at a resolution of 10 cm, while vane shear tests and MAD measurements were undertaken at a resolution of approximately 50 cm. All measurements were carried out on both gravity and MeBo cores.

5.4.3.1 Multi-Sensor Core Logging (MSCL)

5.4.3.1.1 Theoretical Background

The sediments recovered during the cruise M154-2 were subjected to routine laboratory geophysical studies: shipboard measurements on the segmented cores were made using a *Multi-Sensor Core Logging System* (MSCLS) that was newly developed at MARUM (Center for Marine Environmental Sciences, University of Bremen; Fig. 5.19).

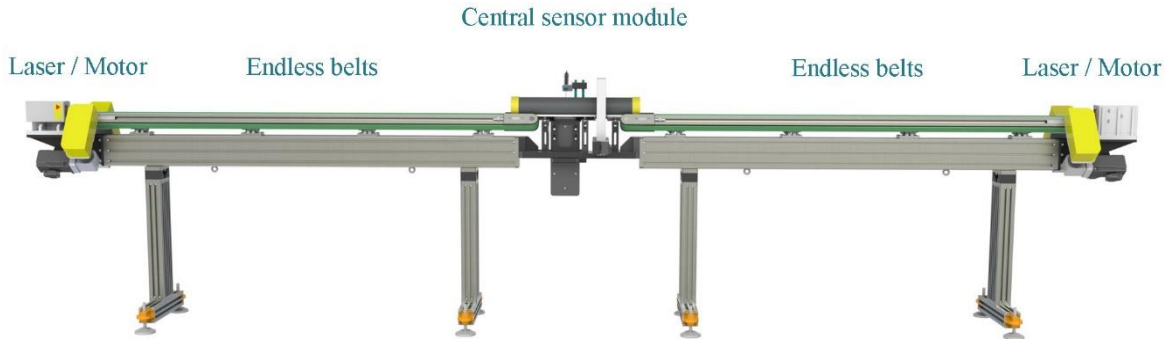

Fig. 5.19: CAD drawing of the Multi-Sensor Core Logging System (MSCLS) consisting of two-sided (endless) conveyor belts, the central sensor module, the drive motors and the laser distance sensors.

The MSCLS measurements routinely comprise two basic physical parameters: (1) electrical resistivity R_s (as a measure of porosity and density) and (2) magnetic volume susceptibility κ.

These properties are closely related to the lithology and grain size of the sediments. Electrical resistivity and magnetic volume susceptibility yield medium-resolution core logs available prior to most other detailed investigations. The characteristic sensor response width for these parameters is approximately 5 – 8 cm.

Magnetic Volume Susceptibility

Magnetic volume susceptibility κ is defined by the equations:

$$B = \mu_0 \cdot \mu_r \cdot H = \mu_0 \cdot (1 + \kappa) \cdot H = \mu_0 \cdot H + \mu_0 \cdot \kappa \cdot H = B_0 + M \quad (5.1)$$

with magnetic induction B, absolute and relative permeabilities μ_0 and μ_r, magnetizing field H, magnetic volume susceptibility κ and volume magnetization M. It can be inferred from the third term, κ is a dimensionless physical quantity. It represents the amount to which a material is magnetized by an external magnetic field. Due to its size, the sensor integrates the response signal over a core interval of about 5 – 8 cm. Consequently, sharp susceptibility changes in the sediment column appear smoothed in the κ log.

Electrical Resistivity. Porosity and Density

The electrical sediment resistivity R_s was determined using an external inductive sensor. A non-contact infrared thermometer is used to measure the temperature at exactly the spot where contemporaneously electrical resistivity is determined. For sensor calibration, a series of saline solutions is measured daily. The porosity ϕ was calculated according to the empirical Archie's equation:

$$\frac{R_s}{R_w} = k \cdot \phi^{-m} \quad (5.2)$$

which approximates the ratio of sediment resistivity R_s to pore water resistivity R_w by a power function of porosity ϕ. Following a recommendation by Boyce (1968) for seawater saturated clay-rich sediments, values of k = 1.30 and m = 1.45 were used. Density estimates were calculated assuming a mean bulk density of 2670 kg/m^3. For inductive porosity and susceptibility proxies, we joined the core section data to an entire core log due to a method-immanent non-linear signal decay toward the section caps. Corrections using an adapted section end correction curve were applied, but some conspicuous peaks and discordances persist at some section boundaries and should not be over-interpreted.

5.4.3.1.2 System Setup and Methods

General Setup of the MSCLS

Magnetic susceptibility, electrical conductivity and temperature are measured by the MSCLS and recorded at the time of measurement. Individual core sections are moved along the static sensors on a horizontal conveyor belt. The latter consists of an endless tooth belt system, which is able to transport the core sections with almost no slippage, thus ensuring an accurate horizontal positioning of the objects to be measured. Two laser distance meter (WELOTEC, Germany, type OWTB V2) measure in real time the distance to the respective edges of the core section and guarantee for a positioning accuracy and determination of section length of better than 0.1 mm.

The V-shaped layout of the four endless conveyor belts ensures an exact axial alignment. It accurately holds the core section on its position on the belt without being accidently moved, even during severe ship movements. The setup consists of four AM8131 three-phase permanent magnet synchronous motors (Beckhoff. Germany), which are electrically connected to form a cluster of two pairs. Thus, it is possible to position even heavy sediment cores with a practical repeatability of better than 0.2 mm.

The sensor module is currently carrying two probes and is located in the centre of the MSCLS. Two fully assembled modules are available, each with a Bartington MS2C susceptibility loop sensor with different coil diameters of 85 mm and 140 mm, respectively. To change between the modules only takes a few minutes and requires no readjustment of the system to adapt to different core diameters. Only the sensors for electrical conductivity and for temperature have to be exchanged between the modules due to availability.

The actual temperature of the core section to be measured is determined by means of a non-contact infrared thermometer focusing on location of recent electrical conductivity measurement.

Since only a single core section is measured at a time, it is possible to horizontally traverse the section forward and backward along the conveyor belt. Any number of background measurements during a measuring cycle can be conducted in order to determine any eventual sensor drift. Therefore, sediment cores were usually measured shortly after their recovery. Warming of the sections to room temperature, as on previous cruises, is no longer necessary.

Magnetic Volume Susceptibility

Measurements on all cores were made on whole-round sections using a MS2C loop sensor (Bartington Instruments Ltd., UK) with a diameter of 140 mm (S/N 827) for gravity cores. MeBo core sections were measured with a MS2C loop sensor with a diameter of 85 mm (S/N 832). Additional measurements were carried out on half-round sections of the MeBo cores. The control unit was a Bartington MS3 (S/N 456), which allows an almost freely programmable time integration of the measurement signal. The functional principle of the susceptibility meter is an oscillator circuit that produces a weak (approximately 80 A/m RMS) non-saturating alternating magnetic field with a frequency of 565 Hz. A PC communicates with the MS3 via an in-house developed serial protocol (RS232) providing permanent checksum proofing of the data transfer.

At the beginning of the measurement of each core section, the MS3 unit was reset and zeroed. The zero measurement provides the reference values E_0, I_0, $F_{1.0}$ and $F_{2.0}$ while the respective parameters E, I, F_1, F_2 from each sample measurement are used to obtain the uncalibrated magnetic susceptibility:

$$V = (I \times 10^{E+1} - I_0 \times 10^{E0+1}) + (F_1 \times 10^{E-5} - F_{1.0} \times 10^{E0-5}) + (F_2 \times 10^{E-12} - F_{2.0} \times 10^{E0-12}) \quad (5.3)$$

This value is transformed into the calibrated susceptibility κ' [SI] by applying the MS3 calibration constant $k = 1.5121357037 \times 10^{-3}$ and the value V_{air} which is determined after the MS3 was initially zeroed and without sediment within the sensitive volume. V_{air} takes into account the ambient environmental conditions:

$$\kappa' = \frac{V - V_{air}}{k} \quad (5.4)$$

with κ' the calibrated magnetic susceptibility [SI], V the uncalibrated magnetic susceptibility, and V_{air} the measurement "in air". Finally κ' is normalized to the volume by correcting for the ratio between the MS2C loop sensor diameter and the core diameter:

$$\kappa = \frac{1}{3.45 \cdot \left(\frac{d}{D + smm}\right)^3} \cdot \kappa' \tag{5.5}$$

with d the core diameter and D the sensor diameter.

Electrical Resistivity. Porosity and Density

Electrical resistivity is a measure of how strongly a material opposes the flow of electric current and is the reciprocal of electrical conductivity. A low resistivity indicates a material that readily allows the movement of electrical charge. The SI unit of electrical resistivity is the ohm-meter and the SI unit of electrical conductivity is Siemens per meter.

Electrical resistivity was measured by means of a non-contact resistivity (NCR) sensor (Version 02.2016) by Geotek Ltd. (UK). The NCR sensor uses a transmitter coil to induce a high-frequent magnetic field in the sediment, which in turn generates an electrical current in the sediment that is inversely proportional to the resistivity. A receiver coil measures the very small magnetic field regenerated by the electrical current in the sediment. These readings are compared with those from a second identical coil operating in air. This difference technique provides the required accuracy and stability. Electrical resistivities between 0.21 Ohm-m and 15.48 Ohm-m (at 20ºC) can be measured with a spatial resolution along the core of approximately 2 cm.

The analogue output Q-signal (±2500 mV) of the NCR sensor was digitized using a 16-bit, 250 kS/s National Instruments PCIe-6320 analogue-to-digital (AD) converter.

The temperature of the object to be measured, which was used to calculate the specific resistance, was recorded using a non-contact Omega OS151 infrared thermometer. In its simplest construction, an infrared thermometer consists of a lens that focuses the infrared energy on a detector. This energy is then converted into an electrical signal (4 - 20 mA) which has also been digitized with 16 bits. This ensures an accuracy of ±1 % of the measured value, or a repeatability of 0.5 % of the measured value.

For the necessary NCR calibration we daily measured a set of saline solutions at concentrations of 0.35 - 1.75 - 3.5 - 8.75 - 17.5 - 35 g/l. Respective voltage readings minus zero level of the sensor are automatically saved to the control software and applied to voltage data from the core section.

Parameter-Setup

Following parameters were applied for physical properties measurements during M154-2:

General Settings	
Distance between core section and sensors for sensor initialization	40 (50) cm
Number of drift measurements	3 (5)
Sampling interval for all sensors	1 cm
Motor velocity	150 mm/s
Motor acceleration / deceleration	100 mm/s^2
Thickness of end caps	2 mm

Magnetic Susceptibility	
Integration time	3500 ms
Leader distance	14 cm
Electrical Conductivity	
Integration time	3500 ms (16-Bit, 100 S/s)
Leader distance	14 cm
Temperature	
Integration time	1000 ms (16-Bit, 100 S/s)

5.4.3.2 Fall Cone Test

The geotechnical properties of the recovered sediments were determined according to the British Standards Institutions (BS1377, 1975). A Wykeham-Ferrance Fall Cone Penetrometer WF 21600 (Fig. 5.20) was used for a first-order estimate of the undrained shear strength. For the measurement, an 80.51 g fall cone with a 30° dip angle was placed directly on the surface of the split core surface (Wood, 1985). It was then released manually to penetrate the sediment in dependence of the sediment's stiffness and the acting gravity. A manual displacement transducer was used to measure the distance prior and after release of the cone (i.e. penetration after free fall of the cone), with a precision of 0.1 mm. The distances measured were converted into undrained shear strength (s_u; Hansbo, 1957):

$$s_u = \frac{m \cdot g \cdot k}{d_p^2} \tag{5.6}$$

with m the cone mass, g the gravity, d_p the penetration depth, and k a geometry-dependent cone factor. Wood (1985) calculated a cone factor k of 0.85 for a 30° cone from extensive fall-cone and miniature vane tests. Main uncertainties related to the fall cone test include the accuracy of displacement measurements as well as gravitational variability on sea due to the wave-forced ship motion (see chapter 5.3.5.4). Additional uncertainties may arise from core disturbances and moisture loss during core splitting. In general, accuracy of the measurements is best for soft sediments with low stiffness. On shore laboratory tests will include ring shear experiments, as well as dynamic triaxial shear tests on selected core material, which was preserved as whole round (WR) sections. From these additional tests, residual strength and rate-dependent frictional properties can be estimated.

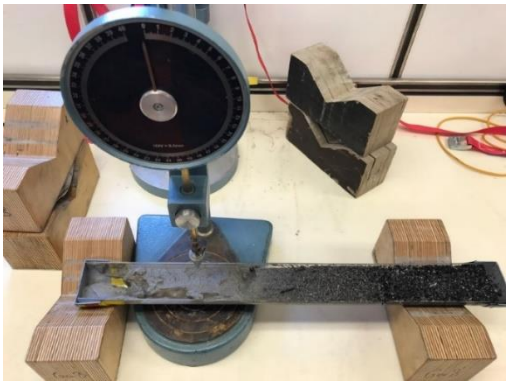

Fig. 5.20: Fall cone penetrometer.

5.4.3.3 Vane Shear Test

In addition to the fall cone test, a standard Wykeham-Ferrance 4WF1730/2 vane shear apparatus (Fig. 5.21) was used for more information about the sediment's shear strength. The vane shear test measures angular deflection of springs that were calibrated for torque. A four-bladed vane of 12.7 mm height h and diameter d was inserted into the undisturbed sediment of the cores and rotated at a constant rate of 10°/min until failure. The torque T required to shear the sediment along the vertical and horizontal edges of the vane is a relatively direct measure of the undrained shear strength s_u and has to be normalized to the vane constant K (Blum, 1997):

$$s_u = \frac{T}{K} \tag{5.7}$$

where the torque T is a function of the measured angular deflection α in dependence of the spring used:

spring #1 $T = 0.0009\alpha - 0.0007$
spring #2 $T = 0.0016\alpha - 2E\text{-}16$
spring #3 $T = 0.00025\alpha + 0.0002$
spring #4 $T = 0.0042\alpha + 0.0014$

The vane constant K is defined as a function of the vane size and geometry:

$$K = \pi \cdot d^2 \frac{h}{2} + \pi \frac{d^2}{6} \tag{5.8}$$

The main uncertainties for vane shear tests include the accuracy of angular deflation readings and possible inhomogeneities within the sediment (e.g. cracks). Further uncertainties may arise from core disturbances and moisture loss during core splitting. In general, accuracy of the measurements is considered superior in comparison to fall cone tests, especially for high undrained shear strengths.

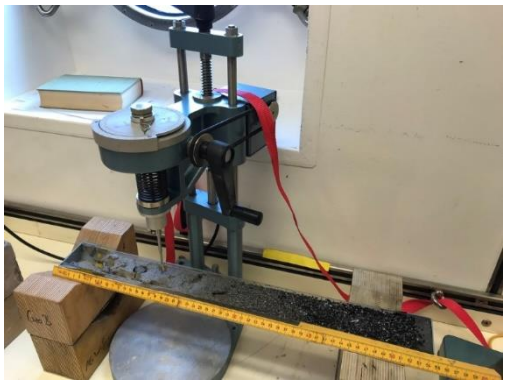

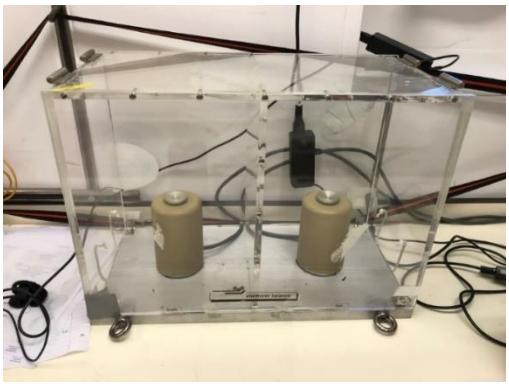

Fig. 5.21: Vane shear apparatus and GEOMAR seagoing balance.

5.4.3.4 Moisture and Density (MAD)

Moisture and Density (MAD) parameters are determined from the wet mass, dry mass and dry volume measurements of ~5 cm^3 samples taken from the working halves of the recovered cores according to ODP and IODP shipboard laboratory practices (Blum, 1997). The MAD parameters include moisture content, bulk and grain density, and porosity.

During the cruise M154-2, shipboard measurements on MAD parameters were restricted to wet and dry mass measurements. It was ensured that only the undisturbed parts of the core were sampled and that drilling fluids in case of MeBo cores were avoided. Core samples of ~5 cm^3 were extruded using syringes and transferred into 10 mL glass beakers of known mass and volume. Subsequently, the combined weight of beaker and wet sample was measured before the sample was dried for at least 24 h in a convection oven at 105 °C. Before determining the combined weight of breaker and dry sample, the sample was transferred into a desiccator for about 1 h to let it cool to room temperature.

Masses were determined to a precision of 0.01 g using the GEOMAR seagoing balance equipped with two electronic balances (Fig. 5.21). To compensate for ship motion, sample weights were averaged over 100 individual measurements at 10 Hz. Additionally, each measured sample weight was accompanied by a weight measurement of a reference mass within a 5 g margin of the actual sample weight (20 g) to account for the remaining error. Shipboard moisture content has been calculated from the measured wet mass and dry mass following Blum (1997) and is expressed as a percentage of the sample's dry weight. The presented data have been corrected for the mass and volume of evaporated seawater assuming a seawater salinity of 35 ppt. This results in a fluid density of 1.024 g/cm³ assuming a salt density of 2.20 g/cm³. All other presented MAD parameters are of preliminary nature only, as they are based on a volume estimate of 5 cm^3 for each sample. Although the error margin is expected to lie within +/-20 %, additional dry measurements are required for accurate results. These will be carried out using a helium-displacement penta-pycnometer upon return of the samples to MARUM, University of Bremen.

5.4.3.5 Preliminary Results

All cores recovered and opened during the cruise M154-2 were analysed for their key physical properties. Compiled data of MSCL magnetic susceptibility, porosity and density measurements, and undrained shear strength, as well as preliminary results for bulk porosity and bulk density with all other shipboard data can be found in the Appendix. The following part will set focus on the preliminary results obtained for site 11.

At site 11, one gravity core and three MeBo cores were recovered on the platform E of Montserrat, just above the head scarp of Deposit 2 (Figs 3.2, 5.11; Watt et al., 2012b). In addition, in-situ borehole data was acquired with the MeBo drilling rig, which included magnetic susceptibility, gamma-ray and p-wave velocity measurements (see chapter 5.2). Figure 5.22 illustrates the magnetic susceptibility, shear strength, porosity and density profiles of gravity core GeoB23711-1 and the three MeBo cores GeoB23711-2, GeoB23711-3 and GeoB23711-4. The sampled slope material from site 11 shows a slightly increasing undrained shear strength with depth in the uppermost 20 m below seafloor to around 80 kPa. The shear strength drops at 24 mbsf to <20 kPa, before it increases continuously again until around 60 mbsf to >125 kPa. The same trend can also be observed in the p-wave velocity profile. Two pronounced peaks in p-wave velocity and magnetic susceptibility at around 24 mbsf can be correlated to gravel layers. These gravel layers could be the base of a disturbed mass transport deposit, probably of Deposit 2. The porosity profiles obtained from the MSCL and MAD measurements correlate well and vary between around 40 % and 70 %, while the density profiles of the MSCL and MAD do not correlate as well. The reason for this difference could be the unknown volume of the core samples, i.e.

falsifying the obtained density values. Nevertheless, the density behaves inversely proportional.to the porosity.

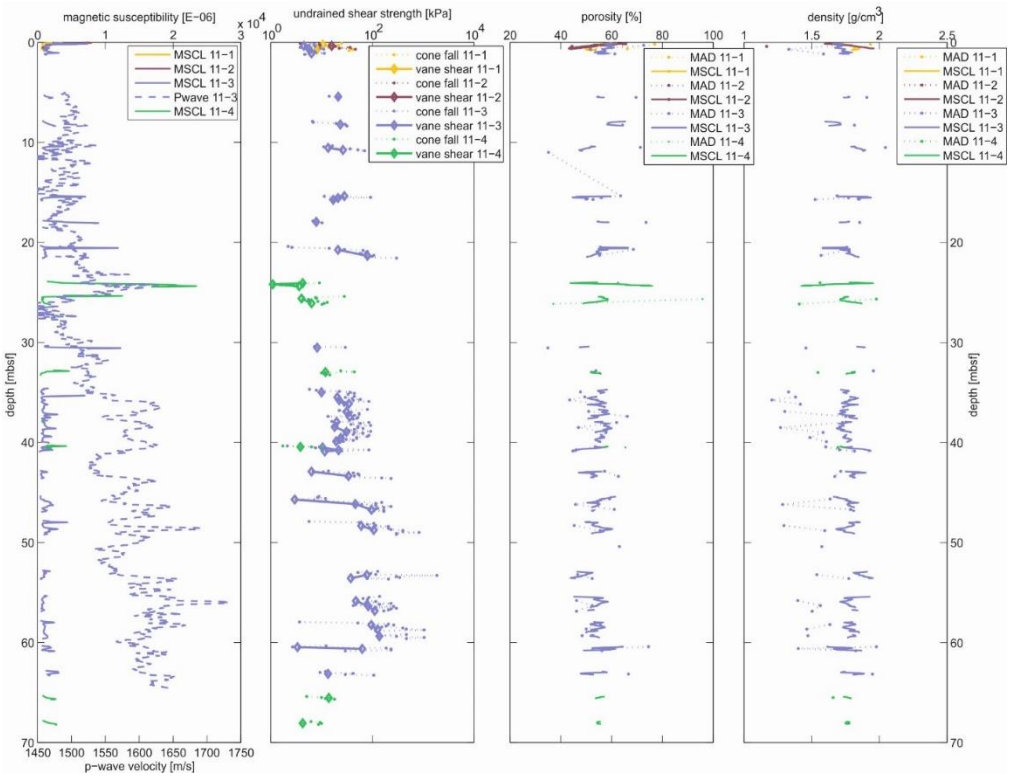

Fig. 5.22: Compilation of in-situ measured p-wave velocity, MSCL measurements (magnetic susceptibility, porosity and density), undrained shear strength (fall cone and vane shear data) and MAD results (porosity and density) at site 11 on the platform E of Montserrat. Gaps in the datasets indicate cores sections without core recovery.

5.5 Heat Flow Measurement

(M. Hornbach)

We calculated heat flow at a total of ten sites during the RV Meteor cruise 154-2 (sites 5-2, 11-3, 15-1 to 19-1, 25-1, 30-1, 31-1). Five of these heat flow sites used an experimental, portable and detachable violin-bow outrigger system developed at Southern Methodist University. Five additional heat flow estimates were made using raw temperature data acquired from logging with MeBo.

5.5.1 Theoretical Background

For the simplest case of 1D diffusive (i.e. non-advective) heat flow in the earth with no source terms and constant thermal conductivity, we calculate heat flow as follows:

$$H = k \frac{dT}{dz} \tag{5.9}$$

where H is heat flow [W/m^2], k is thermal conductivity [W/mK], T is temperature [K], and z is depth below the seafloor [m]. For this study, we measured heat flow by measuring the thermal gradient with depth using both MeBo temperature measurements, and heat flow measurements from the **PoGo** (**P**ortable **G**eothermal gradient) probe detachable violin-bow outrigger system, and

an average thermal conductivity of 1 W/mK. consistent with previous measurements in hemipelagic sediments around Montserrat (Manga et al., 2012). It is important to recognize that this is only a very rough, first-order method for assessing heat flow, as it ignores or simplifies several influencing factors including, but not limited to (1) variable conductivity, (2) influences of ocean bottom temperature variations, (3) advective heat transport, (4) 3D topographic effects, (5) sedimentation and erosion, and (6) additional heat source terms. Final results will need to address all of these issues properly.

5.5.2 System Setup and Theory

We estimated heat flow using two different tools during Meteor cruise 154-2. The first method attached a ~1.5 m long PoGo probe developed at Southern Methodist University to the gravity corer to measure shallow sub-seafloor heat flow. The second method used data acquired from a thermistor installed on the MeBo sonic logging tool.

5.5.2.1 PoGo Probe Heat Flow Method

The PoGo probes used for this study consist of eight thermistors spaced ~0.2 m apart inside a high-conductive resin-filled stainless-steel rod. In all cases, the bottom thermistor was mounted 41 cm above the bottom of the corer, so that the probe head was approximately ~1.9 m above the base of the corer and 1.1 m below the top of the 3 m corer. The probe head where the probe is powered and data is stored/transmitted also contains a thermistor, internal pressure and humidity gauge, and three component accelerometer to assess orientation of the probe. We deployed the PoGo probe on the corer six times, and had five successful deployments where at least five or more thermistors penetrated sediment and we obtained interpretable results. For all five successful insertions, the probe was orientated within ~2 degrees of vertical, indicating no need for dip angle corrections for calculating thermal gradient.

To calculate steady-state temperature at each thermistor, we randomly vary both probe insertion time-shift between 2 – 4 minutes and the number of post-time-shift temperature measurements used to find a best fit using the Villinger and Davis (1987) approach. We calculate the steady state temperature using this approach until the standard deviation for average temperature falls below 0.01ºC. With steady state temperature and uncertainty for each sub-seafloor thermistor constrained, we then apply a least-squares fit to the temperature-depth profile to calculate the thermal gradient at each site. We estimate uncertainty in the thermal gradient by applying a Monti Carlo approach to estimate thermal gradient. With the initial temperature versus depth plotted, we looked for and removed any temperature outliers associated with either anomalously sandy zones in the core or very shallow penetration depths (<1 m) where bottom water temperature variability can introduce outliers. In most cases, no values were removed as the probe penetrated fully into the seafloor. Once the initial thermal gradient is constrained, we should still correct for 3D topographic effects using multibeam bathymetric data and sedimentation rates derived from the core. We calculate an initial heat flow at each site by multiplying thermal gradient by average regional sediment thermal conductivity of 1 W/mK (Manga et al., 2012).

5.5.2.2 Heat Flow Estimated from MeBo Sonic Log Thermistor

During each MeBo sonic log deployment, temperature was measured by a thermistor attached to the sonic logging tool. Although drilling, coring, and fluid circulation will influence downhole temperatures, the temperature measurements on the sonic tool may be used to obtain low-resolution temperature versus depth profiles in MeBo drilling boreholes (pers.comm. shipboard with T. Freundenthal). We have yet to fully process this data. Instead, we simply plot temperature versus depth and apply a very simple linear fit to the profiles to estimate thermal gradient at each of the sites. A more detailed analysis requires (1) detailed study of the drilling and logging history and how it likely impacts regional temperatures, (2) analysis of temperature decay during each drill string pipe removal and racking where see evidence of temperature warming with time, and (3) detailed comparison of temperatures to regional stratigraphy.

5.5.3 Preliminary Results

We provide initial heat flow estimates for all 10 sites (Fig. 5.23). Results from all of these sites compare favourably with previous regional heat flow measurements made both near Montserrat and across the Lesser Antilles Volcanic Arc (e.g. Clark et al., 1978; Manga et al., 2012). We observe the highest heat flow values (~440 mW/m^2) across a NE-SW trending normal fault system bounding the edge of the graben southeast of Montserrat. These values are the highest yet recorded in this region. We speculate that these high heat flow values are associated with upward advection along the faults. We remind the reader that these values are of first order and may have high uncertainty as they are uncorrected for 3D topographic and sedimentation effects, borehole cooling during drilling at MeBo sites, and variations in sediment thermal conductivity.

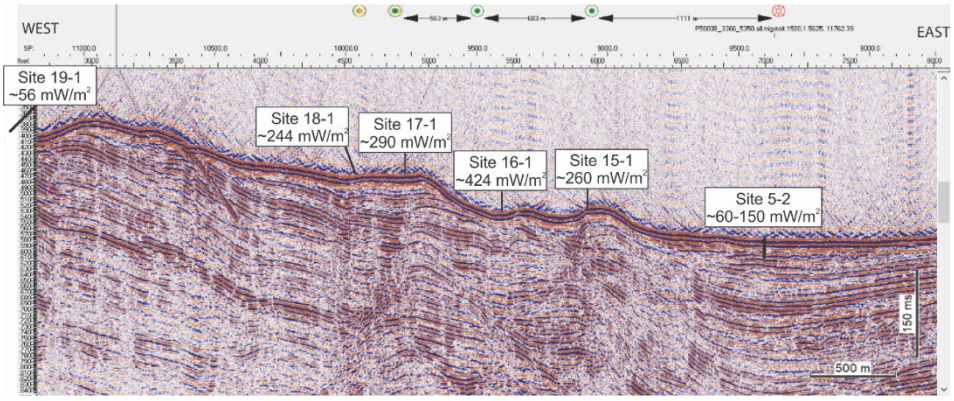

Fig. 5.23: Preliminary heat flow results for coring/PoGo probe sites 23715-1 to 23719-1 and MeBo site 23705-2. Results are plotted on seismic line P5008_12450_14090.all.migstolt.1500.1.5625, located ~1 km south of the heat flow transect. Site 19-1 is located just east of the seismic line. PARASOUND images (not shown here) indicate that site 16-1 was located directly on a fault outcropping at the seafloor

6 Ship's Meteorological Station

(M. Stelzner)

Research vessel (RV) METEOR left the port of Pointe-á-Pitre/Guadeloupe at 12 o'clock on the 29th of April 2019. At that time, the research area was on the southeast edge of a stable North Atlantic high south to southeast of Montserrat. The initially weak east to northeast trade wind blew with increasingly 5 to 6 Bft. The significant wave height of 2 m was composed of a 0.5 m wind sea and a 1.5 to 2 m swell from the east. There were rarely rain showers on site. At the start of May, the showers almost disappeared and there were no changes of wind and significant wave height. From the 8th of May 2019, a deepening depression southeast of Newfoundland disturbed the weather-determining North Atlantic high. Thereupon decreased the east trade wind down to 4 Bft at the research area. The swell came still from easterly directions, but the significant wave height went down to 1.5 m. With the low travelling to Europe a new high, coming from west, spread over the North Atlantic. Meanwhile there was a steady east trade wind with temporarily increasing wind up to 6 Bft or decreasing winds down to 3 Bft. The significant wave height was still approximately 1.5 m.

Towards the end of the expedition M154-2 a higher shower frequency was noticeable. However, the research work on board was not disturbed because the focus area of the activity of these showers was east of Guadeloupe and Antigua/Barbuda. This journey ended one day earlier than scheduled. on the 22 May at 12 o'clock at the harbour of Pointe-á-Pitre/Guadeloupe.

7 Station List M154-2

7.1 Parasound Profile List

Parasound FFN End	Date	Time Start	Time End	Latitude Start	Longitude Start	Latitude End	Longitude End	EM122	Parasound
		[UTC]	[UTC]	[N]	[W]	[N]	[W]		
P1000	01.05.2019	00:50	02:54	16°28.937	62°00.434	16°36.072	61°51.590	x	x
P1001	01.05.2019	02:54	03:58	16°36.072	61°51.590	16°33.199	62°02.876	x	x
P1002	01.05.2019	03:58	06:20	16°33.199	62°02.876	16°33.160	62°16.383	x	x
P1003	01.05.2019	06:20	06:41	16°33.160	62°16.383	16°32.390	62°15.970	x	x
P1004	01.05.2019	06:41	09:12	16°32.390	62°15.970	16°32.370	62°01.814	x	x
P1005	01.05.2019	09:12	09:26	16°32.370	62°01.814	16°31.573	62°01.940	x	x
P1006	01.05.2019	09:26	13:29	16°31.573	62°01.940	16°30.841	61°57.990	x	x
P2001	02.05.2019	01:30	04:18	16°31.572	62°01.556	16°31.628	62°15.625	x	x
P2002	02.05.2019	04:18	04:42	16°31.628	62°15.625	16°30.810	62°16.039	x	x
P2003	02.05.2019	04:42	06:22	16°30.810	62°16.039	16°30.754	62°4.400	x	x
P2004	02.05.2019	06:22	06:49	16°30.754	62°4.400	16°30.742	62°1.731	x	x
P2005	02.05.2019	06:49	09:31	16°30.742	62°1.731	16°30.000	62°16.050	x	x
P2006	02.05.2019	09:31	09:40	16°30.000	62°16.050	16°29.455	62°16.355	x	x
P2007	02.05.2019	09:40	11:00	16°29.455	62°16.355	16°29.162	62°08.956	x	x
P2008	02.05.2019	11:00	11:40	16°29.162	62°08.956	16°33.706	62°11.925	x	x
P2009	03.05.2019	21:35	22:48	16°31.009	61°57.529	16°29.209	62°10.104	x	x
P2010	03.05.2019	22:48	00:49	16°29.209	62°10.104	16°29.101	61°58.703	x	x
P2011	04.05.2019	00:49	04:05	16°29.101	61°58.703	16°28.398	62°15.960	x	x
P2012	04.05.2019	04:05	04:21	16°28.398	62°15.960	16°27.603	62°15.866	x	x
P2013	04.05.2019	04:21	07:27	16°27.603	62°15.866	16°27.474	61° 58.249	x	x
P2014	04.05.2019	07:27	07:41	16°27.474	61° 58.249	16°26.672	61° 58.390	x	x
P2015	04.05.2019	07:41	08:18	16°26.672	61° 58.390	16°33.516	62°2.135	x	x
P2016	04.05.2019	08:18	09:49	16°33.516	62°2.135	16°43.854	62°2.23	x	x
P3000	05.05.2019	01:08	01:53	16°45.837	62°2.378	16°39.702	62°08.995	x	x
P3001	05.05.2019	01:53	03:15	16°39.702	62°08.995	16°32.222	62°09.072	x	x
P3002	05.05.2019	03:15	03:25	16°32.222	62°09.072	16°32.113	62°09.829	x	x
P3003	05.05.2019	03:25	04:43	16°32.113	62°09.829	16°39.356	62°09.964	x	x
P3004	05.05.2019	04:43	04:57	16°39.356	62°09.964	16°39.232	62°10.850	x	x
P3005	05.05.2019	04:57	06:34	16°39.232	62°10.850	16°30.084	62°11.160	x	x
P3006	05.05.2019	06:34	08:33	16°30.084	62°11.160	16°39.948	62°13.594	x	x
P3007	05.05.2019	08:33	08:43	16°39.948	62°13.594	16°40.385	62°14.313	x	x
P3008	05.05.2019	08:43	10:24	16°40.385	62°14.313	16°31.411	62°14.192	x	x
P3009	05.05.2019	10:24	10:54	16°31.411	62°14.192	16°31.224	62°16.993	x	x
P3010	05.05.2019	10:54	12:30	16°31.224	62°16.993	16°39.953	62°16.644	x	x
P3011	05.05.2019	12:30	14:05	16°39.953	62°16.644	16°46.542	62°02.697	x	x
P3012	07.05.2019	18:12	20:10	16°39.532	62°13.526	16°47.269	62°16.735	x	x
P3013	07.05.2019	20:10	21:14	16°47.269	62°16.735	16°42.091	62°17.686	x	x
P3014	07.05.2019	21:14	22:24	16°42.091	62°17.686	16°47.373	62°17.894	x	x
P3015	07.05.2019	22:24	23:40	16°47.373	62°17.894	16°43.032	62°18.691	x	x
P3016	07.05.2019	23:40	00:36	16°43.032	62°18.691	16°47.777	62°18.795	x	x
P3017	08.05.2019	00:36	01:45	16°47.777	62°18.795	16°42.084	62°19.848	x	x

P3018	08.05.2019	01:45	02:55	16°42.084	62°19.848	16°47.783	62°19.946	x	x
P3019	08.05.2019	02:55	04:25	16°47.783	62°19.946	16°42.194	62°21.217	x	x
P3020	08.05.2019	04:25	05:34	16°42.194	62°21.217	16°48.548	62°20.554	x	x
P3021	08.05.2019	05:34	06:29	16°48.548	62°20.554	16°48.207	62°15.781	x	x
P3022	08.05.2019	06:29	07:09	16°48.207	62°15.781	16°46.676	62°14.825	x	x
P3023	08.05.2019	07:09	07:46	16°46.676	62°14.825	16°50.333	62°13.898	x	x
P3024	08.05.2019	07:46	08:10	16°50.333	62°13.898	16°48.638	62°14.886	x	x
P3025	08.05.2019	08:10	08:35	16°48.638	62°14.886	16°50.717	62°14.850	x	x
P3026	08.05.2019	08:35	09:46	16°50.717	62°14.850	16°46.994	62°2.370	x	x
P4000	11.05.2019	01:41	02:29	16°47°435	62°01.905	16°52°621	62°09.176	x	x
P4001	11.05.2019	02:29	03:00	16°52°621	62°09.176	16°51°407	62°07.385	x	x
P4002	11.05.2019	03:00	03:23	16°51°407	62°07.385	16°52°081	62°09.571	x	x
P4003	11.05.2019	03:23	04:03	16°52°081	62°09.571	16°52°775	62°13.290	x	x
P4004	11.05.2019	04:03	04:11	16°52°775	62°13.290	16°52.538	62°14.027	x	x
P4005	11.05.2019	04:11	05:26	16°52.538	62°14.027	16°50.645	62°07.717	x	x
P4006	11.05.2019	05:26	05:40	16°50.645	62°07.717	16°49.806	62°08.400	x	x
P4007	11.05.2019	05:40	06:58	16°49.806	62°08.400	16°51.483	62°15.877	x	x
P4008	11.05.2019	06:58	08:07	16°51.483	62°15.877	16°41.617	62°22.167	x	x
P4009	11.05.2019	08:07	10:02	16°41.617	62°22.167	16°36.155	62°1.367	x	x
P4010	12.05.2019	16:52	17:32	16°35.926	62°1.467	16°34.883	62°7.849	x	x
P4011	12.05.2019	17:32	19:06	16°34.883	62°7.849	16°30.189	62°2.035	x	x
P4012	12.05.2019	19:06	20:26	16°30.189	62°2.035	16°34.867	62°8.177	x	x
P4013	12.05.2019	20:26	20:56	16°34.867	62°8.177	16°36.051	62°2.117	x	x
P4014	13.05.2019	13:38	13:58	16°32.325	62°00.898	16°29.443	62°01.736	x	x
P4015	13.05.2019	13:58	15:07	16°29.443	62°01.736	16°33.277	62°07.200	x	x
P4016	13.05.2019	15:07	20:15	16°33.277	62°07.200	16°32.380	62°10.891	x	x
P4017	13.05.2019	20:15	21:11	16°32.380	62°10.891	16°36.629	62°02.223	x	x
P4018	16.05.2019	02:08	03:43	16°29.223	62°02.178	16°32.719	62°08.720	x	x
P4019	16.05.2019	03:43	04:28	16°32.719	62°08.720	16°34.551	62°06.246	x	x
P4020	16.05.2019	04:28	05:10	16°34.551	62°06.246	16°31.356	62°07.909	x	x
P4021	16.05.2019	05:10	05:59	16°31.356	62°07.909	16°34.073	62°05.449	x	x
P4022	16.05.2019	05:59	06:45	16°34.073	62°05.449	16°30.888	62°07.117	x	x
P4023	16.05.2019	06:45	07:32	16°30.888	62°07.117	16°33.573	62°04750	x	x
P4024	16.05.2019	07:32	08:22	16°33.573	62°04750	16°30.880	62°6.034	x	x
P4025	16.05.2019	08:22	09:06	16°30.880	62°6.034	16°32.970	62°4.102	x	x
P4026	16.05.2019	09:06	09:49	16°32.970	62°4.102	16°30.000	62°5.495	x	x
P4027	16.05.2019	09:49	10:39	16°30.000	62°5.495	16°32.509	62°3.364	x	x
P4028	16.05.2019	10:39	11:00	16°32.509	62°3.364	16°30.757	62°4.473	x	x
P4029	16.05.2019	11:00	11:34	16°30.757	62°4.473	16°33.570	62°2.059	x	x
P4030	17.05.2019	02:32	03:20	16°36.396	61°58.826	16°26.668	62°01.474	x	x
P4031	17.05.2019	03:20	06:07	16°26.668	62°01.474	16°26.576	62°17.711	x	x
P4032	17.05.2019	06:07	08:17	16°26.576	62°17.711	16°38.710	62°18.228	x	x
P4033	17.05.2019	08:17	09:53	16°38.710	62°18.228	16°31.584	62°2.964	x	x
P4034	19.05.2019	14:39	17:31	16°34.046	62°09.466	16°47.052	62°02.795	x	x
P4035	20.05.2019	14:28	16:22	16°46.270	62°01.488	16°37.083	61°53.950	x	x
P4036	20.05.2019	16:22	17:33	16°37.083	61°53.950	16°36.733	62°01.639	x	x

7.2 Overall Station List

Station No.		Date	Time	Gear	Latitude	Longitude	Water Depth	Remarks
METEOR	GeoB		[UTC]		[N]	[W]	[m]	
M154/2_1-1	23701-1	30.04.2019	11:59	GC	16°30.545'	61°57.839'	1190	in the water
M154/2_1-1	23701-1	30.04.2019	12:40	GC	16°30.545'	61°57.839'	1190	max depth/on ground
M154/2_1-1	23701-1	30.04.2019	13:05	GC	16°30.547'	61°57.837'	1190	on deck
M154/2_2-1	23702-1	30.04.2019	13:36	GC	16°30.893'	61°58.081'	1180	in the water
M154/2_2-1	23702-1	30.04.2019	14:00	GC	16°30.887'	61°58.064'	1180	max depth/on ground
M154/2_2-1	23702-1	30.04.2019	14:26	GC	16°30.888'	61°58.064'	1180	on deck
M154/2_3-1	23703-1	30.04.2019	14:54	GC	16°31.469'	61°57.348'	1176	in the water
M154/2_3-1	23703-1	30.04.2019	15:15	GC	16°31.469'	61°57.325'	1176	max depth/on ground
M154/2_3-1	23703-1	30.04.2019	15:42	GC	16°31.470'	61°57.324'	1176	on deck
M154/2_4-1	23704-1	30.04.2019	16:04	GC	16°32.062'	61°56.632'	1160	in the water
M154/2_4-1	23704-1	30.04.2019	16:29	GC	16°32.066'	61°56.618'	1161	max depth/on ground
M154/2_4-1	23704-1	30.04.2019	16:55	GC	16°32.066'	61°56.617'	1160	on deck
M154/2_5-1	23705-1	30.04.2019	17:35	GC	16°33.241'	61°55.165'	1112	in the water
M154/2_5-1	23705-1	30.04.2019	17:54	GC	16°33.246'	61°55.143'	1112	max depth/on ground
M154/2_5-1	23705-1	30.04.2019	18:18	GC	16°33.246'	61°55.143'	1111	on deck
M154/2_2-2	23702-2	30.04.2019	19:56	SVP	16°30.883'	61°58.070'	1182	in the water
M154/2_2-2	23702-2	30.04.2019	19:58	SVP	16°30.885'	61°58.070'	1181	max depth/on ground
M154/2_2-2	23702-2	30.04.2019	20:24	SVP	16°30.895'	61°58.049'	1180	on deck
M154/2_2-3	23702-3	30.04.2019	20:44	MEBO	16°30.899'	61°58.037'	1180	in the water
M154/2_2-3	23702-3	30.04.2019	23:02	MEBO	16°30.892'	61°58.033'	1181	max depth/on ground
M154/2_2-3	23702-3	30.04.2019	23:32	MEBO	16°30.893'	61°58.031'	1180	information
M154/2_2-3	23702-3	01.05.2019	23:33	MEBO	16°30.880'	61°58.029'	1183	information
M154/2_2-3	23702-3	01.05.2019	23:42	MEBO	16°30.879'	61°58.034'	1181	hoisting
M154/2_2-3	23702-3	02.05.2019	00:55	MEBO	16°30.936'	61°58.039'	1178	on deck
M154/2_6-1	23706-1	02.05.2019	12:23	GC	16°33.721'	62°11.904'	914	in the water
M154/2_6-1	23706-1	02.05.2019	12:43	GC	16°33.720'	62°11.897'	915	max depth/on ground
M154/2_6-1	23706-1	02.05.2019	13:10	GC	16°33.721'	62°11.898'	915	on deck
M154/2_7-1	23707-1	02.05.2019	13:52	GC	16°32.384'	62°11.649'	968	in the water
M154/2_7-1	23707-1	02.05.2019	14:12	GC	16°32.384'	62°11.627'	968	max depth/on ground
M154/2_7-1	23707-1	02.05.2019	14:37	GC	16°32.385'	62°11.627'	968	on deck
M154/2_2-4	23702-4	02.05.2019	16:30	GC	16°30.901'	61°58.070'	1179	in the water

M154/2_2-4	23702-4	02.05.2019	16:54	GC	16°30.890'	61°58.053'	1183	max depth/on ground
M154/2_2-4	23702-4	02.05.2019	17:20	GC	16°30.890'	61°58.053'	1184	on deck
M154/2_2-5	23702-5	02.05.2019	19:39	MEBO	16°30.886'	61°58.064'	1184	in the water
M154/2_2-5	23702-5	02.05.2019	21:42	MEBO	16°30.891'	61°58.038'	1182	max depth/on ground
M154/2_2-5	23702-5	02.05.2019	22:52	MEBO	16°30.892'	61°58.032'	1183	information
M154/2_2-5	23702-5	03.05.2019	19:35	MEBO	16°30.891'	61°58.032'	1185	information
M154/2_2-5	23702-5	03.05.2019	19:41	MEBO	16°30.888'	61°58.037'	1182	hoisting
M154/2_2-5	23702-5	03.05.2019	21:00	MEBO	16°30.892'	61°58.036'	1182	on deck
M154/2_8-1	23708-1	04.05.2019	10:02	GC	16°43.837'	62°02.236'	961	in the water
M154/2_8-1	23708-1	04.05.2019	10:21	GC	16°43.845'	62°02.236'	959	max depth/on ground
M154/2_8-1	23708-1	04.05.2019	10:43	GC	16°43.844'	62°02.236'	961	on deck
M154/2_8-1	23708-1	04.05.2019	10:46	GC	16°43.844'	62°02.236'	960	in the water
M154/2_8-1	23708-1	04.05.2019	11:04	GC	16°43.845'	62°02.237'	959	max depth/on ground
M154/2_8-1	23708-1	04.05.2019	11:27	GC	16°43.845'	62°02.235'	960	on deck
M154/2_9-1	23709-1	04.05.2019	11:46	GC	16°44.032'	62°02.233'	980	in the water
M154/2_9-1	23709-1	04.05.2019	12:04	GC	16°44.030'	62°02.231'	982	max depth/on ground
M154/2_9-1	23709-1	04.05.2019	12:25	GC	16°44.029'	62°02.231'	980	on deck
M154/2_10-1	23710-1	04.05.2019	12:39	GC	16°44.153'	62°02.227'	944	in the water
M154/2_10-1	23710-1	04.05.2019	13:00	GC	16°44.152'	62°02.213'	946	max depth/on ground
M154/2_10-1	23710-1	04.05.2019	13:22	GC	16°44.151'	62°02.214'	945	on deck
M154/2_11-1	23711-1	04.05.2019	13:54	GC	16°46.946'	62°02.223'	856	in the water
M154/2_11-1	23711-1	04.05.2019	14:15	GC	16°46.950'	62°02.216'	854	max depth/on ground
M154/2_11-1	23711-1	04.05.2019	14:36	GC	16°46.952'	62°02.215'	855	on deck
M154/2_11-2	23711-2	04.05.2019	15:08	MEBO	16°46.950'	62°02.217'	855	in the water
M154/2_11-2	23711-2	04.05.2019	16:53	MEBO	16°46.948'	62°02.194'	856	max depth/on ground
M154/2_11-2	23711-2	04.05.2019	17:44	MEBO	16°46.954'	62°02.189'	855	information
M154/2_11-2	23711-2	04.05.2019	23:01	MEBO	16°46.946'	62°02.195'	856	information
M154/2_11-2	23711-2	04.05.2019	23:02	MEBO	16°46.945'	62°02.195'	855	hoisting
M154/2_11-2	23711-2	04.05.2019	23:53	MEBO	16°46.954'	62°02.194'	855	on deck
M154/2_11-3	23711-3	05.05.2019	14:29	MEBO	16°46.943'	62°02.202'	856	in the water
M154/2_11-3	23711-3	05.05.2019	16:00	MEBO	16°46.945'	62°02.194'	855	max depth/on ground
M154/2_11-3	23711-3	05.05.2019	16:47	MEBO	16°46.945'	62°02.187'	854	information
M154/2_11-3	23711-3	07.05.2019	10:40	MEBO	16°46.948'	62°02.187'	856	information
M154/2_11-3	23711-3	07.05.2019	10:48	MEBO	16°46.949'	62°02.192'	855	hoisting
M154/2_11-3	23711-3	07.05.2019	11:58	MEBO	16°46.959'	62°02.191'	856	on deck

M154/2_12-1	23712-1	07.05.2019	14:01	BC	16°39.767'	62°13.329'	616	in the water
M154/2_12-1	23712-1	07.05.2019	14:20	BC	16°39.767'	62°13.317'	615	max depth/on ground
M154/2_12-1	23712-1	07.05.2019	14:36	BC	16°39.766'	62°13.317'	617	on deck
M154/2_12-2	23712-2	07.05.2019	16:16	GRAB	16°39.768'	62°13.311'	613	in the water
M154/2_12-2	23712-2	07.05.2019	16:31	GRAB	16°39.768'	62°13.311'	613	max depth/on ground
M154/2_12-2	23712-2	07.05.2019	16:52	GRAB	16°39.768'	62°13.311'	614	on deck
M154/2_13-1	23713-1	07.05.2019	17:15	GRAB	16°39.825'	62°13.405'	609	in the water
M154/2_13-1	23713-1	07.05.2019	17:30	GRAB	16°39.824'	62°13.407'	612	max depth/on ground
M154/2_13-1	23713-1	07.05.2019	17:51	GRAB	16°39.825'	62°13.407'	667	on deck
M154/2_11-4	23711-4	08.05.2019	13:16	MEBO	16°46.948'	62°02.199'	855	in the water
M154/2_11-4	23711-4	08.05.2019	15:05	MEBO	16°46.954'	62°02.200'	855	max depth/on ground
M154/2_11-4	23711-4	08.05.2019	16:07	MEBO	16°46.951'	62°02.194'	855	information
M154/2_11-4	23711-4	10.05.2019	23:38	MEBO	16°46.957'	62°02.195'	855	information
M154/2_11-4	23711-4	10.05.2019	23:41	MEBO	16°46.956'	62°02.199'	856	hoisting
M154/2_11-4	23711-4	11.05.2019	00:38	MEBO	16°46.981'	62°02.210'	855	on deck
M154/2_14-1	23714-1	11.05.2019	10:10	GC	16°36.190'	62°01.349'	1139	in the water
M154/2_14-1	23714-1	11.05.2019	10:38	GC	16°36.194'	62°01.325'	1140	max depth/on ground
M154/2_14-1	23714-1	11.05.2019	11:02	GC	16°36.195'	62°01.324'	1139	on deck
M154/2_15-1	23715-1	11.05.2019	11:55	GC	16°30.525'	61°58.543'	1166	in the water
M154/2_15-1	23715-1	11.05.2019	12:27	GC	16°30.524'	61°58.534'	1166	max depth/on ground
M154/2_15-1	23715-1	11.05.2019	12:58	GC	16°30.525'	61°58.534'	1167	on deck
M154/2_16-1	23716-1	11.05.2019	13:35	GC	16°30.299'	61°58.836'	1140	in the water
M154/2_16-1	23716-1	11.05.2019	13:59	GC	16°30.297'	61°58.826'	1139	max depth/on ground
M154/2_16-1	23716-1	11.05.2019	14:32	GC	16°30.299'	61°58.826'	1139	on deck
M154/2_17-1	23717-1	11.05.2019	15:02	GC	16°30.110'	61°59.036'	1104	in the water
M154/2_17-1	23717-1	11.05.2019	15:25	GC	16°30.107'	61°59.028'	1106	max depth/on ground
M154/2_17-1	23717-1	11.05.2019	16:00	GC	16°30.109'	61°59.028'	1103	on deck
M154/2_18-1	23718-1	11.05.2019	16:31	GC	16°30.031'	61°59.137'	1101	in the water
M154/2_18-1	23718-1	11.05.2019	16:57	GC	16°30.033'	61°59.134'	1102	max depth/on ground
M154/2_18-1	23718-1	11.05.2019	17:26	GC	16°30.032'	61°59.133'	1101	on deck
M154/2_19-1	23719-1	11.05.2019	18:05	GC	16°28.322'	62°01.126'	967	in the water
M154/2_19-1	23719-1	11.05.2019	18:27	GC	16°28.322'	62°01.092'	967	max depth/on ground
M154/2_19-1	23719-1	11.05.2019	18:55	GC	16°28.323'	62°01.092'	968	on deck
M154/2_20-1	23720-1	11.05.2019	19:28	GC	16°28.331'	62°02.125'	929	in the water

M154/2_20-1	23720-1	11.05.2019	19:50	GC	16°28.330'	62°02.111'	929	max depth/on ground
M154/2_20-1	23720-1	11.05.2019	20:17	GC	16°28.329'	62°02.112'	929	on deck
M154/2_14-2	23714-2	11.05.2019	21:21	MEBO	16°36.190'	62°01.300'	1141	in the water
M154/2_14-2	23714-2	11.05.2019	23:12	MEBO	16°36.188'	62°01.297'	1139	max depth/on ground
M154/2_14-2	23714-2	11.05.2019	23:58	MEBO	16°36.178'	62°01.292'	1141	information
M154/2_14-2	23714-2	12.05.2019	05:36	MEBO	16°36.170'	62°01.299'	1139	information
M154/2_14-3	23714-3	12.05.2019	06:48	MEBO	16°36.173'	62°01.297'	1140	max depth/on ground
M154/2_14-3	23714-3	12.05.2019	07:08	MEBO	16°36.171'	62°01.292'	1140	information
M154/2_14-3	23714-3	12.05.2019	14:05	MEBO	16°36.173'	62°01.294'	1140	hoisting
M154/2_14-3	23714-3	12.05.2019	15:57	MEBO	16°36.224'	62°01.291'	1139	on deck
M154/2_14-4	23714-4	12.05.2019	21:13	MEBO	16°36.190'	62°01.318'	1139	in the water
M154/2_14-4	23714-4	12.05.2019	22:50	MEBO	16°36.194'	62°01.300'	1142	max depth/on ground
M154/2_14-4	23714-4	12.05.2019	23:21	MEBO	16°36.198'	62°01.296'	1139	information
M154/2_14-4	23714-4	13.05.2019	11:23	MEBO	16°36.191'	62°01.294'	1139	information
M154/2_14-4	23714-4	13.05.2019	11:28	MEBO	16°36.188'	62°01.300'	1139	hoisting
M154/2_14-4	23714-4	13.05.2019	12:47	MEBO	16°36.146'	62°01.310'	1140	on deck
M154/2_21-1	23721-1	13.05.2019	15:34	GC	16°33.730'	62°07.501'	928	in the water
M154/2_21-1	23721-1	13.05.2019	15:51	GC	16°33.732'	62°07.494'	928	max depth/on ground
M154/2_21-1	23721-1	13.05.2019	16:19	GC	16°33.733'	62°07.495'	928	on deck
M154/2_22-1	23722-1	13.05.2019	16:53	GC	16°32.400'	62°09.364'	969	in the water
M154/2_22-1	23722-1	13.05.2019	17:12	GC	16°32.378'	62°09.347'	969	max depth/on ground
M154/2_22-1	23722-1	13.05.2019	17:35	GC	16°32.379'	62°09.346'	970	on deck
M154/2_23-1	23723-1	13.05.2019	18:05	GC	16°33.719'	62°09.895'	929	in the water
M154/2_23-1	23723-1	13.05.2019	18:26	GC	16°33.716'	62°09.879'	929	max depth/on ground
M154/2_23-1	23723-1	13.05.2019	18:48	GC	16°33.717'	62°09.880'	929	on deck
M154/2_24-1	23724-1	13.05.2019	19:26	GC	16°32.375'	62°10.899'	971	in the water
M154/2_24-1	23724-1	13.05.2019	19:47	GC	16°32.381'	62°10.891'	971	max depth/on ground
M154/2_24-1	23724-1	13.05.2019	20:15	GC	16°32.380'	62°10.891'	971	on deck
M154/2_25-1	23725-1	13.05.2019	21:28	MEBO	16°36.763'	62°02.077'	1134	in the water
M154/2_25-1	23725-1	13.05.2019	23:04	MEBO	16°36.729'	62°01.997'	1133	max depth/on ground
M154/2_25-1	23725-1	13.05.2019	23:40	MEBO	16°36.732'	62°01.991'	1133	information
M154/2_25-1	23725-1	15.05.2019	17:19	MEBO	16°36.755'	62°01.998'	1132	information
M154/2_25-1	23725-1	15.05.2019	17:31	MEBO	16°36.748'	62°02.001'	1134	hoisting
M154/2_25-1	23725-1	15.05.2019	18:46	MEBO	16°36.762'	62°02.001'	1132	on deck
M154/2_26-1	23726-1	15.05.2019	20:15	BC	16°31.582'	62°02.963'	855	in the water

M154/2_26-1	23726-1	15.05.2019	21:02	BC	16°31.590'	62°02.931'	834	max depth/on ground
M154/2_26-1	23726-1	15.05.2019	21:47	BC	16°31.589'	62°02.934'	832	on deck
M154/2_26-2	23726-2	15.05.2019	22:00	BC	16°31.589'	62°02.934'	832	in the water
M154/2_26-2	23726-2	15.05.2019	22:31	BC	16°31.589'	62°02.935'	829	max depth/on ground
M154/2_26-2	23726-2	15.05.2019	22:40	BC	16°31.589'	62°02.934'	830	hoisting
M154/2_27-1	23727-1	15.05.2019	23:11	BC	16°31.588'	62°02.840'	914	lowering
M154/2_27-1	23727-1	15.05.2019	23:19	BC	16°31.589'	62°02.845'	829	max depth/on ground
M154/2_27-1	23727-1	15.05.2019	23:25	BC	16°31.588'	62°02.847'	952	hoisting
M154/2_28-1	23728-1	15.05.2019	23:54	BC	16°31.584'	62°02.626'	848	lowering
M154/2_28-1	23728-1	16.05.2019	00:00	BC	16°31.584'	62°02.627'	847	max depth/on ground
M154/2_28-1	23728-1	16.05.2019	00:10	BC	16°31.586'	62°02.625'	846	hoisting
M154/2_29-1	23729-1	16.05.2019	00:27	BC	16°31.582'	62°02.489'	913	lowering
M154/2_29-1	23729-1	16.05.2019	00:32	BC	16°31.582'	62°02.490'	828	max depth/on ground
M154/2_29-1	23729-1	16.05.2019	01:04	BC	16°31.584'	62°02.491'	827	on deck
M154/2_30-1	23730-1	16.05.2019	12:30	MEBO	16°37.565'	61°59.010'	1088	in the water
M154/2_30-1	23730-1	16.05.2019	14:14	MEBO	16°37.594'	61°59.012'	1089	max depth/on ground
M154/2_30-1	23730-1	16.05.2019	14:49	MEBO	16°37.595'	61°59.006'	1085	information
M154/2_30-1	23730-1	17.05.2019	00:25	MEBO	16°37.592'	61°59.005'	1086	information
M154/2_30-1	23730-1	17.05.2019	00:33	MEBO	16°37.590'	61°59.010'	1087	hoisting
M154/2_30-1	23730-1	17.05.2019	01:42	MEBO	16°37.643'	61°59.028'	1091	on deck
M154/2_26-3	23726-3	17.05.2019	10:00	GRAB	16°31.586'	62°02.961'	803	in the water
M154/2_26-3	23726-3	17.05.2019	10:33	GRAB	16°31.592'	62°02.918'	884	max depth/on ground
M154/2_26-3	23726-3	17.05.2019	10:53	GRAB	16°31.593'	62°02.924'	957	on deck
M154/2_26-4	23726-4	17.05.2019	11:32	BC	16°31.591'	62°02.929'	833	in the water
M154/2_26-4	23726-4	17.05.2019	12:12	BC	16°31.577'	62°02.918'	818	max depth/on ground
M154/2_26-4	23726-4	17.05.2019	12:42	BC	16°31.578'	62°02.919'	821	on deck
M154/2_27-2	23727-2	17.05.2019	12:56	BC	16°31.576'	62°02.845'	829	in the water
M154/2_27-2	23727-2	17.05.2019	13:36	BC	16°31.575'	62°02.832'	828	max depth/on ground
M154/2_27-2	23727-2	17.05.2019	14:09	BC	16°31.579'	62°02.832'	905	on deck
M154/2_31-1	23731-1	17.05.2019	15:37	MEBO	16°33.723'	62°09.574'	930	in the water
M154/2_31-1	23731-1	17.05.2019	16:59	MEBO	16°33.717'	62°09.570'	929	max depth/on ground
M154/2_31-1	23731-1	17.05.2019	17:31	MEBO	16°33.717'	62°09.565'	930	information
M154/2_31-1	23731-1	18.05.2019	12:45	MEBO	16°33.713'	62°09.563'	929	information
M154/2_31-1	23731-1	18.05.2019	12:48	MEBO	16°33.714'	62°09.569'	928	hoisting

M154/2_31-1	23731-1	18.05.2019	13:48	MEBO	16°33.637'	62°09.575'	931	on deck
M154/2_32-1	23732-1	18.05.2019	15:58	GC	16°37.556'	61°57.558'	672	in the water
M154/2_32-1	23732-1	18.05.2019	16:13	GC	16°37.555'	61°57.557'	672	max depth/on ground
M154/2_32-1	23732-1	18.05.2019	16:30	GC	16°37.556'	61°57.558'	672	on deck
M154/2_33-1	23733-1	18.05.2019	16:45	GC	16°37.413'	61°57.307'	671	in the water
M154/2_33-1	23733-1	18.05.2019	17:00	GC	16°37.415'	61°57.306'	671	max depth/on ground
M154/2_33-1	23733-1	18.05.2019	17:16	GC	16°37.414'	61°57.305'	671	on deck
M154/2_34-1	23734-1	18.05.2019	17:51	GC	16°37.702'	61°58.443'	760	in the water
M154/2_34-1	23734-1	18.05.2019	18:08	GC	16°37.705'	61°58.443'	760	max depth/on ground
M154/2_34-1	23734-1	18.05.2019	18:27	GC	16°37.706'	61°58.443'	760	on deck
M154/2_31-2	23731-2	18.05.2019	20:26	MEBO	16°33.724'	62°09.573'	930	in the water
M154/2_31-2	23731-2	18.05.2019	21:46	MEBO	16°33.713'	62°09.571'	930	max depth/on ground
M154/2_31-2	23731-2	18.05.2019	22:27	MEBO	16°33.711'	62°09.564'	930	information
M154/2_31-2	23731-2	19.05.2019	12:41	MEBO	16°33.698'	62°09.568'	929	information
M154/2_31-2	23731-2	19.05.2019	12:45	MEBO	16°33.700'	62°09.574'	930	hoisting
M154/2_31-2	23731-2	19.05.2019	13:39	MEBO	16°33.614'	62°09.604'	933	on deck
M154/2_11-5	23711-5	19.05.2019	18:09	MEBO	16°46.945'	62°02.206'	855	in the water
M154/2_11-5	23711-5	19.05.2019	19:41	MEBO	16°46.943'	62°02.206'	855	max depth/on ground
M154/2_11-5	23711-5	19.05.2019	20:21	MEBO	16°46.960'	62°02.200'	890	information
M154/2_11-5	23711-5	20.05.2019	12:49	MEBO	16°46.961'	62°02.201'	854	information
M154/2_11-5	23711-5	20.05.2019	12:52	MEBO	16°46.959'	62°02.206'	855	hoisting
M154/2_11-5	23711-5	20.05.2019	13:44	MEBO	16°46.905'	62°02.204'	855	on deck
M154/2_25-2	23725-2	20.05.2019	18:10	MEBO	16°36.736'	62°01.998'	1132	in the water
M154/2_25-2	23725-2	20.05.2019	19:34	MEBO	16°36.735'	62°01.998'	1133	max depth/on ground
M154/2_25-2	23725-2	20.05.2019	20:32	MEBO	16°36.735'	62°01.993'	1133	information
M154/2_25-2	23725-2	22.05.2019	03:00	MEBO	16°36.714'	62°01.998'	1132	information
M154/2_25-2	23725-2	22.05.2019	03:05	MEBO	16°36.717'	62°02.002'	1133	hoisting
M154/2_25-2	23725-2	22.05.2019	04:19	MEBO	16°36.636'	62°01.902'	1134	on deck

7.2.1 Gravity Core Deployment

Station No.		Date	Time	Latitude	Longitude	Water Depth	Coring Length	Remarks/ Recovery
METEOR	GeoB		[UTC]	[N]	[W]	[m]	[cm]	
M154/2_01-1	23701-1	30.04.2019	11:59	16°30.545'	61°57.839'	1190	73	49 %
M154/2_02-1	23702-1	30.04.2019	13:36	16°30.893'	61°58.081'	1180	298	99 %
M154/2_02-4	23702-4	02.05.2019	16:30	16°30.901'	61°58.070'	1179	0	
M154/2_03-1	23703-1	30.04.2019	14:54	16°31.469'	61°57.348'	1176	163	54 %
M154/2_04-1	23704-1	30.04.2019	16:04	16°32.062'	61°56.632'	1160	135	45 %
M154/2_05-1	23705-1	30.04.2019	17:35	16°33.241'	61°55.165'	1112	171	57 %
M154/2_06-1	23706-1	02.05.2019	12:23	16°33.721'	62°11.904'	914	223	74 %
M154/2_07-1	23707-1	02.05.2019	13:52	16°32.384'	62°11.649'	968	47	31 %
M154/2_08-1	23708-1	04.05.2019	10:02	16°43.837'	62°02.236'	961	0	
M154/2_09-1	23709-1	04.05.2019	11:46	16°44.032'	62°02.233'	980	0	
M154/2_10-1	23710-1	04.05.2019	12:39	16°44.153'	62°02.227'	944	88	46 %
M154/2_11-1	23711-1	04.05.2019	13:54	16°46.946'	62°02.223'	856	86	45 %
M154/2_14-1	23714-1	11.05.2019	10:10	16°36.190'	62°01.349'	1139	0	
M154/2_15-1	23715-1	11.05.2019	11:55	16°30.525'	61°58.543'	1166	282	94 %
M154/2_16-1	23716-1	11.05.2019	13:35	16°30.299'	61°58.836'	1140	140	45 %
M154/2_17-1	23717-1	11.05.2019	15:02	16°30.110'	61°59.036'	1104	213	71 %
M154/2_18-1	23718-1	11.05.2019	16:31	16°30.031'	61°59.137'	1101	29	15 %
M154/2_19-1	23719-1	11.05.2019	18:05	16°28.322'	62°01.126'	967	140	73 %
M154/2_20-1	23720-1	11.05.2019	19:28	16°28.331'	62°02.125'	929	0	
M154/2_21-1	23721-1	13.05.2019	15:34	16°33.730'	62°07.501‘	928	43	28 %
M154/2_22-1	23722-1	13.05.2019	16:53	16°32.400'	62°09.364'	969	56	30 %
M154/2_23-1	23723-1	13.05.2019	18:05	16°33.719'	62°09.895'	929	34	18 %
M154/2_24-1	23724-1	13.05.2019	19:26	16°32.375'	62°10.899'	971	56	28 %
M154/2_32-1	23732-1	18.05.2019	15:58	16°37.556'	61°57.558'	672	0	
M154/2_33-1	23733-1	18.05.2019	16:45	16°37.413'	61°57.307'	671	0	
M154/2_34-1	23734-1	18.05.2019	17:51	16°37.702'	61°58.443'	760	0	

7.2.2 Grab Sampler Deployment

Station No.		Date	Time	Latitude	Longitude	Water Depth	Remarks/ Recovery
METEOR	GeoB		[UTC]	[N]	[W]	[m]	
M154/2_12-2	23712-2	07.05.2019	16:16	16°39.768'	62°13.311'	613	
M154/2_13-1	23713-1	07.05.2019	17:15	16°39.825'	62°13.405'	609	
M154/2_26-3	23726-3	17.05.2019	10:00	16°31.586'	62°02.961'	803	

7.2.3 Box Corer Deployment

Station No.		Date	Time	Latitude	Longitude	Water Depth	Remarks/ Recovery
METEOR	**GeoB**		**[UTC]**	**[N]**	**[W]**	**[m]**	
M154/2_12-1	23712-1	07.05.2019	14:01	16°39.767'	62°13.329'	616	
M154/2_26-1	23726-1	15.05.2019	20:15	16°31.582'	62°02.963'	855	
M154/2_26-2	23726-2	15.05.2019	22:00	16°31.589'	62°02.934'	832	
M154/2_26-4	23726-4	17.05.2019	11:32	16°31.591'	62°02.929'	833	
M154/2_27-1	23727-1	15.05.2019	23:11	16°31.588‘	62°02.840‘	914	
M154/2_27-2	23727-2	17.05.2019	12:56	16°31.576'	62°02.845'	829	
M154/2_28-1	23728-1	15.05.2019	23:54	16°31.584'	62°02.626'	848	
M154/2_29-1	23729-1	16.05.2019	00:27	16°31.582'	62°02.489'	913	

7.2.4 MeBo Deployment

Station No.		Deployment Duration	Latitude	Longitude	Water Depth	Drill Depth	Coring Length	Recovery	Borehole Logging	Logging Interval
METEOR	**GeoB**	**[hrs:min]**	**[N]**	**[W]**	**[m]**	**[cm]**	**[cm]**			
M154/2_02-3	23702-3	28:11	16°30.882‘	61°58.065‘	1189	2865	0		CPT Acoustic	520-1036; 1036-1262 2511-270
M154/2_02-5	23702-5	25:21	16°30.883‘	61°58.038‘	1170	3030	2571	1462 cm 57 %	MagSus	2770-270
M154/2_11-2	23711-2	08:45	16°46.949'	62°2.231‘	856	1165	510	85 cm 17 %	CPT	530-1165
M154/2_11-3	23711-3	45:29	16°46.947‘	62°2.229‘	856	6530	5931	2450 cm 41 %	Acoustic	6270-270
M154/2_11-4	23711-4	59:22	16°46.949‘	62°2.235‘	856	7030	2660	493 cm 19 %	CPT MagSus	780-2385 failed
M154/2_11-5	23711-5	19:35	16°46.9470'	62°02.2340'	855	5530	0		SGR MagSus	5270-0 5270-0
M154/2_14-2	23714-2	18:36	16°36.187‘	62°01.330‘	1140	530	510	54 cm 11 %		
M154/2_14-3	23714-3		16°36.185‘	62°01.329‘	1140	2030	0	Stopped due to broken flush tool		
M154/2_14-4	23714-4	15:34	16°36.186‘	62°01.331‘	1140	1530	260	226 cm 87 %		
M154/2_25-1	23725-1	45:18	16°36.728‘	62°02.032‘	1127	4100	400	192 cm 48 %	Acoustic	2520-270
M154/2_25-2	23725-2	34:06	16°46.7270'	62°02.0260'	1133	5530	0		SGR MagSus	5270-0 5270-0
M154/2_30-1	23730-1	13:12	16°37.580‘	61°59.045‘	1088	2530	520	60 cm 12 %	Acoustic	2270-270
M154/2_31-1	23731-1	22:11	16°33.709'	62°09.605'	929	2530	2510	425 cm 17 %	Acoustic	2270-270
M154/2_31-2	23731-2	17:13	16°30.8819‘	62°09.6004'	929	2920	260	159 cm 61 %	CPT SGR MagSus	440-710; 720-760; 920-2920 2520-0 failed

7.2.5 CPT Deployment

Station No.		Date	Time	Latitude	Longitude	Water Depth	Depth	# of Push Tests
METEOR	GeoB		[UTC]	[N]	[W]	[m]	[mbsf]	
M154/2_02-3	23702-3	30.04.2019	20:44	16°30.899'	61°58.037'	1180	5.2 – 12.7	5
M154/2_11-2	23711-2	04.05.2019	15:08	16°46.950'	62°02.217'	855	5.2 – 11.6	3
M154/2_11-4	23711-4	08.05.2019	13:16	16°46.948'	62°02.199'	855	7.7 – 23.7	7
M154/2_31-2	23731-2	18.05.2019	20:26	16°33.724'	62°09.573'	930	4.4 – 29.2	11

7.2.6 Heat Flow Measurements

Station No.		Tool	Latitude	Longitude	Water Depth	Thermal Gradient	Standard Deviation	Heat Flow
METEOR	GeoB		[N]	[W]	[m]	[°/km]	[°/km]	[mW/m^2]
M154/2_15-1	23715-1	PoGo	16°30.525'	61°58.543'	1166	260	10	260
M154/2_16-1	23716-1	PoGo	16°30.299'	61°58.836'	1140	424	17	424
M154/2_17-1	23717-1	PoGo	16°30.110'	61°59.036'	1103	242-290	9	242-290
M154/2_18-1	23718-1	PoGo	16°30.031'	61°59.137'	1101	244	18	244
M154/2_19-1	23719-1	PoGo	16°28.322'	62°01.126'	967	60	44	60
M154/2_02-5	23702-5	Sonic	16°30.886'	61°58.064'	1180	60-150	N/A	60-150
M154/2_11-3	23711-3	Sonic	16°46.943'	62°02.202'	856	80-100	N/A	80-100
M154/2_25-1	23725-1	Sonic	16°36.763'	62°02.077'	1240 (?)	20-50	N/A	20-50
M154/2_30-1	23730-1	Sonic	16°37.565'	61°59.010'	800	100-180	N/A	100-180
M154/2_31-1	23731-1	Sonic	16°33.723'	62°09.574'	1096	26-28	N/A	26-28

8 Data and Sample Storage and Availability

All shipboard data will be transferred to PANGAEA database as soon as they are available and quality checked. Cores are stored in the MARUM core repository and have obtained GeoB ID numbers in addition to the PANGAEA event labels. Cooperation on the obtained data and samples is always welcome and interested scientists may contact the chief scientist (K. Huhn).

9 Acknowledgements

We thank captain Rainer Hammacher and his crew for their excellent, ever-present and always friendly support during the voyage. Funding for M154-2 was provided through the German Science Foundation (Project Sekt).

10 References

Blum, P., 1997. Physical Properties Handbook: A guide to the shipboard measurement of physical properties of deep-sea cores. ODP Technical Notes, 26.

Boudon, G., Le Friant, A., Komorowski, JC., Deplus, C., Semet, M.P., 2007. Volcano flank instability in the Lesser Antilles Arc: diversity of scale, processes, and temporal recurrence. Journal of Geophysical Research, 112: B08205. Doi: 10.1029/2006JB004674.

Boyce, R.E., 1968. Electrical resistivity of modern marine sediments from the Bering Sea. Journal of Geophysical Research, 73(14): 4759-4766. Doi: 10.1029/JB073i014p04759.

Cassidy, M., Trofimovs, J., Palmer, M.R., Talling, P.J., Watt, S.F.L., Moreton, S.G., Taylor, R.N., 2013. Timing and emplacement dynamics of newly recognised mass flow deposits at ~8-12 ka offshore Soufriere Hills volcano, Montserrat: How submarine stratigraphy can complement subaerial eruption histories. Journal of Volcanology and Geothermal Research, 253: 1-14.

Cassidy, M., Trofimovs, J., Watt, S.F.L., Palmer, M.R., Taylor, R.N., Gernon, T.M., Talling, P.J., Le Friant, A., 2014. Multi-stage collapse events in the South Soufriere Hills, Montserrat as recorded in marine sediment cores. In: G. Wadge, R.E.A. Robertson, B. Voight (Eds) The Eruption of Soufrière Hills Volcano, Montserrat from 2000 to 2010. Geological Society, London, Memoirs 39: 383-397.

Clark, T.F., Korgen, B.J., Best, D.M., 1978. Heat flow in the eastern Caribbean. Journal of Geophysical Research, 83: 5883-5891.

Crandell, D.R., 1989. Gigantic debris avalanche of Pleistocene age from ancestral Mount Shasta Volcano, California, and debris-avalanche hazard zonation. U.S. Geological Survey Bulletin 1861.

Crutchley, G.J., Karstens, J., Berndt, C., Talling, P.J., Watt, S.F.L., Vardy, M.E., Hühnerbach, V., Urlaub, M., Sarkar, S., Klaeschen, D., Paulatto, M., Le Friant, A., Lebas, E., Maeno, F, 2013. Insights into the emplacement dynamics of volcanic landslides from high-resolution 3D seismic data acquired offshore Montserrat, Lesser Antilles. Marine Geology, 335: 1-15. Doi: 10.1016/j.margeo.2012.10.004.

Deplus, C., Le Friant, A., Boudon, G., Komorowski, JC., Villemant, B., Harford, C., Ségoufin, J., Cheminée, JL., 2001. Submarine evidence for large-scale debris avalanches in the Lesser Antilles Arc. Earth and Planetary Science Letters, 192(2): 145-157.

Fisher, R.V., Schmincke, HU., 1984. Pyroclastic Rocks. Springer Verlag, Berlin.

Folk, R.L., 1980. Petrology of Sedimentary Rocks. Hemphill Publisher, Austin, Texas.

Freudenthal, T., Wefer, G., 2007. Scientific drilling with the sea floor drill rig MeBo. Scientific Drilling, 5: 63-66. Doi: 10.2204/iodp.sd.5.11.2007.

Freudenthal, T., Wefer, G., 2013. Drilling cores on the sea floor with the remote-controlled sea floor drilling rig MeBo. Geoscience Instrumentation Methods and Data Systems, 2: 329–337. Doi: 10.5194/gi-2-329-2013.

Frey-Martínez, J., Cartwright, J. and James, D., 2006. Frontally confined versus frontally emergent submarine landslides: A 3D seismic characterisation. Marine and Petroleum Geology, 23(5): 585-604.

Hansbo, S., 1957. A new approach to the determination of the shear strength of clay by the fall-cone test. Royal Swedish Geotechnical Institute, Stockholm.

Harford, C.L., Pringle, M.S., Sparks, R.S.J., Young, S.R., 2002. The volcanic evolution of Montserrat using 40Ar/39Ar geochronology. In: T.H. Druitt, B.P. Kokelaar (Eds.) The eruption of Soufriere Hills volcano, Montserrat, from 1995 to 1999. Geological Society, London, Memoirs 21: 93-113.

Hunt, J.E., Wynn, R.B., Masson, D.G., Talling, P.J., Teagle, D.A.H., 2011. Sedimentological and geochemical evidence for multistage failure of volcanic island landslides: A case study from Icod landslide on north Tenerife, Canary Islands. Geochemistry, Geophysics, Geosystems, 12(12): Q12007. Doi: 10.1029/2011GC003740.

Karstens, J., Crutchley, G.J., Berndt, C., Talling, P.J., Watt, S.F.L., Hühnerbach, V., Le Friant, A. Lebas, E., Trofimovs, J., 2013. Emplacement of pyroclastic deposits offshore Montserrat from 3D seismic data. Journal of Volcanology and Geothermal Research, 257: 1-11. Doi: 10.1016/j.jvolgeores.2013.03.004.

Krastel, S., Schmincke, HU., Jacobs, C.L., Rihm, R., Le Bas, T.P., Alibés, B., 2001. Submarine landslides around the Canary Islands. Journal of Geophysical Research, 106(B3): 3977-3997.

Labazuy, P., 1996. Recurrent landslides events on the submarine flank of Piton de la Fournaise volcano (Reunion Island). Geological Society, London, Special Publications, 110(1): 295-306.

Lebas, E., Le Friant, A., Boudon, G., Watt, S.F.L., Talling, P.J., Feuillet, N., Deplus, C., Berndt, C., Vardy, M.E., 2011. Multiple widespread landslides during the long-term evolution of a volcanic island: insights form high-resolution seismic data, Montserrat, Lesser Antilles. Geochemistry, Geophysics, Geosystems, 12(5): Q05006. Doi: 10.1029/2010GC003451.

Le Friant, A., Harford, C.L., Deplus, C., Boudon, G., Sparks, R.S.J., Herd, R.A., Komorowski, J.C., 2004. Geomorphological evolution of Montserrat (West Indies): importance of flank collapse and erosional processes. Journal of the Geological Society, London, 161: 147-160.

Le Friant, A., Ishizuka, O., Boudon, G., Palmer, M.R., Talling, P.J., Villemant, B., Adachi, T., Aljahdali, M., Breitkreuz, C., Brunet, M., Caron, B., Coussens, M., Deplus, C., Endo, D., Feuillet, N., Fraas, A.J., Fujinawa, A., Hart, M.B., Hatfield, R.G., Hornbach, M., Jutzeler, M., Kataoka, K.S., Komorowski, JC., Lebas, E., Lafuerza, S., Maeno, F., Manga, M., Martínez-Colón, M., McCanta, A., Morgan, S., Saito, T., Slagle, A., Sparks, S., Stinton, A., Stroncik, N., Subramanyam, K.S.V., Tamura, Y., Trofimovs, J., Voight, B., Wall-Palmer, D., Wang, F., Watt, S.F.L., 2015. Submarine record of volcanic island construction and collapse in the Lesser Antilles arc: first scientific drilling of submarine volcanic island landslides by IODP Expedition 340. Geochemistry, Geophysics, Geosystems, 16: 420-442. Doi: 10.1002/2014GC005652.

Løvholt, F., Harbitz, C.B., Haugen, K.B., 2005. A parametric study of tsunamis generated by submarine slides in the Ormen Lange/Storegga area off western Norway. Marine and Petroleum Geology, 22(1): 219-231.

Løvholt, F., Pedersen, G., Glimsdal, S., 2010. Coupling of Dispersive Tsunami Propagation and Shallow Water Coastal. Open Oceanography Journal, 4: 71-82.

Manga, M., Hornbach, M.J., Le Friant, A., Ishizuka, O., Stroncik, N., Adachi, T., Aljahadali, M., Boudon, G., Breitkreuz, C., Fraas, A., Fujinawa, A., Hatfield, R., Jutzeler, M., Kataoka, K., Lafuerza, S., Maeno, F., Martinez-Colon, M., McCanta, M., Morgan, S., Palmer, M.R., Saito, T., Slagle, A., Stinton, A.J., Subramanyam, K.S.V., Tamura, Y., Talling, P.J., Villemant, B., Wall-Palmer, D., Wang, F., 2012. Heat

flow in the Lesser Antilles island arc and adjacent back arc Grenada basin. Geochemistry, Geophysics, Geosystems, 13: Q08007.

Masson, D.G., Le Bas, T.P., Grevemeyer, I., Weinrebe, W., 2008. Flank collapse and large-scale landsliding in the Cape Verde Islands, off West Africa. Geochemistry, Geophysics, Geosystems, 9(7): Q07015.

Masson, D.G., Watts, A.B., Gee, M.J.R., Urgeles, R., Mitchell, N.C., Le Bas, T.P., Canals, M., 2002. Slope failures on the flanks of the western Canary Islands. Earth Science Reviews, 57: 1-35.

Mazzullo, J., Graham. A.G., 1988. Handbook for Shipboard Sedimentologists: ODP Technical Note, 8.

McMurtry, G.M., Fryer, G.J., Tappin, D.R., Wilkinson, I.P., Williams, M., Fietzke, J., Garbe-Schoenberg, D., Watts, P., 2004. Megatsunami deposits on Kohala volcano, Hawaii, from flank collapse of Mauna Loa. Geology, 32(9): 741-744.

Moore, J.G., Clague, D.A., Holcomb, R.T., Lipman, P.W., Normark, W.R., Torresan, M.E., 1989. Prodigious submarine landslides on the Hawaiian Ridge. Journal of Geophysical Research, 94(B12): 17,465-17,485.

Moore, J.G., Bryan, W.B., Beeson, M.H., Normark, W.R., 1995. Giant blocks in the South Kona landslide, Hawaii. Geology, 23(2): 125-128.

Moore, J.G., Normark, W.R., 1994. Giant Hawaiian Landslides. Annual Review of Earth and Planetary Sciences, 22: 119-144.

Shepard, F.P., 1954. Nomenclature based on sand-silt-clay ratios. Journal of Sedimentology and Petrology, 24(3): 151–158.

Sousa, J., Voight, B., 1995. Multiple-pulsed debris avalanche emplacement at Mount St. Helens in 1980: Evidence from numerical continuum flow simulations. Journal of Volcanology and Geothermal Research, 66(1-4): 227-250.

Strozyk, F., Strasser, M., Förster, A., Kopf, A.J., Huhn, K., 2010. Slope failure repetition in active margin environments: Constraints from submarine landslides in the Hellenic fore arc, eastern Mediterranean. Journal of Geophysical Research-Solid Earth, 115: B08103. Doi:10.1029/2009JB006841.

Trofimovs, J., Sparks, R.S.J., Talling, P.J., 2008. Anatomy of a submarine pyroclastic flow and associated turbidity current: July 2003 dome collapse, Soufriere Hills volcano, Montserrat, West Indies. Sedimentology, 55: 617–634. Doi: 10.1111/j.1365-3091.2007.00914.x.

Trofimovs, J., Talling, P.J., Fisher, J.K., Hart, M.B., Sparks, R.S.J., Watt, S.F.L., Cassidy, M., Smart, C.W., Le Friant, A., Moreton, S.G., Leng, M.J., 2013. Timing, origin and emplacement dynamics of mass flows offshore of SE Montserrat in the last 110 ka: Implications for landslide and tsunami hazards, eruption history, and volcanic island evolution. Geochemistry, Geophysics, Geosystems, 14: 385–406. Doi:10.1002/ggge.20052.

Urgeles, R., Masson, D.G., Canals, M., Watts, A.B., Le Bas, T.P., 1999. Recurrent large-scale landsliding on the west flank of La Palma, Canary Islands. Journal of Geophysical Research, 104(B11): 25,331-25,348.

Villinger, H., Davis, E.E., 1987. A New Reduction Algorithm for Marine Heat Flow Measurements. Journal of Geophysical Research, 92: 12,846-12,856.

Watt, S.F.L., Talling, P.J., Vardy, M.E., Masson, D.M., Henstock, T.J., Hühnerbach, V., Minshull, T.A., Urlaub, M., Lebas, E., Le Friant, A., Berndt, C., Crutchley, G.J., Karstens, J., 2012b. Widespread and progressive seafloor-sediment failure following volcanic debris avalanche emplacement: landslide dynamics and timing offshore Montserrat. Lesser Antilles. Marine Geology, 323-325: 69-94. Doi: 10.1016/j.margeo.2012.08.002.

Watt, S.F.L., Talling, P.J., Vardy, M.E., Heller, V., Hühnerbach, V., Urlaub, M., Sarkar, S., Masson, D.G., Henstock, T.J., Minshull, T.A., Paulatto, M., Le Friant, A., Lebas, E., Berndt, C., Crutchley, G.J., Karstens, J., Stinton, A.J., Maeno, F., 2012a. Combinations of volcanic-flank and seafloor-sediment failure offshore Montserrat, and their implications for tsunami generation. Earth and Planetary Science Letters, 319-320: 228-240. Doi: 10.1016/j.epsl.2011.11.032.

Watts, A.B, Masson, D.G., 1995. A giant landslide on the north flank of Tenerife, Canary Islands. Journal of Geophysical Research, 100(B12): 24,487-24,498.

Wentworth, C.K., 1922. A scale of grade and class terms for clastic sediments. Journal of Geology, 30: 377-392.

Williams, M., Wilkinson, I.P., Tappin, D.R., McMurty, G., Fryer, G.J., 2006. The Hawaiian megatsunami of 110¬±10 ka: the use of microfossils in detection. Journal of Micropalaeontology, 25(1): 55-56.

Wolfe, C.J., McNutt, M.K., Detrick, R.S., 1994. The Marquesas archipelagic apron: Seismic stratigraphy and implications for volcano growth, mass wasting, and crustal underplating. Journal of Geophysical Research, 99(B7): 13,591-13,608.

Wood, D.M., 1985. Some fall-cone tests. Géotechnique, 38: 64-68.

Wynn, R.B., Masson, D.G., 2003. Canary islands landslides and tsunami generation: Can we suse turbidite deposits to interpret landslide processes? In: J. Locat, J. Mienert (Eds) Submarine mass movements and their consequences. Kluwer Academic Publishers, 325-332.

11 Appendices

Appendix A – Core Recovery

MeBo Cores

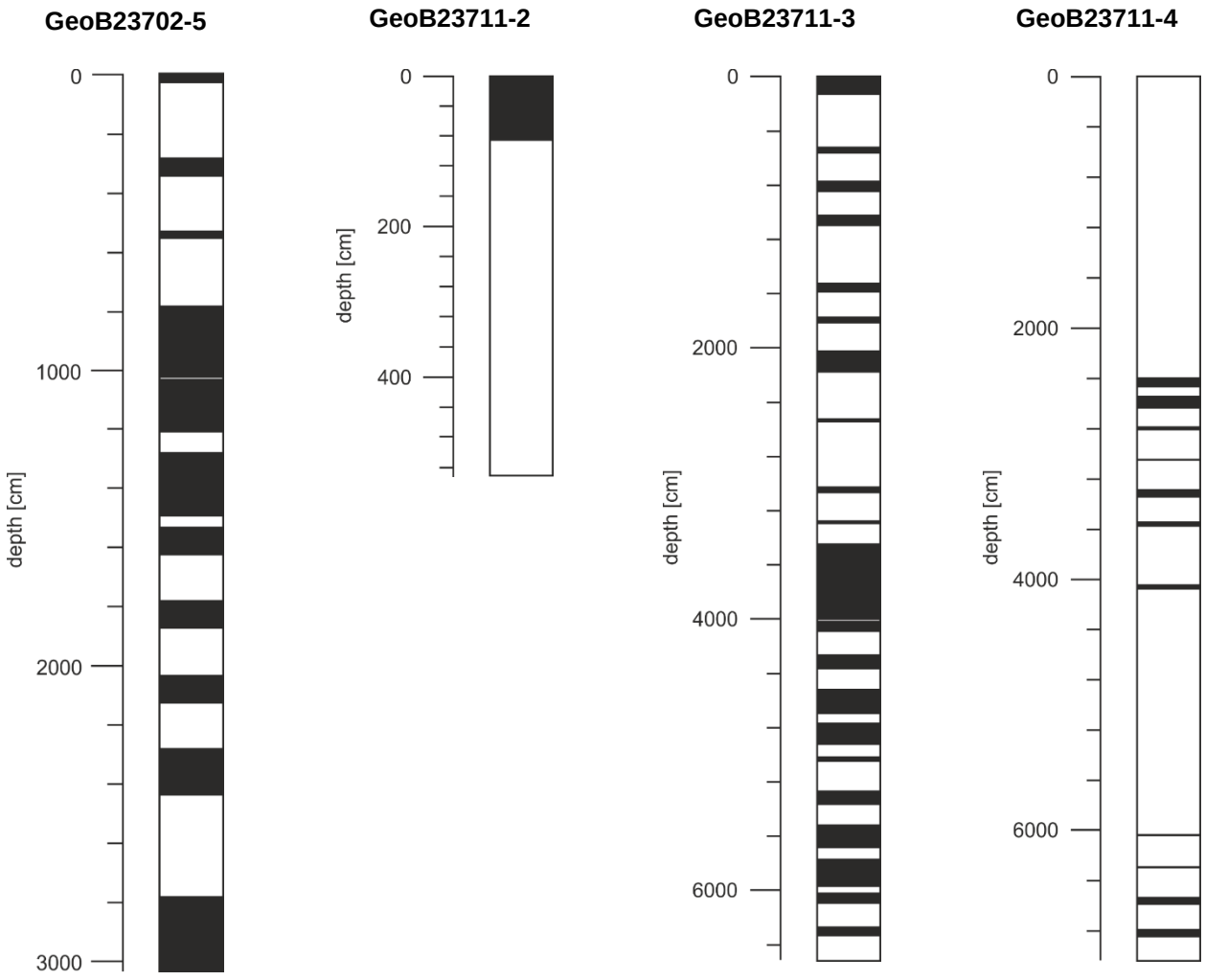

GeoB23714-2

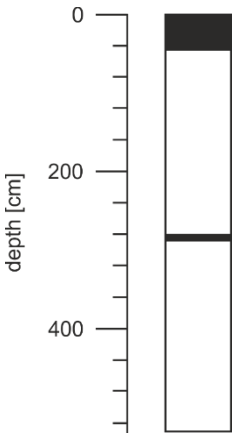

GeoB23714-4

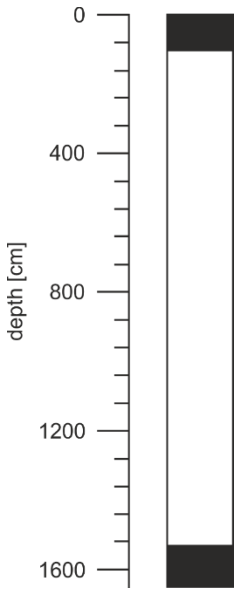

GeoB23725-1

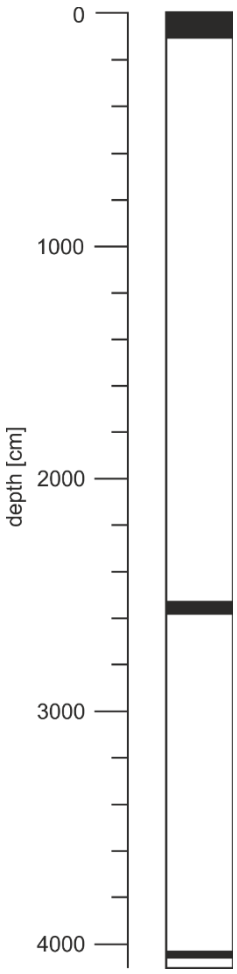

GeoB23730-1

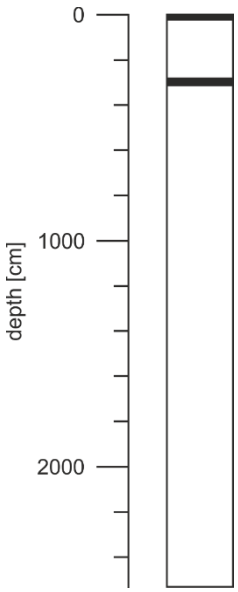

GeoB23731-1

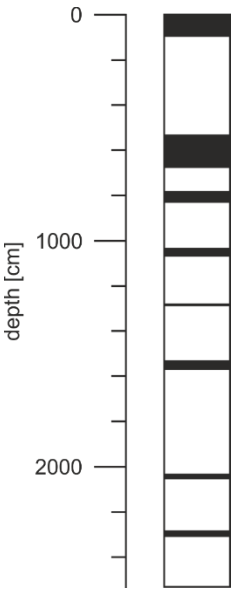

GeoB23731-2

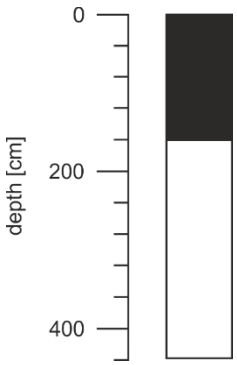

Appendix B – Core Images and Core Description

Gravity Cores

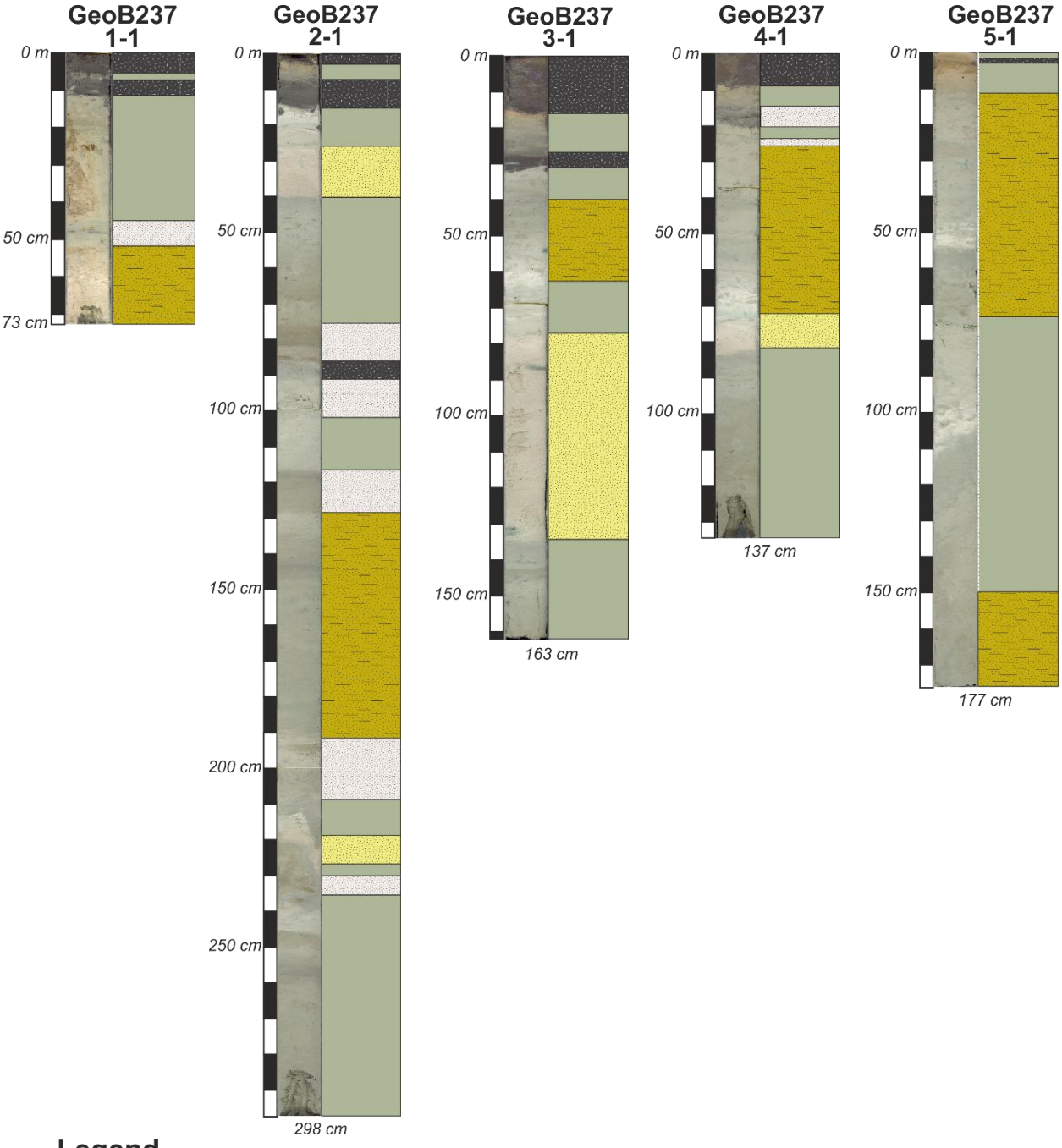

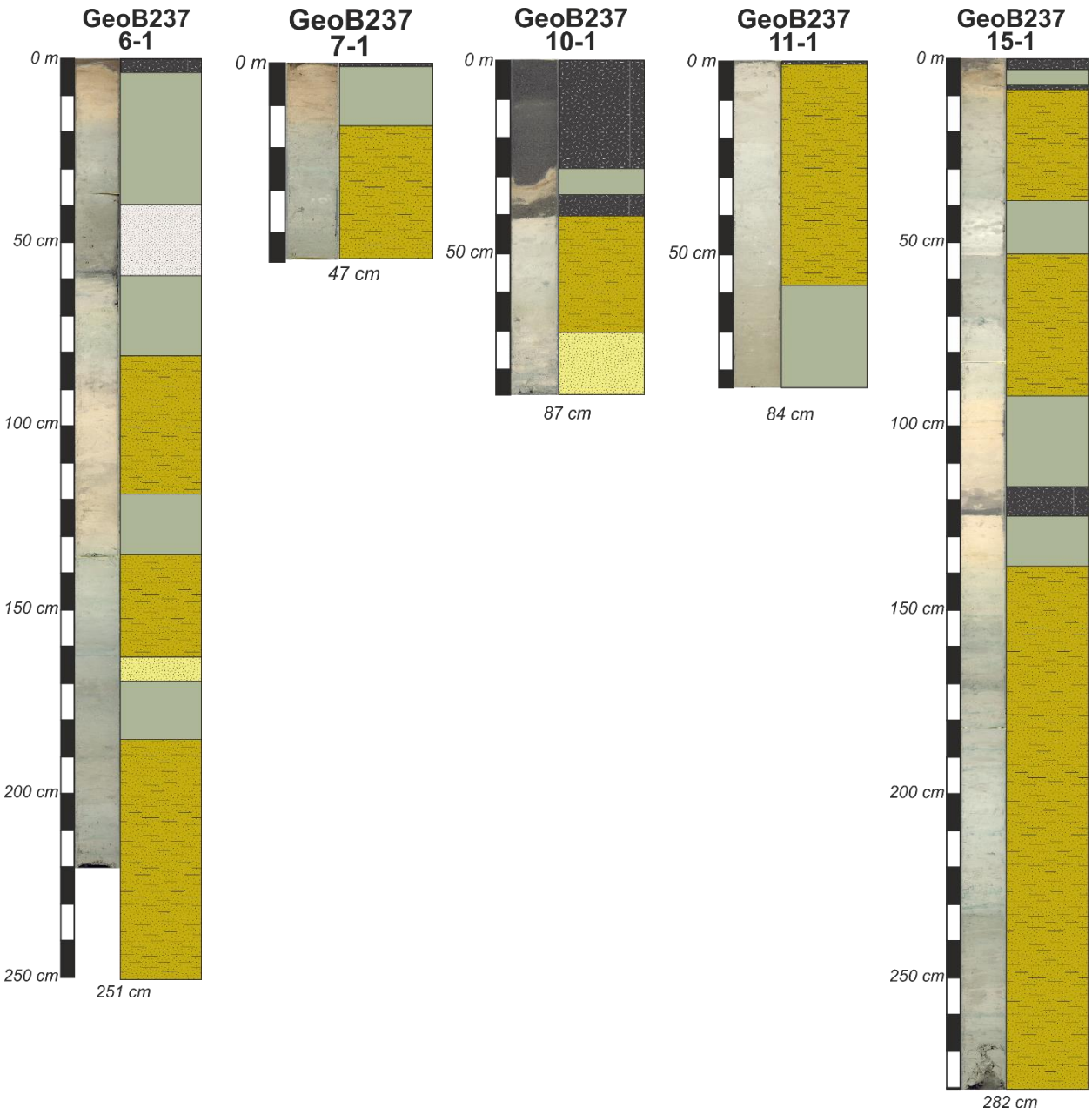

Legend

- hemipelagic background mud with different amount of volcanoclastics
- fine sand with mixture of volcanoclasts and bioclasts
- silty clay with patchy distributed fine to coarse sand clasts and/or rounded mud clasts
- medium sand with mostly volcanoclasts
- fine to medium sand with mostly bioclasts
- coarse to gravely volcanoclastic sand

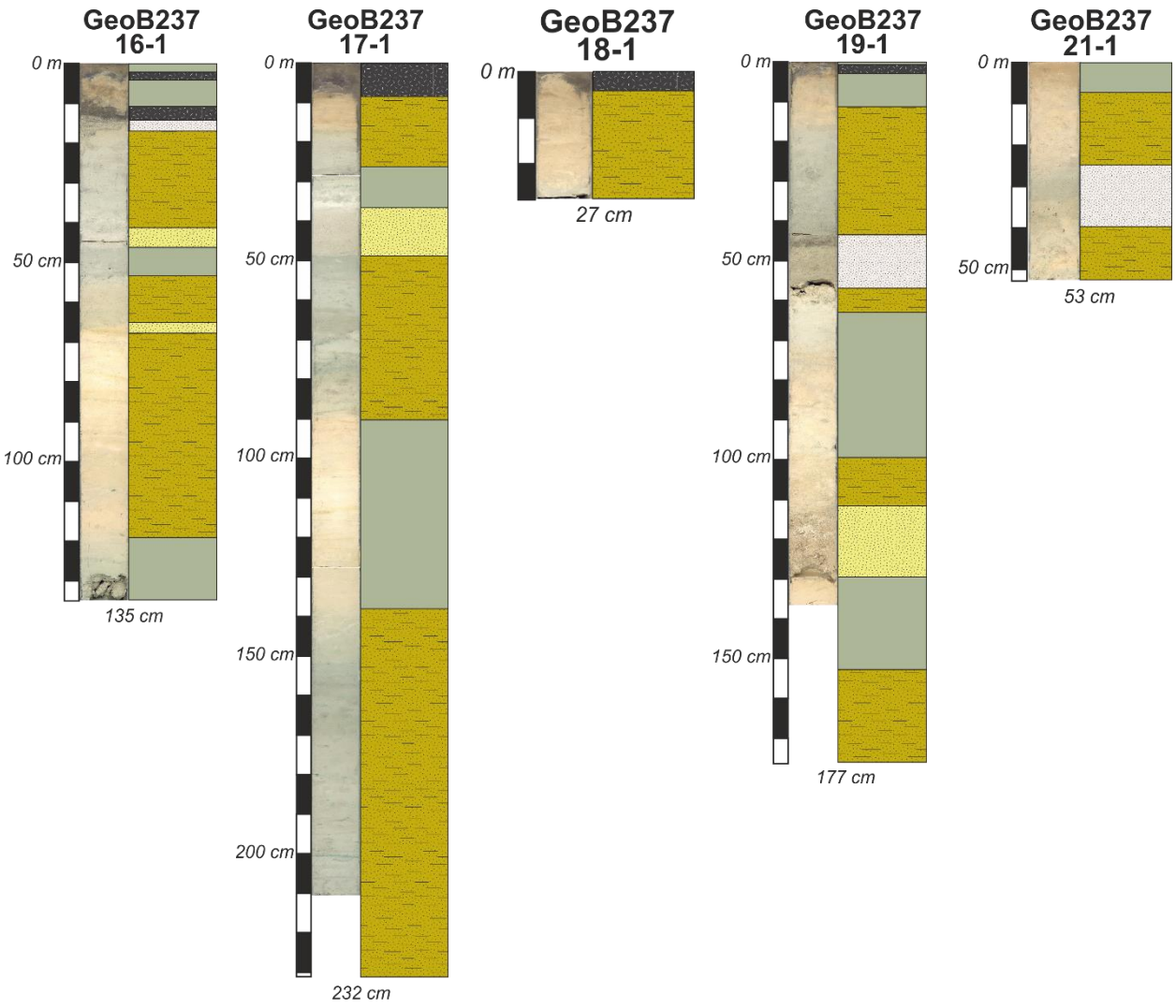

Legend

- hemipelagic background mud with different amount of volcanoclastics
- fine sand with mixture of volcanoclasts and bioclasts
- silty clay with patchy distributed fine to coarse sand clasts and/or rounded mud clasts
- medium sand with mostly volcanoclasts
- fine to medium sand with mostly bioclasts
- coarse to gravely volcanoclastic sand

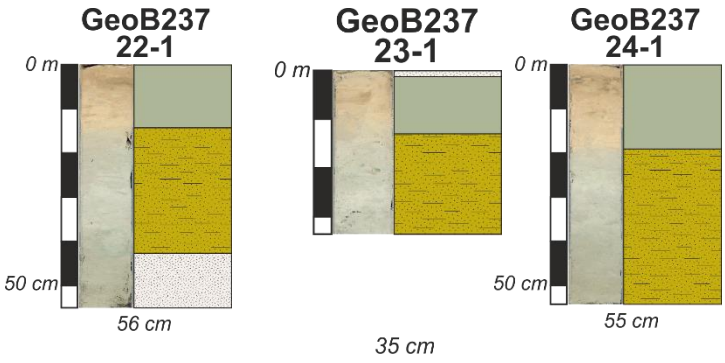

Legend

- hemipelagic background mud with different amount of volcanoclastics
- fine sand with mixture of volcanoclasts and bioclasts
- silty clay with patchy distributed fine to coarse sand clasts and/or rounded mud clasts
- medium sand with mostly volcanoclasts
- fine to medium sand with mostly bioclasts
- coarse to gravely volcanoclastic sand

Appendix C – Sample List

Station Number	Instrument	Sediment Samples	Smear Slides	MAD	Fall Cone Tests	Vane Shear Tests
23701-1	GC	5	7	4	9	2
23702-1	GC	16	16	6	30	6
23703-1	GC	8	8	4	16	4
23704-1	GC	4	4	3	11	3
23705-1	GC	2	0	4	16	4
23705-2	MeBo	46	35	28	112	22
23706-1	GC	7	7	5	23	6
23707-1	GC	0	0	1	4	1
23710-1	GC	13	5	2	8	1(5)
23711-2	MeBo	4	4	1	7	1
23711-3	MeBo	105	99	49	197	46
23711-4	MeBo	29	11	7	29	9
23711-1	GC	3	3	2	8	2
23713-1	MeBo	1	0	0	0	0
23714-2	MeBo	5	3	0	4	2
23714-4	MeBo	13	6	4	23	5
23715-1	GC	11	6	10	26	5
23716-1	GC	7	3	3	12	3
23717-1	GC	3	0	7	21	7
23718-1	GC	1	1	1	3	1
23719-1	GC	8	5	5	12	4
23721-1	GC	3	2	2	6	2
23722-1	GC	1	1	1	5	2
23723-1	GC	1	1	1	4	1
23724-1	GC	2	1	1	5	1
23725-1	MeBo	16	11	3	13	3
23730-1	MeBo	5	2	1	3	1
23731-1	MeBo	45	11	8	36	9
23731-2	MeBo	9	2	3	14	3
Total		**375**	**256**	**165**	**655**	**157**

Appendix D – Physical Properties

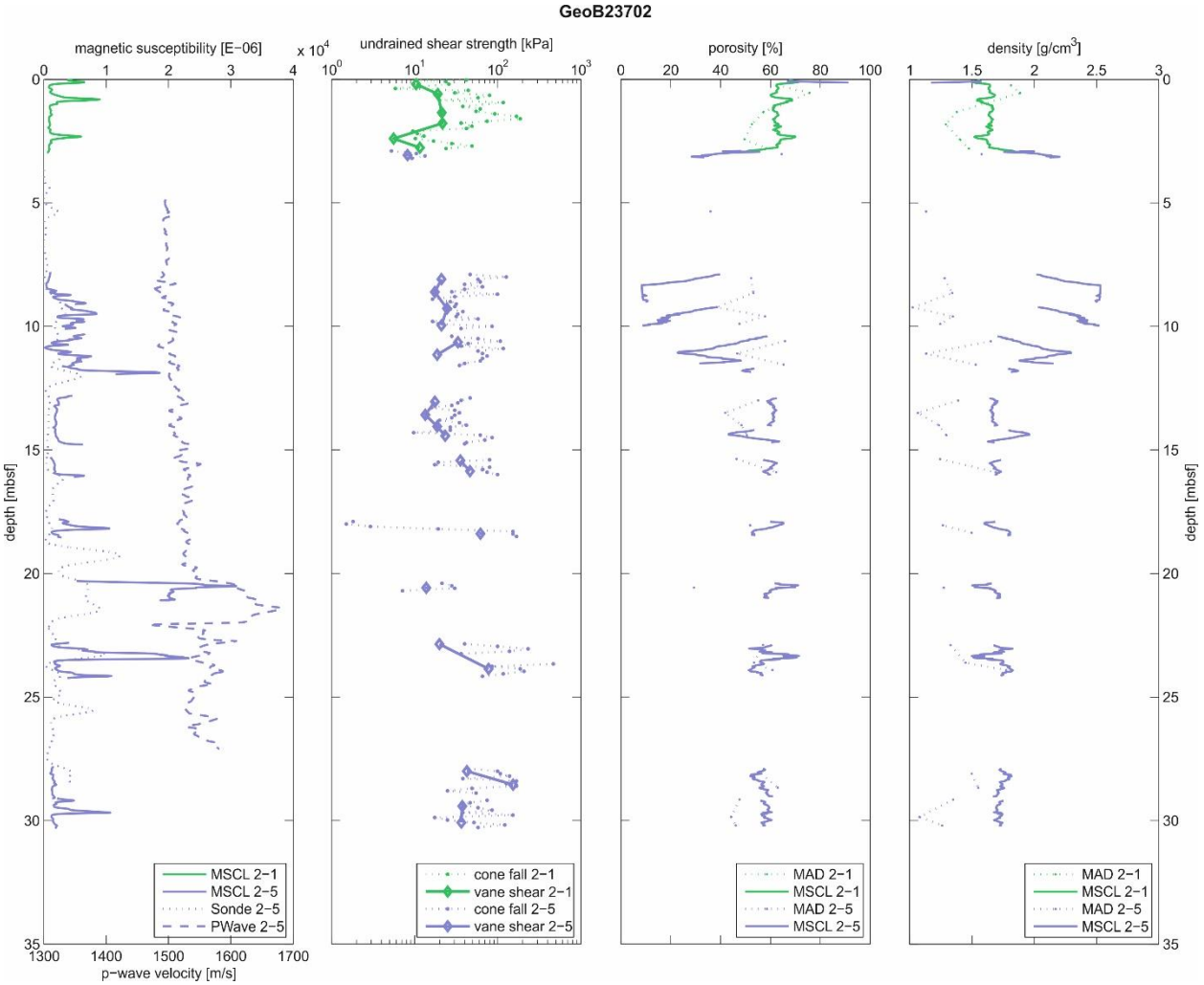

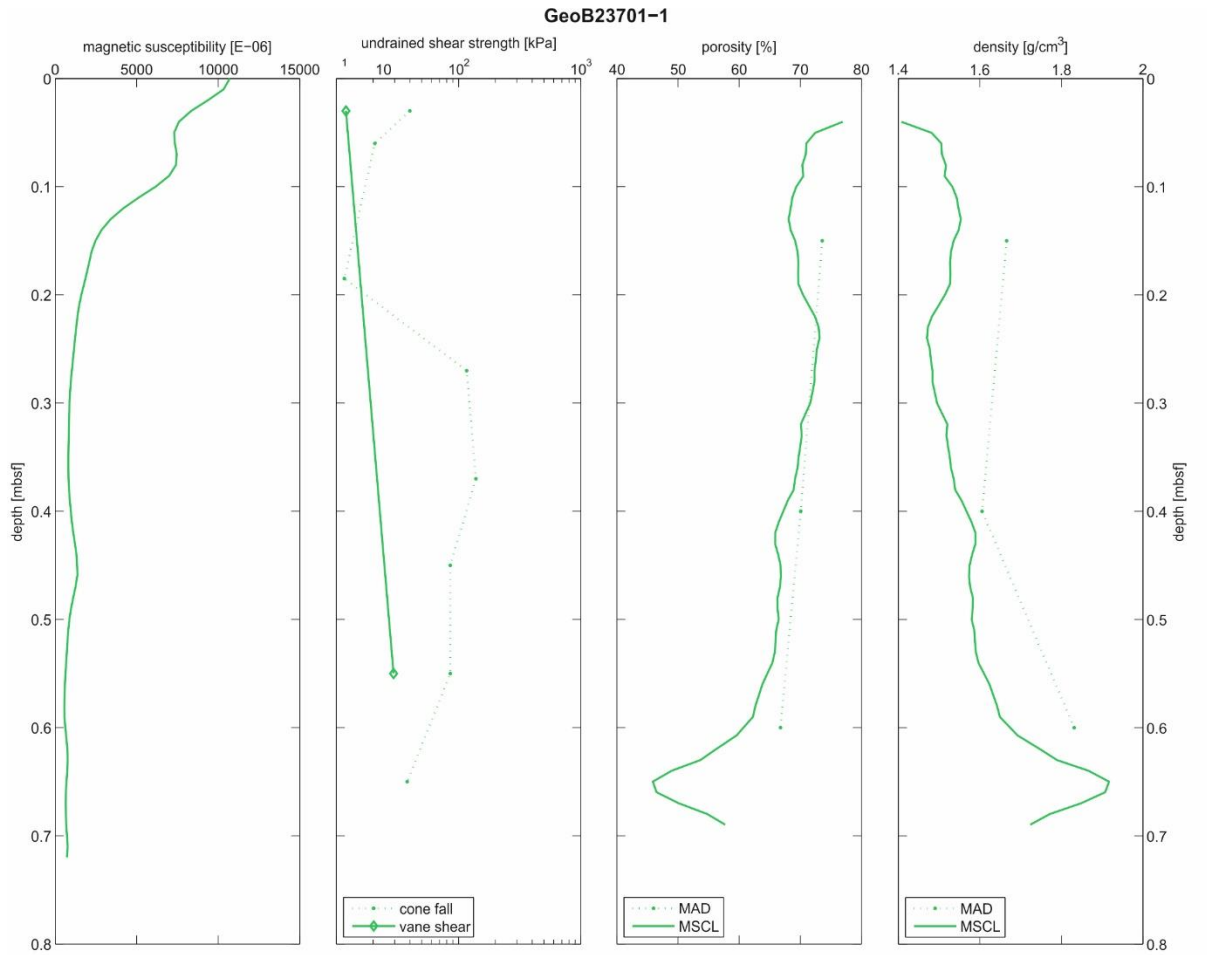
GeoB23701-1
magnetic susceptibility [E-06]
undrained shear strength [kPa]
porosity [%]
density [g/cm3]
depth [mbsf]
cone fall
vane shear
MAD
MSCL

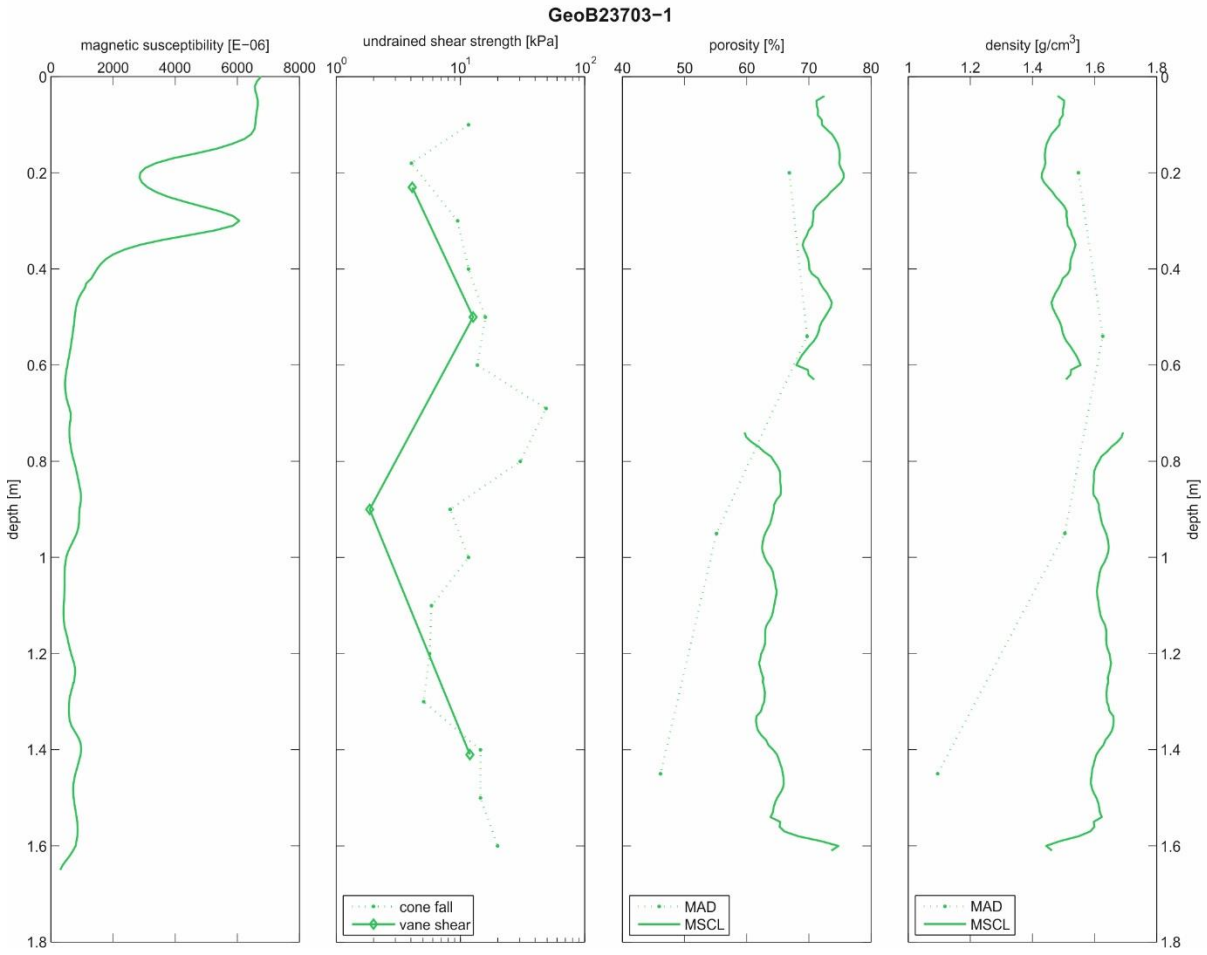
GeoB23703-1
magnetic susceptibility [E-06]
undrained shear strength [kPa]
porosity [%]
density [g/cm3]
depth [m]
cone fall
vane shear
MAD
MSCL

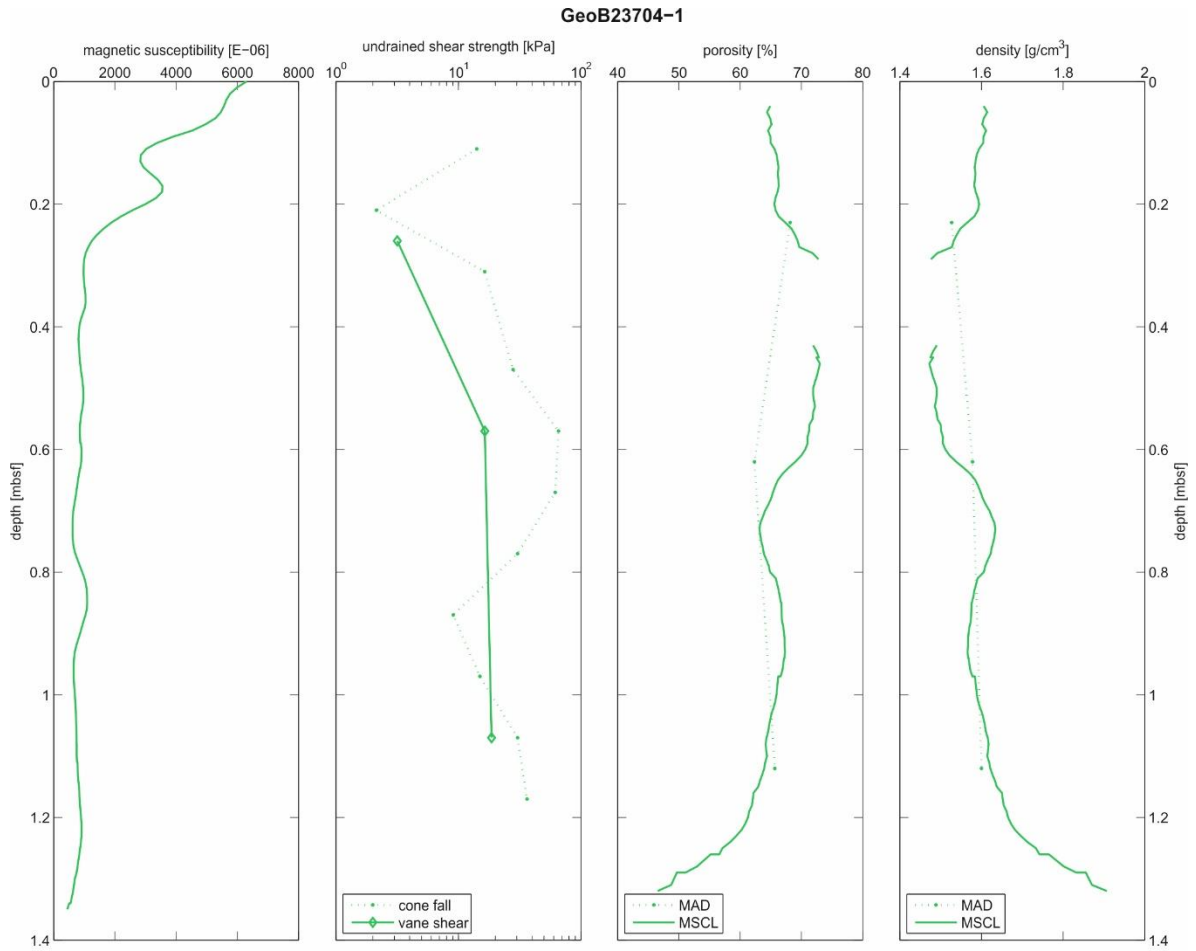
GeoB23704−1
magnetic susceptibility [E−06]
undrained shear strength [kPa]
porosity [%]
density [g/cm3]
depth [mbsf]
cone fall
vane shear
MAD
MSCL

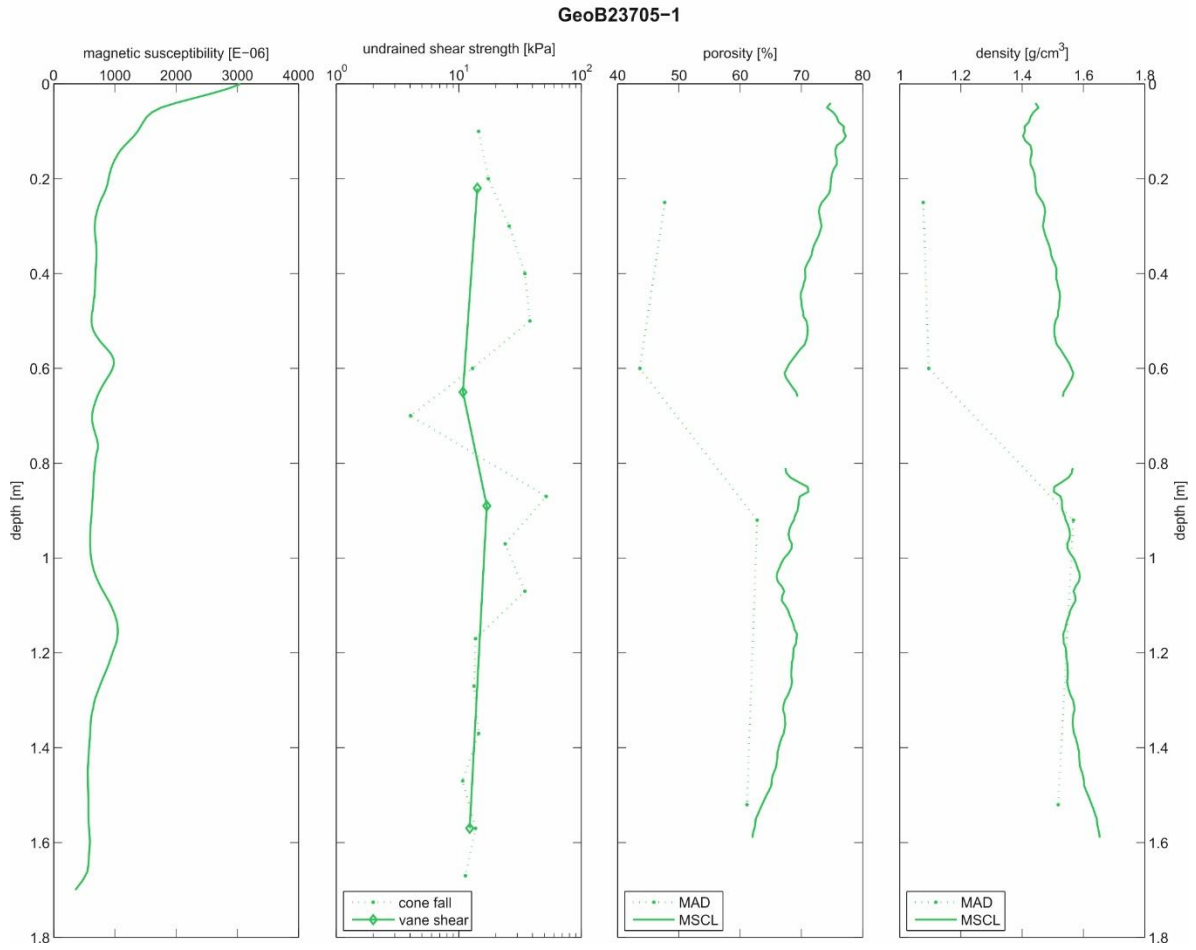
GeoB23705−1
magnetic susceptibility [E−06]
undrained shear strength [kPa]
porosity [%]
density [g/cm3]
depth [m]
cone fall
vane shear
MAD
MSCL

GeoB23706-1

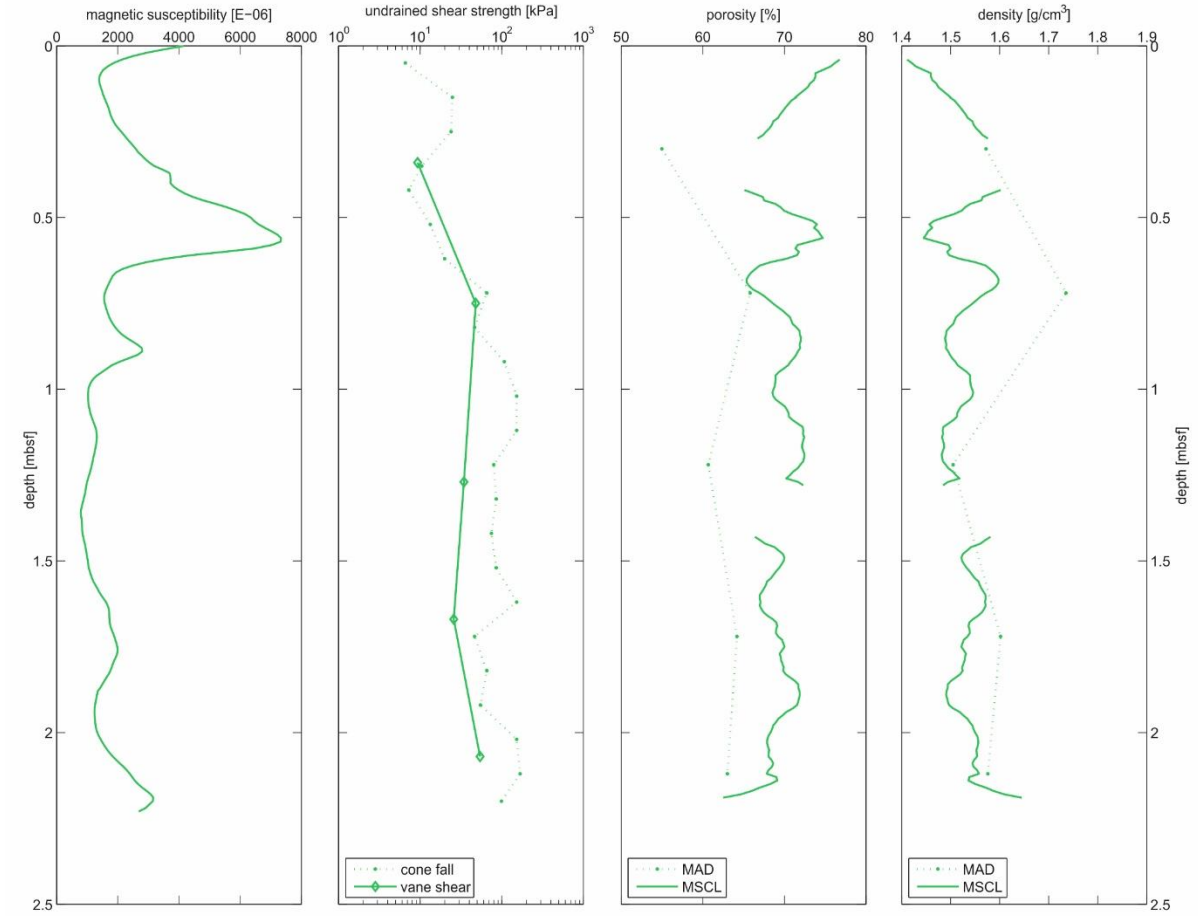

GeoB23707-1

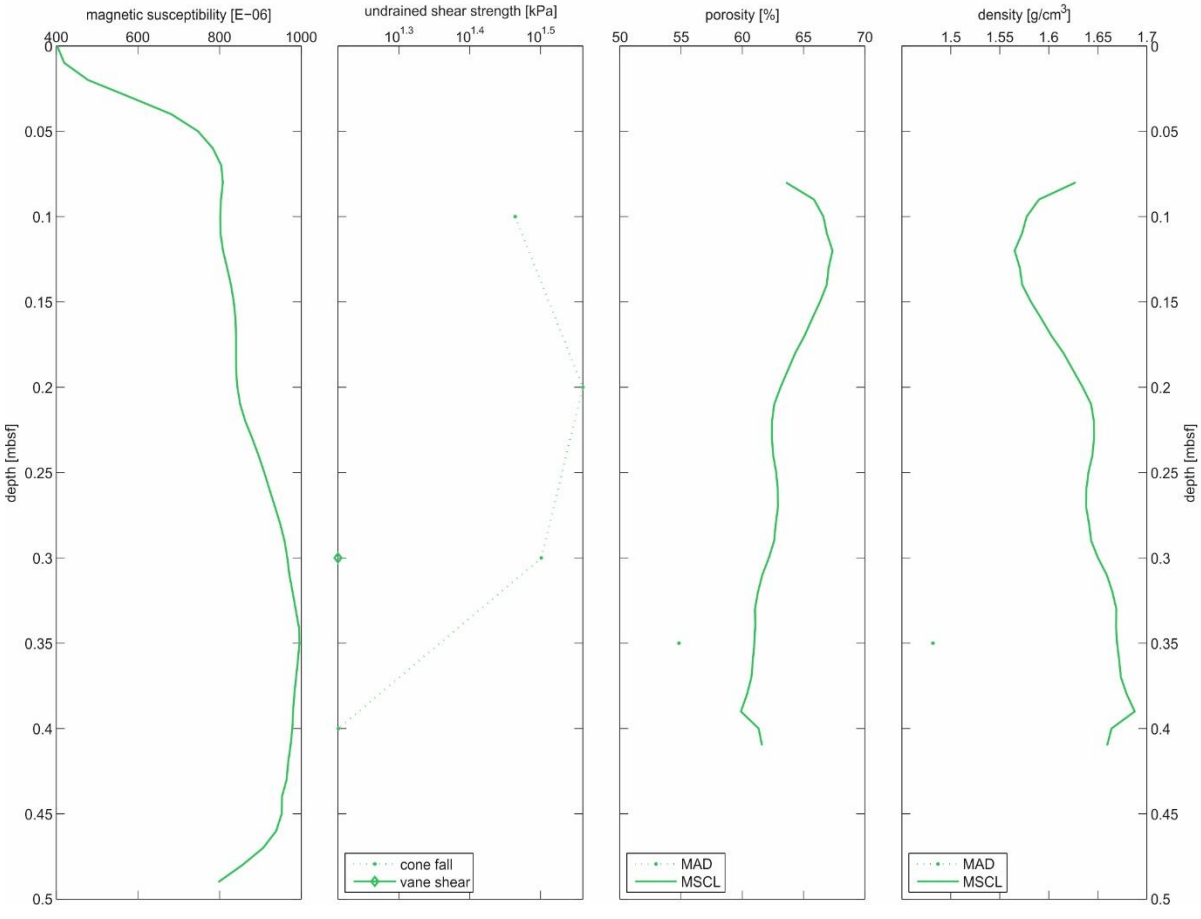

GeoB23710−1

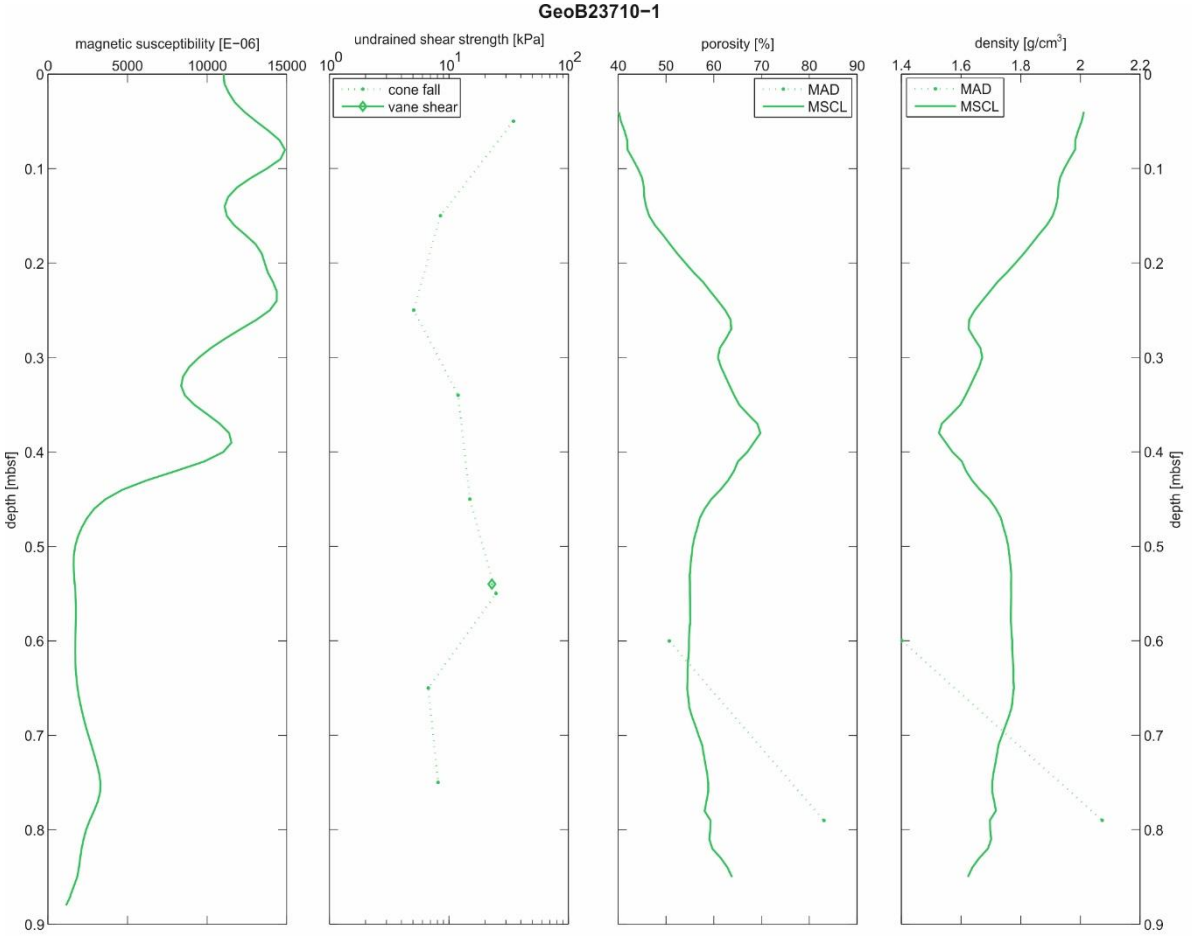

GeoB23711

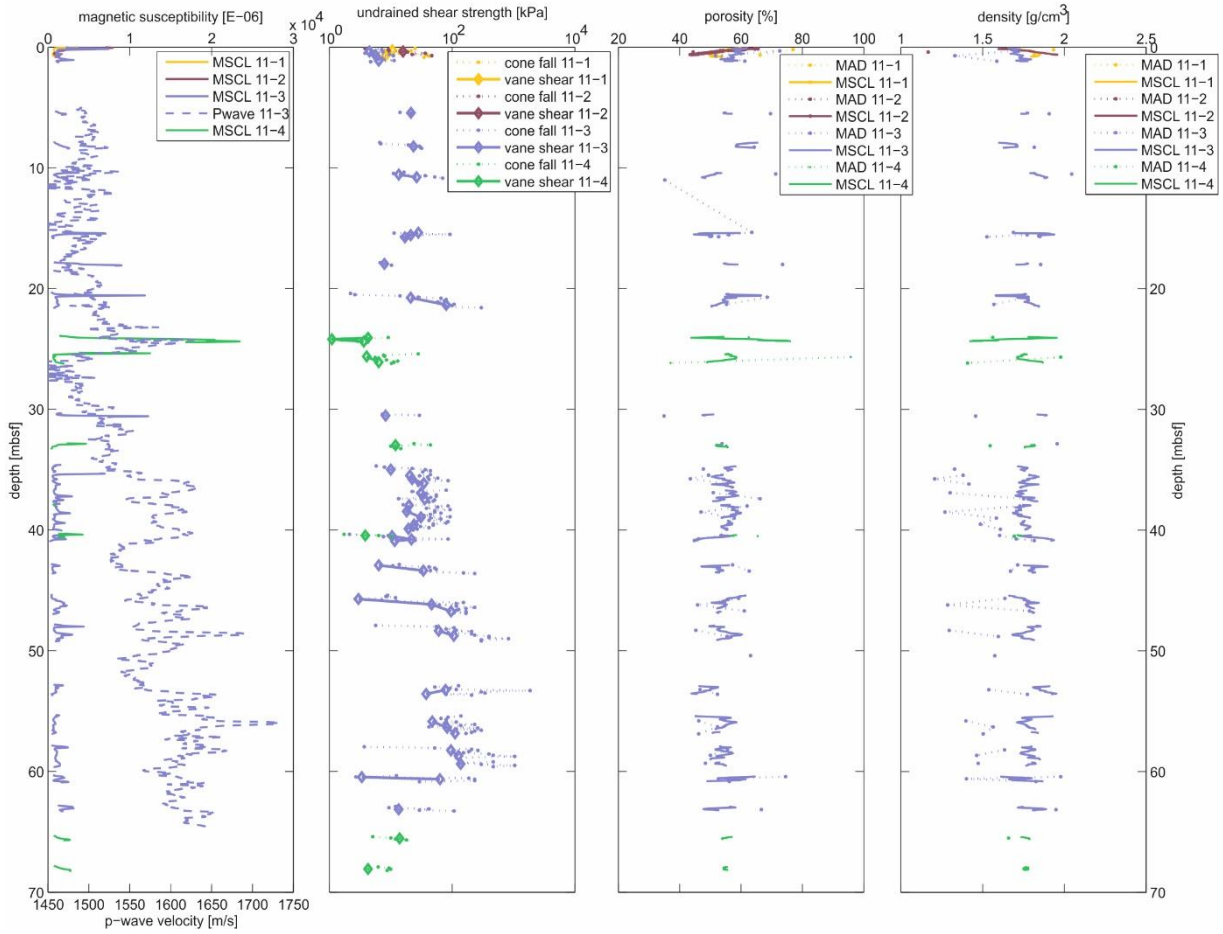

GeoB23714

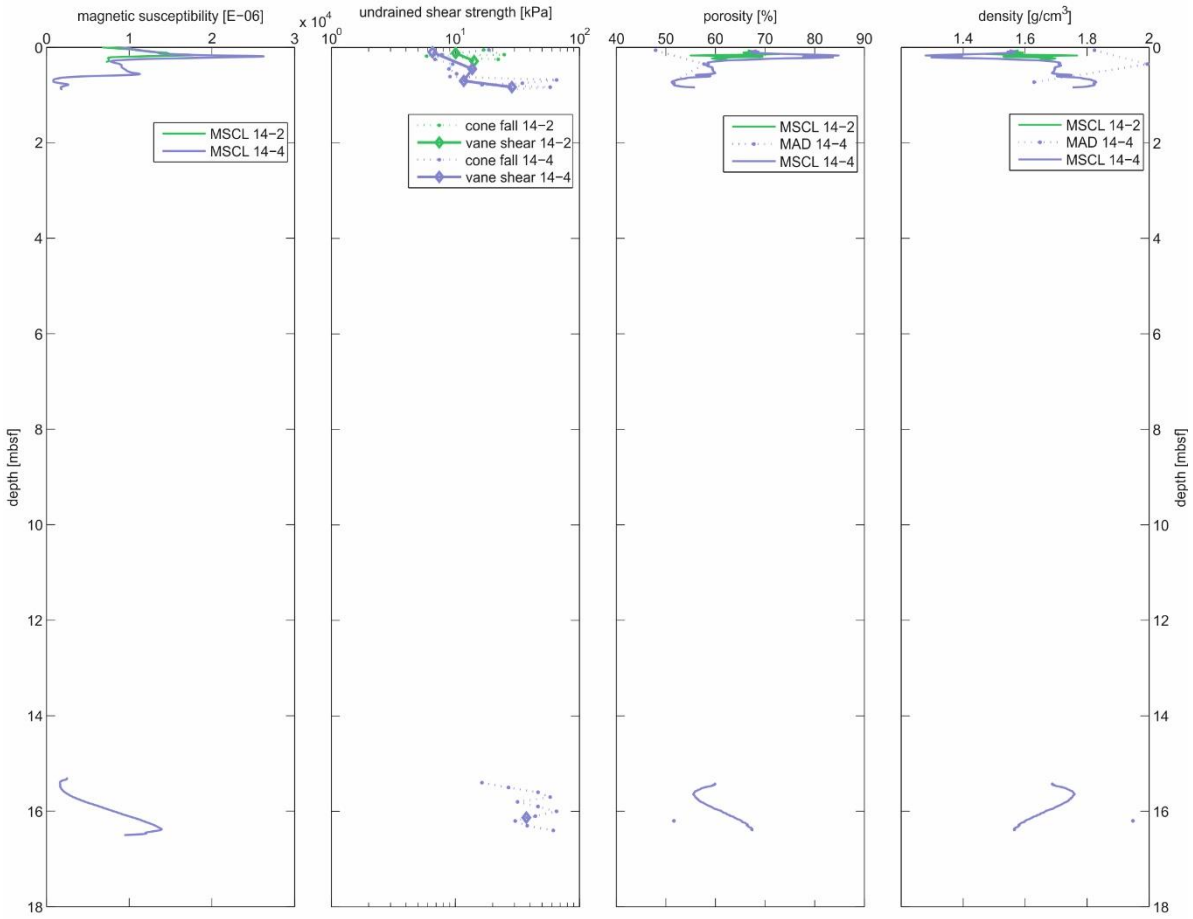

GeoB23705−1

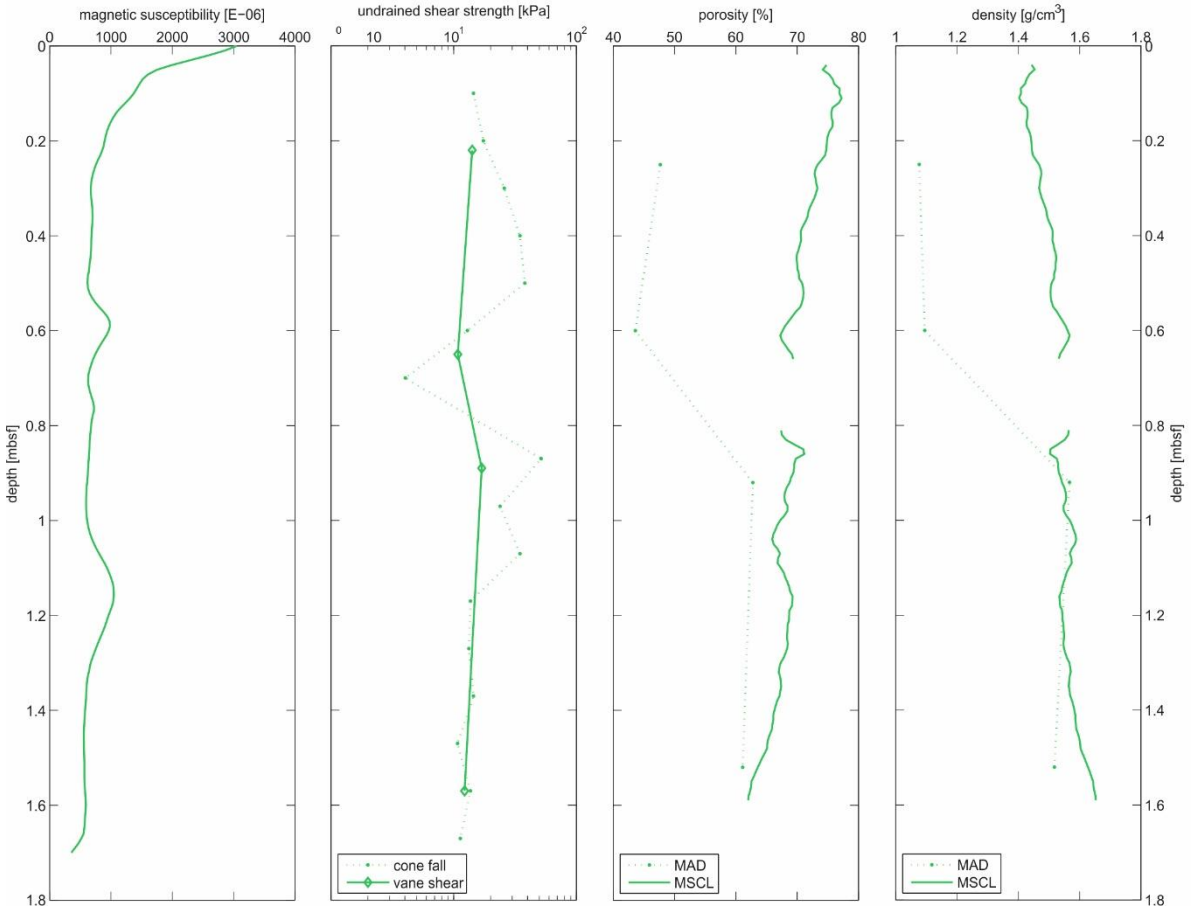

GeoB23716-1

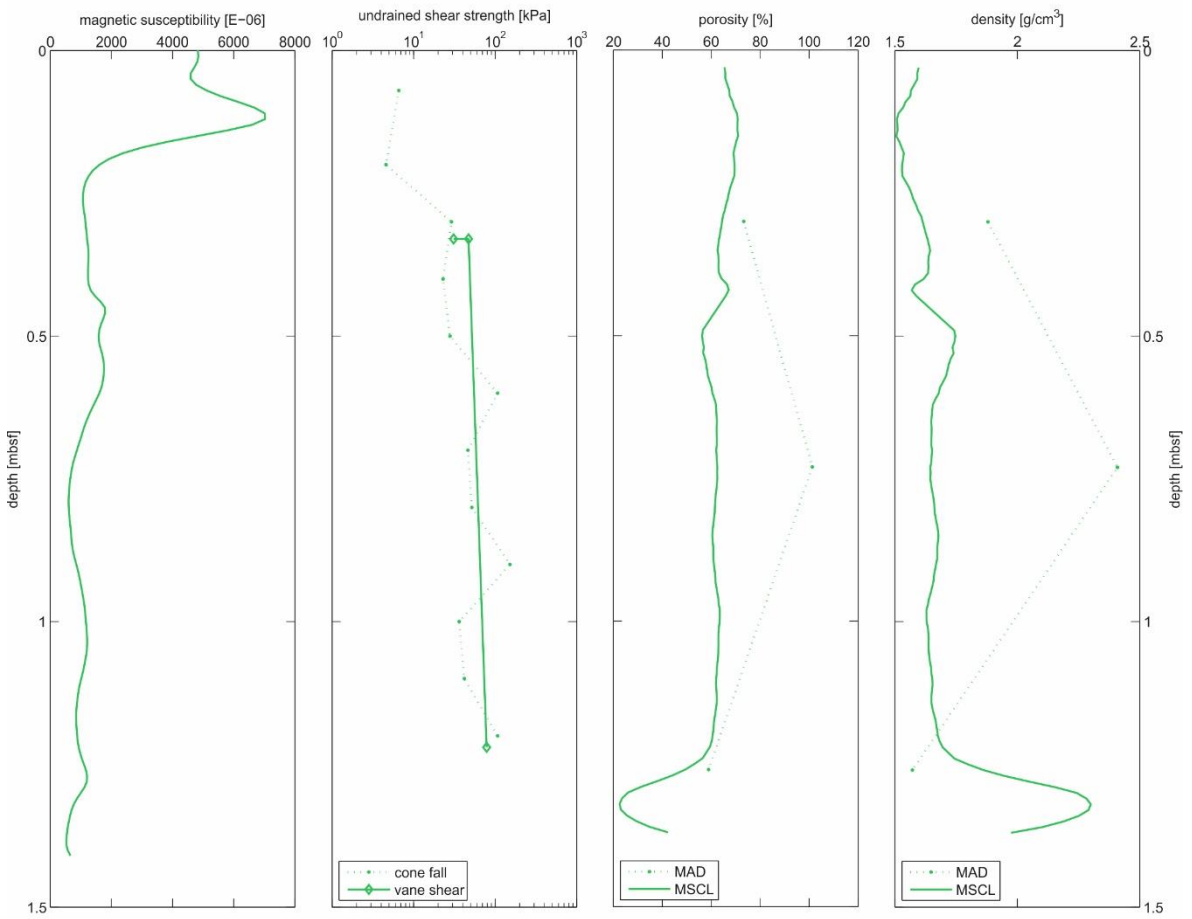

GeoB23717-1

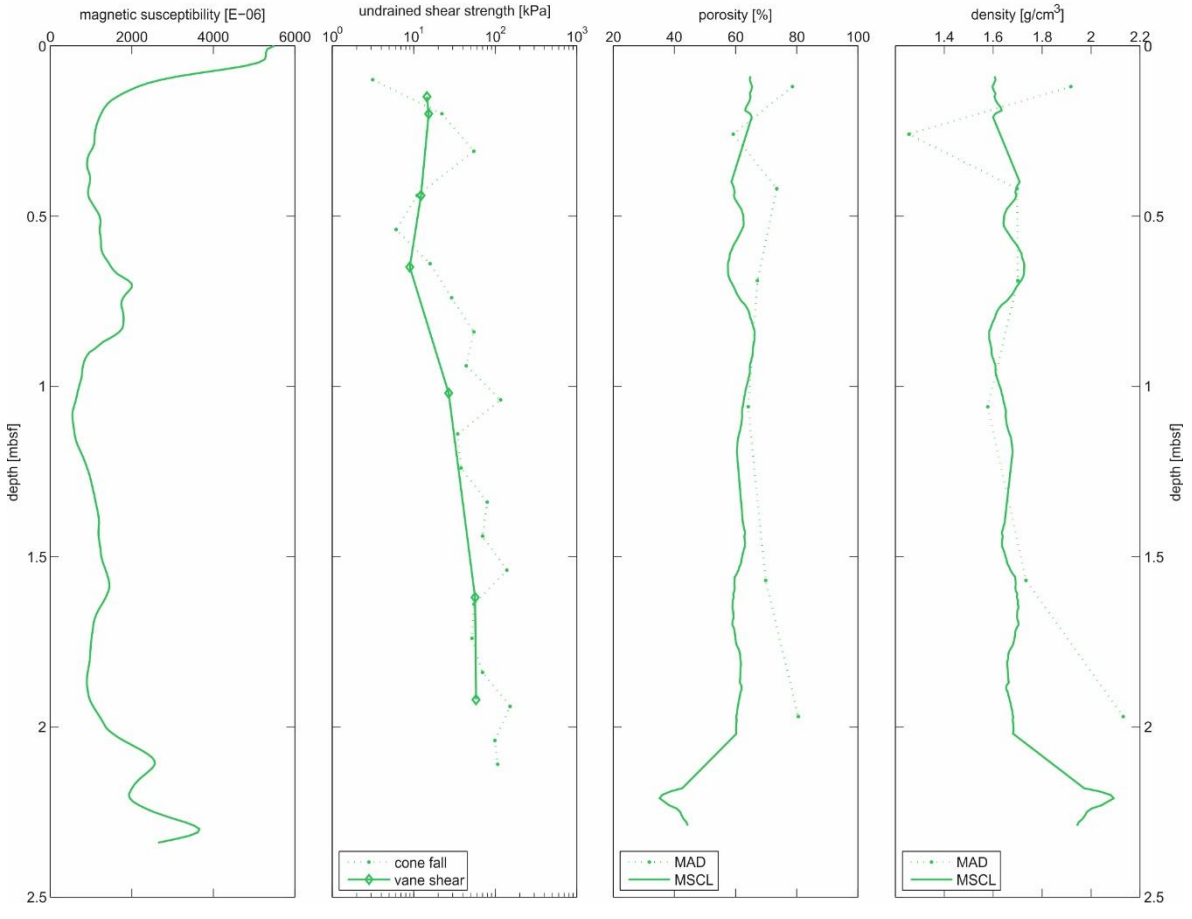

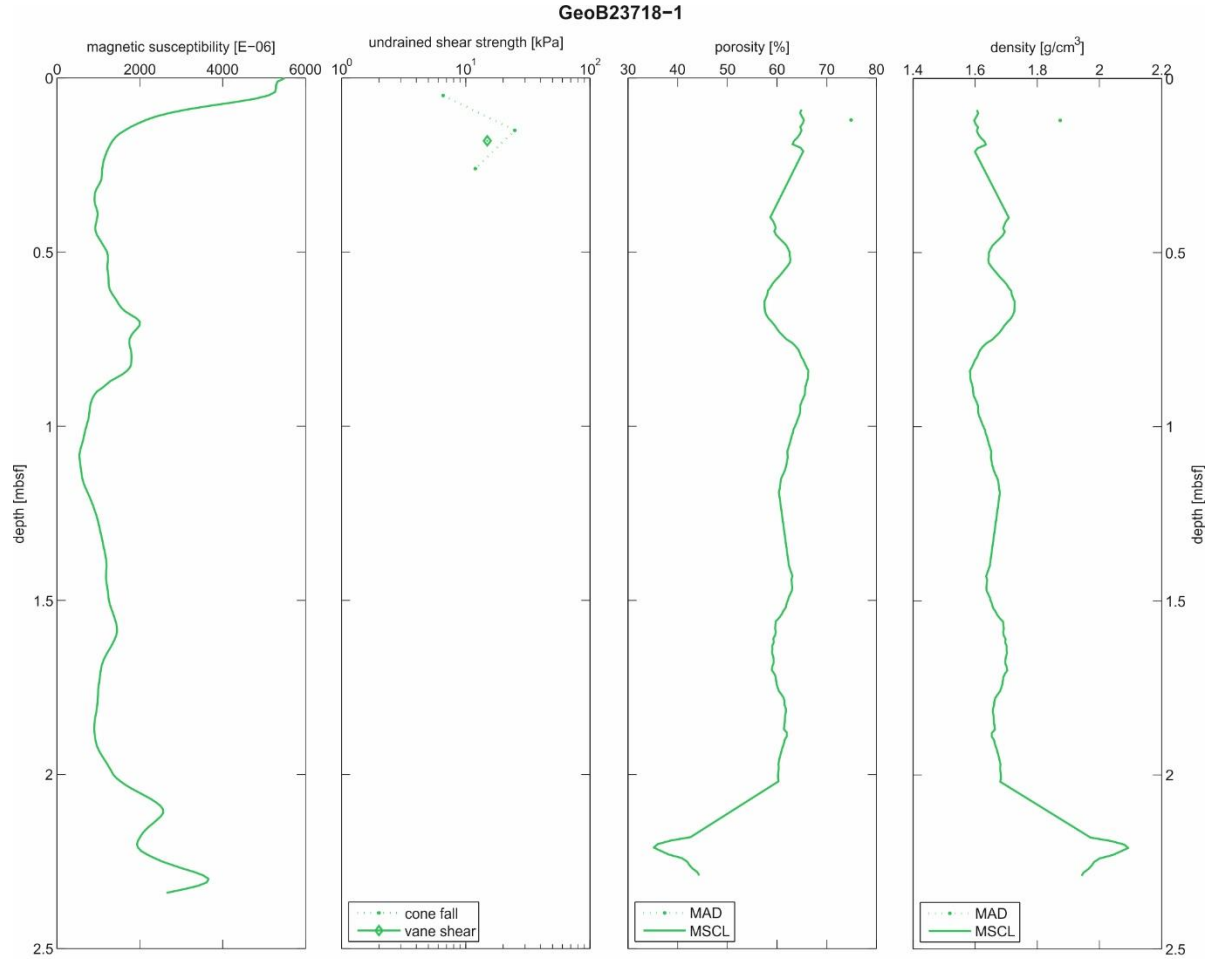
GeoB23718-1
magnetic susceptibility [E-06]
undrained shear strength [kPa]
porosity [%]
density [g/cm3]
depth [mbsf]
cone fall
vane shear
MAD
MSCL

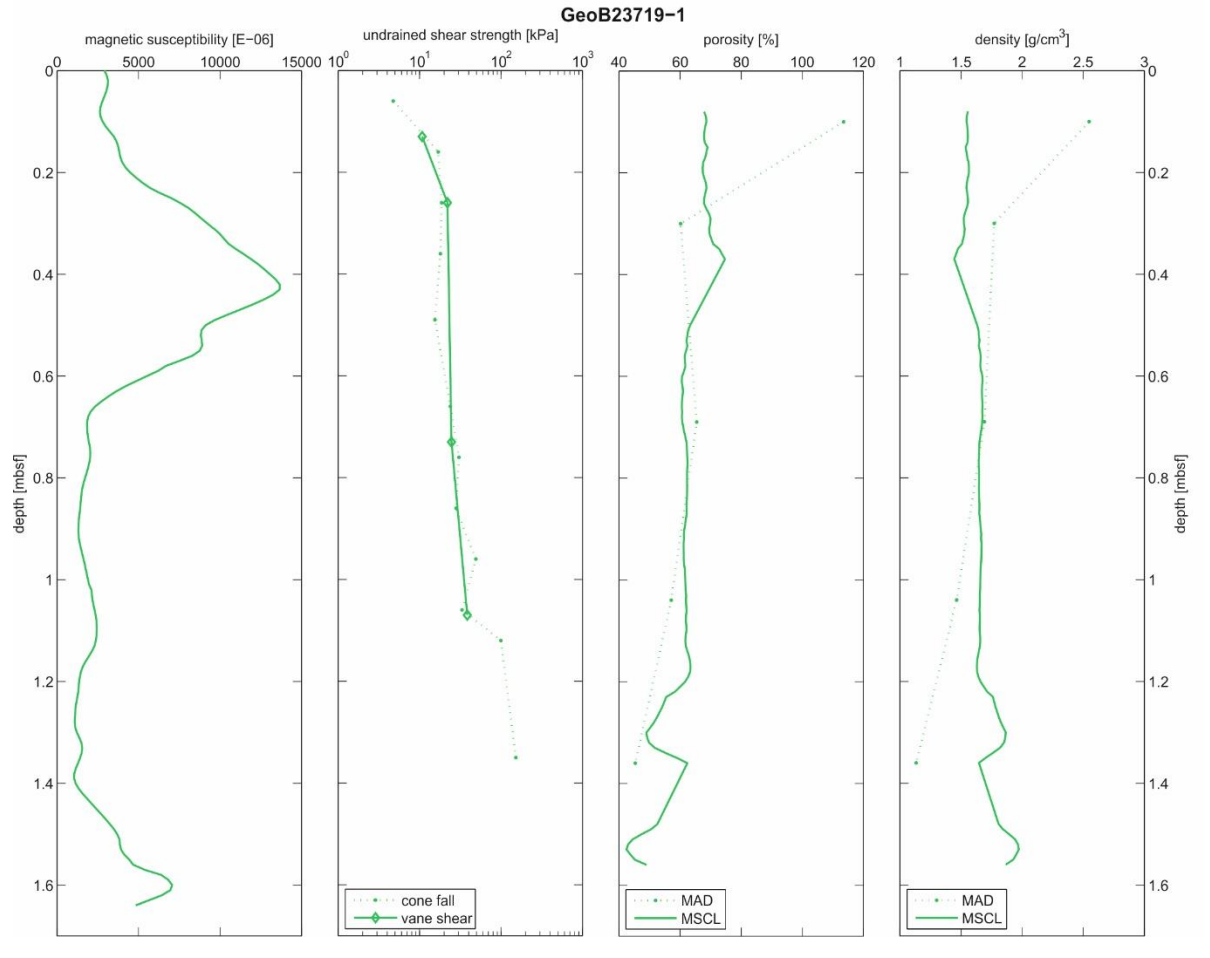
GeoB23719-1
magnetic susceptibility [E-06]
undrained shear strength [kPa]
porosity [%]
density [g/cm3]
depth [mbsf]
cone fall
vane shear
MAD
MSCL

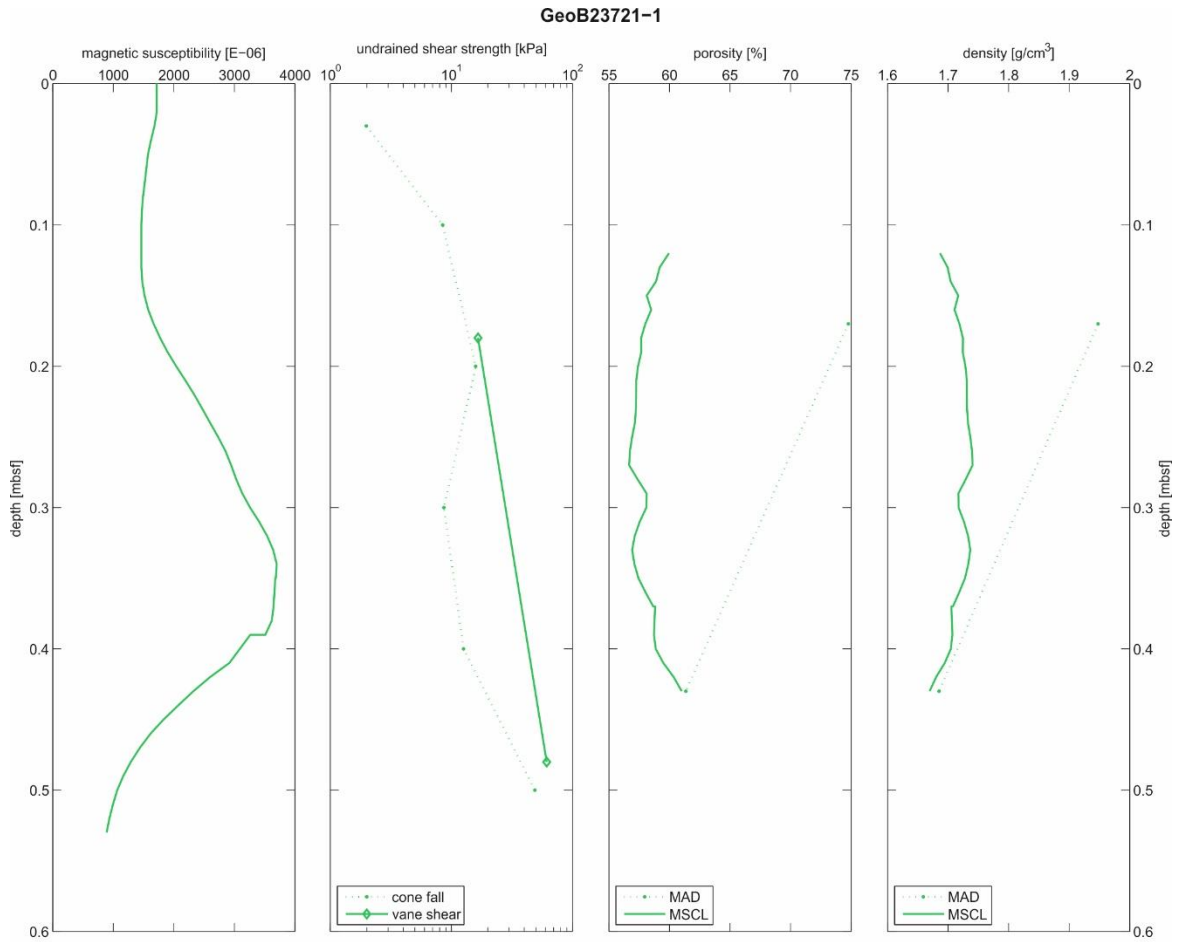
GeoB23721−1
magnetic susceptibility [E−06]
undrained shear strength [kPa]
porosity [%]
density [g/cm3]
depth [mbsf]
cone fall
vane shear
MAD
MSCL

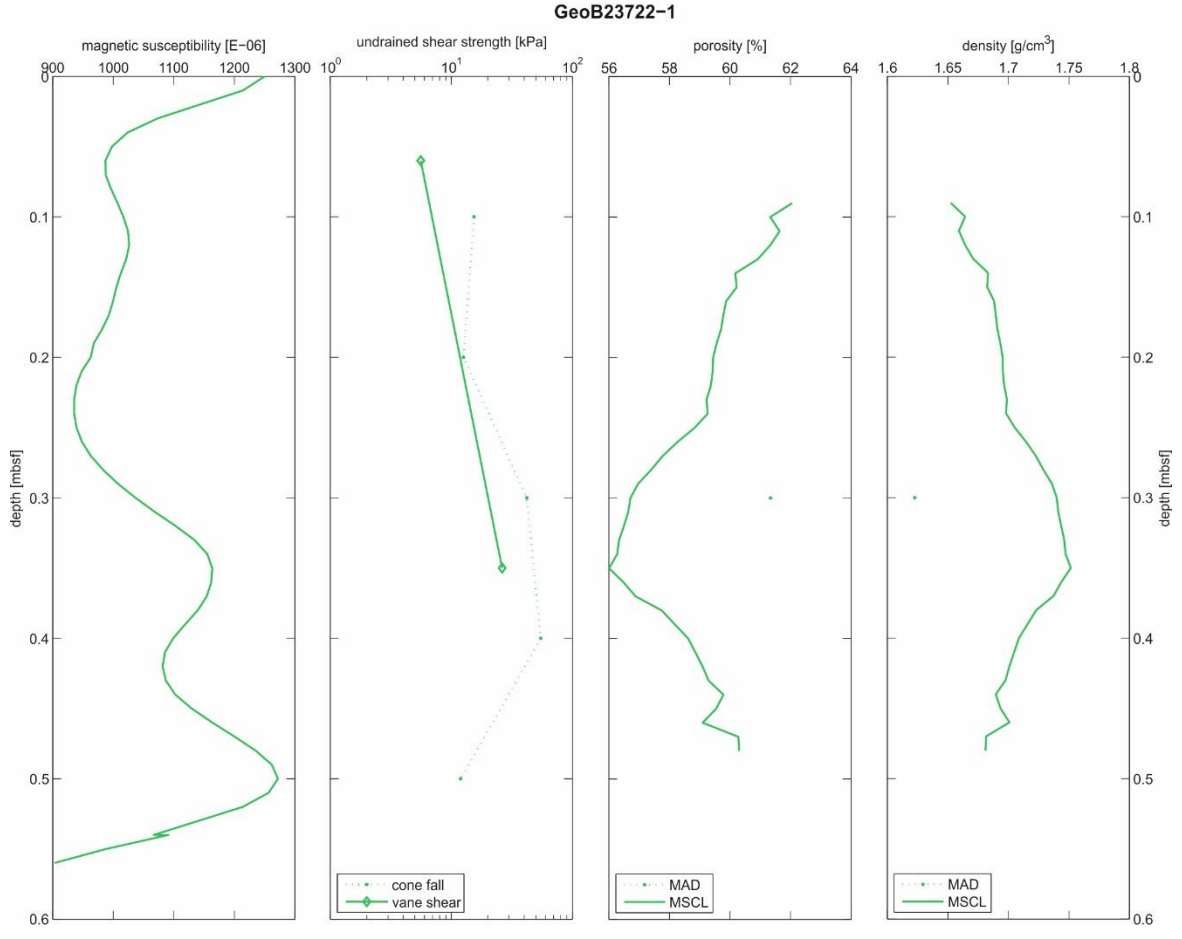
GeoB23722−1
magnetic susceptibility [E−06]
undrained shear strength [kPa]
porosity [%]
density [g/cm3]
depth [mbsf]
cone fall
vane shear
MAD
MSCL

GeoB23723−1

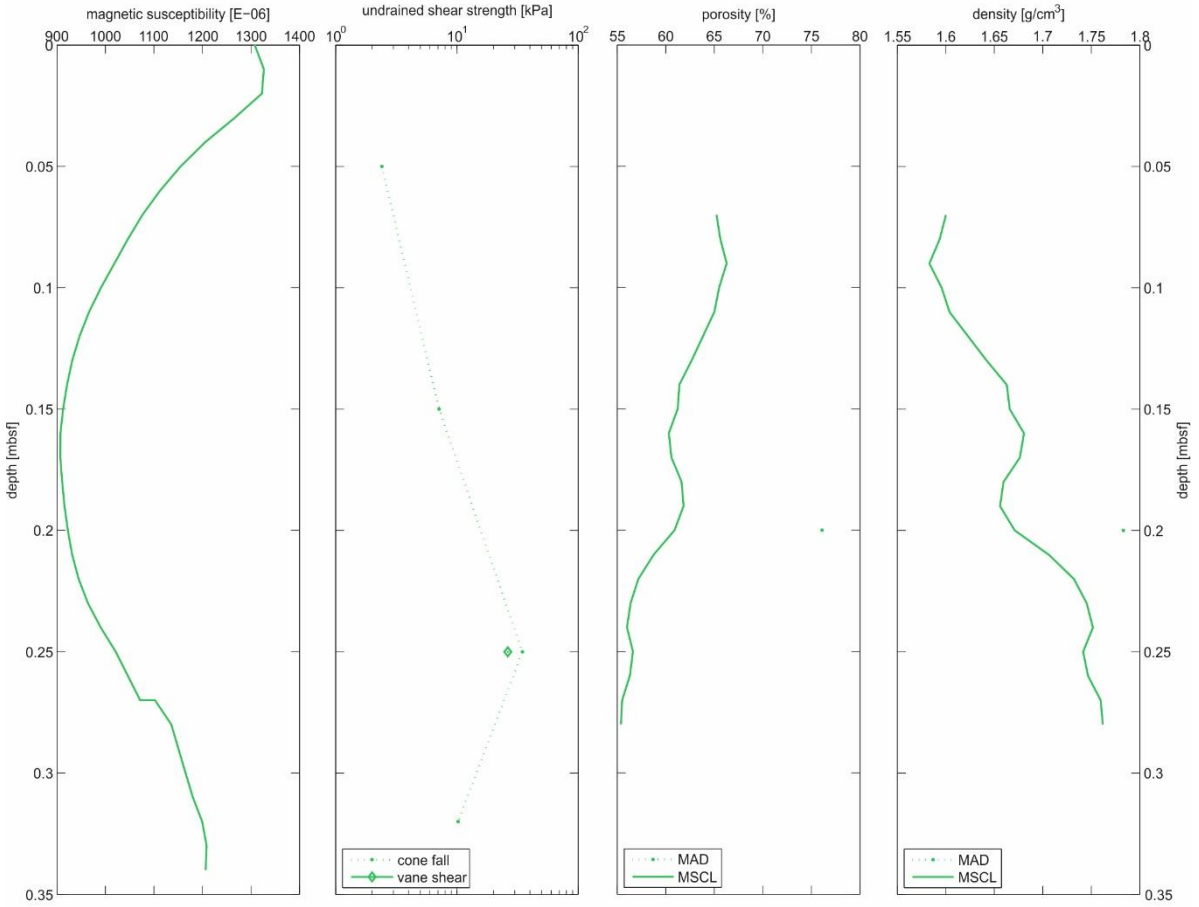

GeoB23724−1

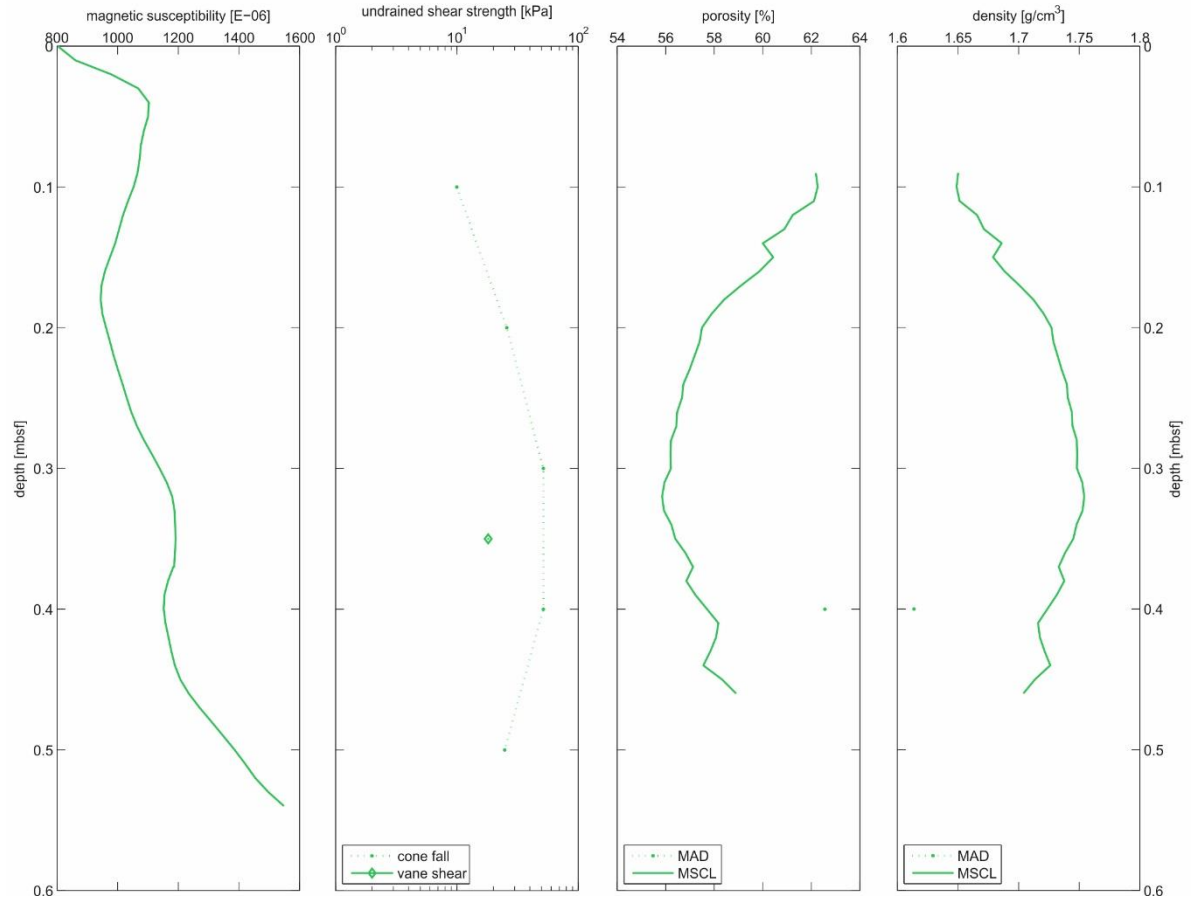

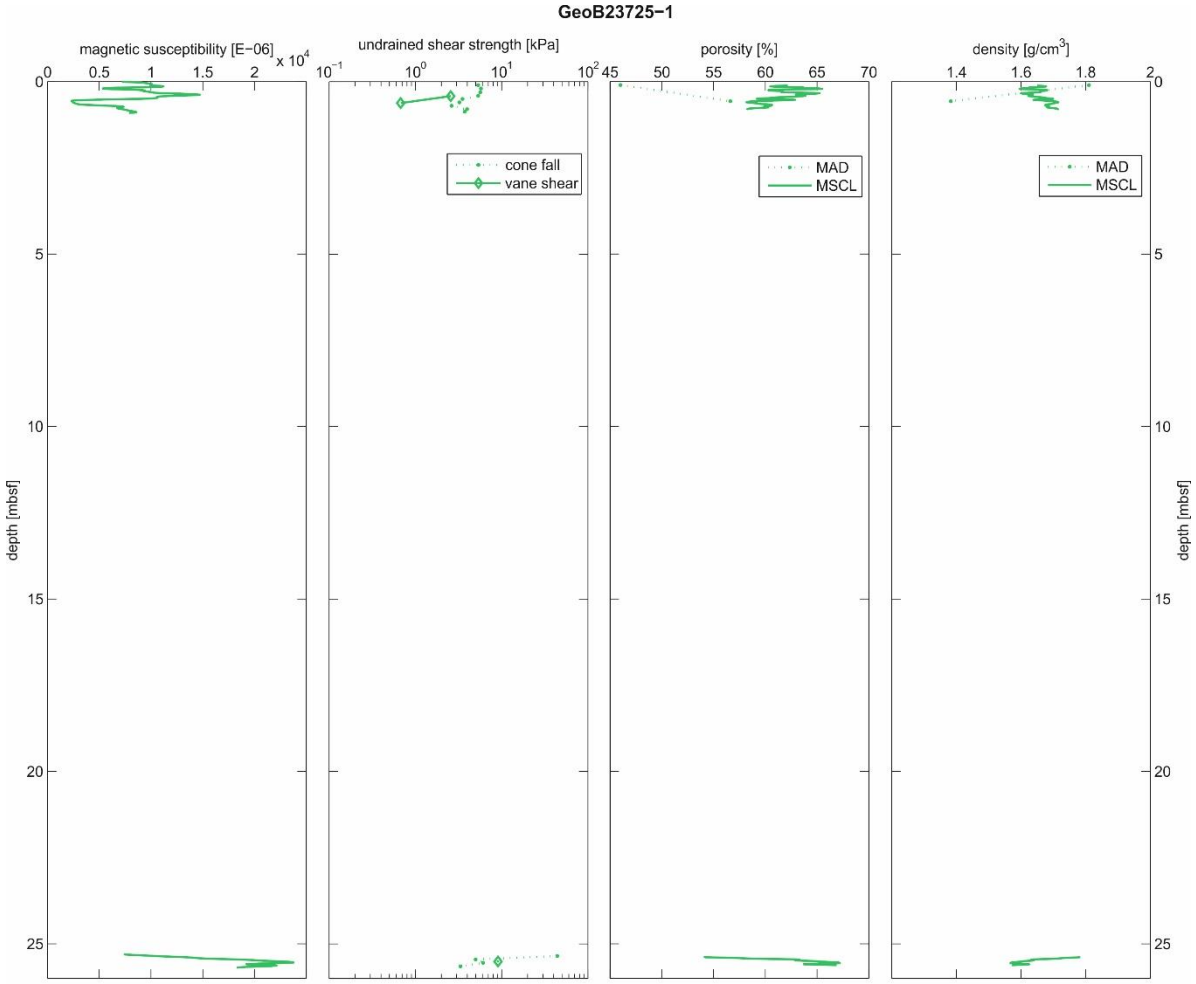
GeoB23725−1
magnetic susceptibility [E−06]
x 10^4
undrained shear strength [kPa]
porosity [%]
density [g/cm^3]
cone fall
vane shear
MAD
MSCL
MAD
MSCL
depth [mbsf]
depth [mbsf]